

© Copyright 2017

Jillian M. Schleicher

# Crystal-scale control on magmatic mush mobilization and mixing

Jillian M. Schleicher

A dissertation

submitted in partial fulfillment of the  
requirements for the degree of

Doctor of Philosophy

University of Washington

2017

Reading Committee:

George Bergantz, Chair

Robert Breidenthal

Bruce Nelson

Program Authorized to Offer Degree:

Earth and Space Sciences

University of Washington

**Abstract**

Crystal-scale control on magmatic mush mobilization and mixing

Jillian M. Schleicher

Chair of the Supervisory Committee:  
Dr. George Bergantz  
Department of Earth and Space Sciences

Magmatic systems present an apparent paradox: they exist as long-term, crystal-rich magmas (called mushes) which are mechanically locked, yet crystals in exposed plutons and volcanic deposits with diverse histories indicate magmatic mobilization and mixing processes are common. Geochemical and petrologic analyses of igneous rocks and crystals provide a way to distinguish magmatic events such as intrusion, crystallization, assimilation, and mixing that occurred. These events cannot be directly observed, so previous studies have used experiments and numerical simulations to investigate the dynamics of mobilization and mixing. The high-crystal fractions in mushes require consideration of particle-particle-liquid interactions, which previous continuum and quasi-multiphase models do not recover.

This dissertation takes a multi-scale approach to understanding the processes of mush mobilization and mixing. Chapters 2 and 3 present a discrete element method-computational fluid dynamics (DEM-CFD) model of a basalt and olivine magmatic mush subject to intrusion by basaltic magma from below. Chapter 2 demonstrates the crystal-scale control on the system-wide response to the intrusion. The localized mobilization of crystals above the intrusion site produces a region called the mixing bowl, where liquids and crystals are fluidized and mixed. Monitoring the crystals and liquid throughout the intrusion demonstrates the potential for diverse crystal populations to be created in even simple magmatic systems. Chapter 3 quantifies the dispersion of crystals in the simulations from their initial state for a range of intrusion velocities. The crystal dispersion occurs with an exponential relationship with time, and a mixing time scaling produces a single curve for the tested intrusion rates. Extrapolating the results to a realistic magmatic system produces mixing times that agree with those inferred for mixing events occurring in nature. Chapter 4 is a case study of a natural mush, the 1868 picrite eruption of Mauna Loa, Hawaii. Geochemical analyses at the crystal-scale demonstrate the existence of six olivine populations. These populations reflect a diversity of magmatic conditions and processes within the central and rift magmatic systems in Mauna Loa.

Also included with this dissertation are three supplementary movies. These movies show the simulation presented in Chapters 2 and 3. Movie 2.1 shows the intrusion of the magma into the mush, Movie 2.2 shows the coordination number of the crystals within the mush, and Movie 2.3 tracks the three pairs of crystals described in the text.



# TABLE OF CONTENTS

List of Figures .....	iv
List of Tables .....	v
Chapter 1. Introduction .....	9
1.1 Organization of Dissertation .....	9
1.2 Motivation .....	9
Chapter 2. The mechanics and temporal evolution of an open-system magmatic intrusion into a crystal-rich magma.....	13
2.1 Introduction.....	13
2.2 Multiphase simulation of an intruded magmatic mush.....	15
2.3 Mechanical fluidization of magmatic mushes .....	16
2.3.1 Scaling model variables for applications to natural examples .....	17
2.4 The cycle of an open-system intrusion event.....	19
2.4.1 Initially fluidizing the mush by intrusion of new magma .....	21
2.4.2 The self-similar mixing bowl.....	23
2.4.3 Termination of intrusion and defluidization of the mush .....	24
2.5 Granular mechanics and the Viscous and Coordination Numbers .....	24
2.6 The crystal record of the open-system event .....	31
2.7 Geological implications of the open-system model.....	39
2.8 Conclusions.....	40
2.9 Supplementary text .....	41

2.9.1	Supplementary movies.....	41
2.9.2	Simulation methods .....	42
Chapter 3. Time scales of crystal mixing in magma mushes.....		51
3.1	Introduction.....	51
3.2	A mixing paradigm for crystal-rich magma mushes .....	52
3.3	Calculating open-system mixing in crystal mush .....	56
3.3.1	Quantifying the mixing of discrete phases.....	56
3.3.2	The initial neighbor distance mixing index .....	57
3.4	Characteristic crystal mixing time calculation.....	58
3.4.1	Dimensionless time scale and mixing time calculation .....	58
3.4.2	Applications to natural systems .....	65
3.5	Summary and conclusions .....	66
Chapter 4. Mush mobilization and mixing in the 1868 eruption of Mauna Loa, Hawaii.....		67
4.1	Introduction.....	67
4.1.1	Crystal populations .....	67
4.1.2	Mauna Loa, Hawaii, 1868.....	70
4.2	Samples and methods.....	72
4.2.1	Sample locations .....	72
4.2.2	Modal abundances .....	72
4.2.3	X-ray Fluorescence .....	74
4.2.4	Electron Microprobe .....	74
4.3	Results.....	75

4.3.1	Whole rock.....	75
4.3.2	Microprobe.....	76
4.4	Discussion.....	82
4.4.1	Crystallization conditions of olivine.....	82
4.4.2	The reservoir system of Mauna Loa.....	87
4.4.3	Future work: diffusion modeling.....	90
	Bibliography.....	91

## LIST OF FIGURES

Figure 2.1. Simulation domain.....	19
Figure 2.2. Four time steps from the simulation of the open-system intrusion .....	20
Figure 2.3. The Viscous number of the intrusion at $t^*=1.48$ .....	28
Figure 2.4. Average coordination number for crystals .....	29
Figure 2.5. Trajectories and liquid composition for 3 pairs of crystals .....	32
Figure 2.6. Dissolution of orange crystals .....	37
Figure 3.1. Two time steps from the simulation of the open-system intrusion .....	54
Figure 3.2. Mobilized areas of crystals at different intrusion rates. ....	57
Figure 3.3. The IND as a function of dimensionless time for four intrusion rates .....	61
Figure 3.4. KDE for two time steps and initial neighbor distances .....	64
Figure 4.1. Olivine NiO-Fo relationships for published data .....	70
Figure 4.2. Map of the 1868 southwest rift eruption of Mauna Loa, Hawaii .....	73
Figure 4.3. Whole rock Mg# against olivine % in samples .....	75
Figure 4.4. PDFs of Fo# in olivine cores .....	77
Figure 4.5. Olivine core Fo# compositions and corresponding whole rock Mg#.....	78
Figure 4.6. Olivine NiO-Fo relationships for 1868 and published data.....	78
Figure 4.7. Examples of the 6 zoning varieties.....	80
Figure 4.8. NiO-Fo in cores of all crystal traverses with MELTS results .....	82
Figure 4.9. Evolution of NiO and Fo in crystal traverses with MELTS results .....	86

## LIST OF TABLES

Table 2.1. Simulation Parameters .....	16
Table 4.1. Description of six zoning population types .....	81
Table 4.2. Starting compositions for MELTS simulations .....	84

## ACKNOWLEDGEMENTS

I would like to express my appreciation for all those who have supported me through my time at the University of Washington, and in the years leading up to this point.

I want to thank my advisor, George Bergantz, for encouraging me to explore magmatic systems with an interdisciplinary perspective. Your enthusiasm for this work kept me excited and motivated throughout my time as a graduate student. I also appreciate your encouragement to participate in a variety of outreach activities and workshops, which expanded my graduate experience beyond a purely academic one.

Thank you to my committee, Bruce Nelson, Bob Breidenthal, Fangzhen Teng, and Alberto Aliseda. Your unique perspectives on this work always led to enlightening discussions, and I enjoyed working with all of you on this dissertation. Thanks also to Alain Burgisser for all your help with MFiX and quantifying mixing, and Scott Kuehner for teaching me and giving me assistance on our microprobe whenever I needed it. Finally, I want to thank my collaborators in Hawaii: Mike Garcia, Pete Lipman, and Frank Trusdell for working with me to sample the 1868 eruption of Mauna Loa, and also Tom Shea, Eric Hellebrand, and Kendra Lynn for insightful discussions about my sample results.

I would not have gotten this far academically without the amazing support and encouragement of my undergraduate professors at the University of St. Thomas. The professors in the physics and geology departments were such an inspiration to me; they constantly demonstrated their love of not only their research, but also of teaching and mentoring students. I might never have taken a geology class if Marty Johnston hadn't suggested it during my first semester as an undergraduate student. Taking classes and working on research projects with Tom

Hickson and Lisa Lamb taught me the benefits of interdisciplinary work and the joy of studying earth science.

I would like to thank the Department of Earth and Space Sciences for providing funding for my graduate work and supporting me during my time at the University of Washington. I would specifically like to thank No  ll Bernard-Kingsley, Lauren McOwen Wood, Ed Mulligan, Nathan Briley, Dave McDougall, Eunice Yang, Kathy Gabriel, and Sue Bernhardt for all their assistance.

I want to thank my friends in Seattle and elsewhere for giving me encouragement and happiness throughout my PhD. I especially thank the incredible women of the Seattle Ladies Choir who cheered me on throughout my graduate career. Finally, I have to thank the ESS graduate students who gave me encouragement, advice, and kept me laughing for the last six years.

Most importantly, thank you to my family. Thank you to my brother, Andrew, for being my being my closest friend growing up, and for sending me things to keep me smiling during my PhD. Thank you to my parents, Judy, Dave, Erik, and Liz. You supported me my whole life, let me take my own path, and always gave me encouragement and advice. I especially want to thank my mom, Judy, for our weekly Skype calls and always being there for me when I needed it most.

## **DEDICATION**

To my parents: Judy, Dave, Erik, and Liz,  
and to my brother, Andrew



# Chapter 1. INTRODUCTION

## 1.1 ORGANIZATION OF DISSERTATION

This first chapter provides the motivation for the work done for this dissertation. Chapters 2-4 have been written as stand-alone papers. Chapter 2 of this dissertation, "The mechanics and temporal evolution of an open-system magmatic intrusion into a crystal-rich magma" is in press at the *Journal of Petrology* as of August 2017. Chapter 3, "Time scales of crystal mixing in magma mushes" was published in the journal *Geophysical Research Letters* in February 2016. Chapter 4, "Mush mobilization and mixing in the 1868 eruption of Mauna Loa, Hawaii," will be submitted during Fall Quarter 2017. References for all chapters are at the end of this dissertation.

## 1.2 MOTIVATION

An unresolved issue in understanding igneous systems is the apparent paradox of the long-term existence of crystal-rich (and therefore mechanically locked) magmas known as mushes, while the exposed plutons and volcanic deposits derived from these mushes indicate magma mobilization and mixing are common processes. Direct observation of these processes is not possible, so geochemical and petrologic analyses of igneous rocks provide a way to infer magmatic responses to events such as intrusion, crystallization, assimilation, and mixing. Plutonic rocks integrate tens of thousands to millions of years of the reservoir's existence (Barboni & Schoene, 2014; Cooper, 2015; Cooper & Kent, 2014), though this makes it difficult to distinguish individual mobilization and mixing events. Volcanic deposits sample the state of a magma reservoir in the hours, days, and months before they erupt (Cooper, 2015; Costa *et al.*, 2010; Kahl *et al.*, 2011, 2013; Moore *et al.*, 2014). This makes them ideal for understanding the

processes leading to their eruption, but they only include the mobilized portion of the reservoir at that point in time.

Crystals with diverse histories found in volcanic samples can provide a longer, more complete story of the physical and compositional conditions in the reservoir. Microanalytic analyses of major, trace, and isotopic zoning patterns; melt inclusions; crystal sizes and morphologies; and age dating of crystals can be used to identify mobilization and mixing events which brought the erupted crystal assemblage together. The use of these techniques can identify crystal populations that reflect the long-term conditions in magmatic reservoirs (Cooper, 2015; Cooper & Kent, 2014) and changes in these conditions by short-term events (Costa *et al.*, 2010; Kahl *et al.*, 2011; Thomson & Maclennan, 2013). This dissertation uses multiphase numerical simulations and geochemical analysis of crystals in a simple magmatic system to identify crystal-scale control of, and response to, magmatic mobilization and mixing processes.

Due to the inability to observe magmatic processes as they occur, previous studies have used experiments and numerical simulations to investigate the mechanics of magmatic mobilization and mixing. Previous laboratory experiments have used fluids of different densities (e.g. (Huppert *et al.*, 1986; Turner & Campbell, 1986)) and particle-rich systems (e.g. (Girard & Stix, 2009; Hodge *et al.*, 2012)) to investigate the dynamics of mobilization and mixing in magmas. However, the high crystal fractions in magmatic mushes make it difficult to create laboratory systems where variables including temperature, volume fraction, and velocities are monitored throughout the experiment. Numerical modeling using continuum or quasi-multiphase methods has the ability to monitor these variables throughout the simulation (Dufek & Bergantz, 2007; McKenzie, 1984; Ruprecht *et al.*, 2008). However, physics and engineering advances in particle mechanics demonstrate the importance of considering interactions (frictional and collisional

contacts, buoyancy, viscous coupling, and lubrication) between individual particles and the liquid in systems with high particle volume fractions (Andreotti *et al.*, 2013; Campbell, 2006; Forterre & Pouliquen, 2008; MiDi, 2004).

The first question addressed in this dissertation is: how does a magmatic mush become mobilized? Chapter 2 introduces a numerical model of a basalt and olivine magmatic mush subject to intrusion by basaltic magma from below. Persistent crystal-rich conditions in basaltic magma bodies have been inferred from seismic evidence from ocean islands and mid-ocean ridges (Clague & Denlinger, 1994; Sinton & Detrick, 1992), and from the eruption of picrites (Rhodes, 1995). We present a simulation that is a discrete element method-computational fluid dynamics model, where every crystal is monitored for the duration of the intrusion, mobilization, and subsequent settling. As the liquid intrudes the mush, it mobilizes only a portion of the crystals; we call this region the mixing bowl. The presence of the crystal mush affects the dynamics of the entire domain as the liquids and crystals mix. As crystals encounter the intruding liquid, we use a reaction model to calculate the dissolution of a pair of crystals as they move through the mush. With this model, we demonstrate the potential for diverse populations of crystals to emerge in even the simplest magmatic systems (e.g. (Helz, 1987)).

Studies of crystal zoning and chemical diffusion can constrain the time elapsed between intrusion, mixing, and eruption, which may range from hours to months. Once a mush is mobilized, the question becomes: how long does it take for it to become mixed? In Chapter 3, we quantify the dispersion of crystals during magmatic intrusion for simulations similar to the one presented in Chapter 2. We test a range of intrusion velocities that determine the initial volume of crystals and liquid that is mobilized. From there, we use a mixing metric, the initial neighbor distance, which determines the dispersion of initially neighboring crystals for each intrusion rate.

We find an exponential relationship between the mixing and the duration of the intrusion, when time is scaled with a characteristic mixing time. Extrapolating this relationship to realistic mush parameters gives us mixing times that agree with those inferred to occur in similar magmatic systems in nature.

The fourth chapter of this dissertation is a case study of an erupted basalt and olivine mush. The 1868 eruption from the Southwest Rift Zone of Mauna Loa is one of two subaerial picrite eruptions that have occurred on Mauna Loa in recorded history. Despite the simple magmatic conditions, we identified six populations of olivine crystals that exist in both the olivine-rich picrites and olivine-poor basalts, defined by the crystal zoning of Fo# and NiO in olivine. We use MELTS experiments to infer the magmatic conditions under which the crystals grew, were stored, mobilized, and mixed. Using these experiments and the crystal zoning populations, we present a preliminary description of the central and rift magmatic systems within Mauna Loa, and a qualitative estimate for the relative timing of mixing events. Future diffusion modeling of the crystal compositions will provide estimates of the timescales of mush mobilization and mixing prior to the eruption.

## Chapter 2. THE MECHANICS AND TEMPORAL EVOLUTION OF AN OPEN-SYSTEM MAGMATIC INTRUSION INTO A CRYSTAL-RICH MAGMA

*This manuscript is in press as of August 2017 at the Journal of Petrology.*  
Co-authored by Jillian M. Schleicher, George W. Bergantz

### 2.1 INTRODUCTION

Magma reservoirs are dominated by near-solidus, high crystal-fraction conditions (known as a magmatic mush) for tens of thousands to millions of years (Cooper, 2015; Reid, 2008; Schmitt, 2011). Yet complexly zoned crystals erupted from crystal-rich magmas require rapid mobilization occurring on timescales over days to hundreds of years (Cooper, 2015; Cooper *et al.*, 2016; Costa & Morgan, 2011; Kahl *et al.*, 2011, 2013; Moore *et al.*, 2014; Shea *et al.*, 2015b). Open-system intrusions of magma into magmatic mushes can rapidly disaggregate and mobilize the near-solidus magma, and explain the eruption of distinct populations of crystals (Bergantz *et al.*, 2015; Burgisser & Bergantz, 2011; Girard & Stix, 2009; Huber *et al.*, 2012; Kahl *et al.*, 2011; Ruprecht *et al.*, 2008; Streck, 2008; Thomson & MacLennan, 2013; Wallace & Bergantz, 2005) and crystals out of equilibrium with their carrier liquids (Moore *et al.*, 2014; Neave *et al.*, 2013; Passmore *et al.*, 2012). However, the mechanics and temporal evolution of an open-system intrusion are not well understood (Bergantz & Breidenthal, 2001). Geological examples demonstrate that intruded magma can percolate or pond in the resident mush (Costa *et al.*, 2010; Paterson, 2009; Perugini & Poli, 2005), or can lead to mush disaggregation and eruption (Kahl *et al.*, 2011; Passmore *et al.*, 2012; Thomson & MacLennan, 2013).

The presence of crystals greatly affects the mechanics of a magma through both hydrodynamic and granular interactions (Marsh, 1981). Crystal concentrations of as little as 25 volume% can

form crystal contact networks (Philpotts *et al.*, 1999) which can cause jamming, strain localization, variable crystal packing, and the transmission of stress by crystal-crystal contacts called force chains (Estep & Dufek, 2012; Sandnes *et al.*, 2011; Sun *et al.*, 2010). There are several mechanisms that can lead to the fluidization of crystals within a mush, including gas-driven overturn (Ruprecht *et al.*, 2008), buoyancy-driven overturn from basal intrusion and heating (Burgisser & Bergantz, 2011; Girard & Stix, 2009; Huber *et al.*, 2012), and momentum-driven fluidization by magmatic intrusions (Bergantz *et al.*, 2015). An open-system, momentum-driven intrusion can fluidize a crystal-rich mush when the intruding liquid locally separates contacts between crystals. This creates locally dilute (higher porosity) regions of the mush, which behave as a mobile fluid rather than a viscoplastic solid.

Investigating the mechanics involved in an open-system intrusion requires an approach that resolves both the crystal-scale and the mush-scale throughout the event. We present a discrete element method-computational fluid dynamics (DEM-CFD) simulation to examine the granular and fluid dynamics of basaltic liquid intruding into an olivine-rich basaltic mush. The particle-based numerical modeling is described in the Supplemental Text (Section 2.9) and includes frictional, collisional, translational, and buoyant forces, as well as viscous particle-particle-fluid coupling. This approach reveals the microphysical controls on fluidization and mixing in a mush over a range of spatial scales simultaneously that cannot be resolved with continuum modeling (mixture or Eulerian-Eulerian multi-fluid theories). The particle-based simulation records the motion of all crystals within the mush, enabling us to examine crystal gathering and dispersal during the intrusion.

We have described some general features of magma dynamics using the DEM-CFD method in two previous publications. In Bergantz *et al.*, (2015) we introduced the notion of the ‘mixing

bowl' but did not describe the distinct time-dependent regimes throughout an open-system cycle. In Schleicher *et al.*, (2016) we described the ways that crystal mixing could be quantified. Here we document and describe the distinct kinematic stages of an open-system event in a magma mush, and present a scaling to describe the multiphase dynamics under crystal-rich conditions. We also monitor the mixing between the crystals and the resident and intruding liquids, and their potential for recording the intrusion with crystal growth or dissolution.

## 2.2 MULTIPHASE SIMULATION OF AN INTRUDED MAGMATIC MUSH

To exemplify the mechanics of an open-system intrusion, we consider a geologically simple, yet common crystal-rich system: an olivine-mush in basaltic liquid (Table 2.1). To create the mush, we randomly distribute olivine crystals throughout the domain and allow them to settle. Crystals naturally organize into a random loose-packed bed, creating an average crystal fraction of  $\sim 0.6$ . We saturate the crystals with a resident liquid, which extends above the bed into a crystal-free region. An intruding crystal-free liquid enters the mush as a dike into the base of the domain at a constant momentum flux. The properties of the resident and intruding liquids are the same, approximating conditions observed in basalts (Table 2.1); calculations with MELTS indicated that melt density changed only 0.6% over the 50°C temperature interval assumed here and so will have negligible influence on the dynamics. Basaltic systems are often intruded by liquids with similar temperatures, viscosities, and densities to those residing within the mush (Geist *et al.*, 2006; Rhodes, 1988), therefore all simulations are run with isothermal conditions. The open-system nature of the intrusion requires a domain where liquid is allowed to leave the top to accommodate the constant momentum flux of the intruding liquid. This assumption is supported by geological examples where input can be accommodated by crustal deformation (Baker & Amelung, 2012; Gerbi *et al.*, 2004). Additionally, magma can drain from cracks in the

crust above magma reservoirs, allowing intruding magma to fill in the void spaces without accompanying crustal deformation (Johnson *et al.*, 2010). The walls and base of the domain have a no-slip boundary condition for the liquid, and a wall-friction law for the crystals. The majority of liquid and crystal motions occur far from the walls, so boundaries have little influence on the overall dynamics of the system. Simulations are 2.5-D, with the depth of the domain given by the diameter of the crystals. However, this value is much less than the other spatial dimensions in the system, creating an effectively 2-D system. The theory and equations describing the numerical simulations can be found in the Supplemental Text (Section 2.9).

Table 2.1. Simulation Parameters

Parameter [units]	Variables	Values
Domain size [m]	$D_w, D_h$	2.56, 1.28
Computational grid size [m]		0.01, 0.01
Injection width [m]	$I_w$	0.32
Liquid density [ $\text{kg/m}^3$ ]	$\rho_l$	2650
Liquid dynamic viscosity [ $\text{Pa}\cdot\text{s}$ ]	$\mu_l$	0.2
Crystal density [ $\text{kg/m}^3$ ]	$\rho_c$	3300
Crystal diameter [m]	$d_c$	0.004
Initial bed height [m]	$H_0$	0.823
Number of crystals	$N$	147,040
Simulation time [s]	$t$	100
Injection velocity [m/s]	$U_0$	0.023
Minimum fluidization velocity [m/s]	$U_{mf}$	0.0025
Mixing bowl taper angle from the vertical [radians]	$\alpha$	$\pi/6$

### 2.3 MECHANICAL FLUIDIZATION OF MAGMATIC MUSHES

The general concept of fluidization as used in industry and sedimentary geology refers to the support of a bed of particles by the upward drag exerted by a fluid. The fluid works against gravity, expanding and supporting the bed from a stationary rest state. To fluidize a crystal-rich mush, the intruding liquid must enter at a sufficient rate to overcome the weight of the crystal bed. This rate is known as the minimum fluidization velocity ( $U_{mf}$ ), which is commonly



calculated using the Ergun equation (Ergun, 1952). This equation for the minimum fluidization velocity estimates the velocity of the injected liquid needed to induce a drag force on the crystals equaling the weight of the crystals. In these calculations, the work needed to overcome initial contact friction between the crystals is ignored.

### 2.3.1 *Scaling model variables for applications to natural examples*

The application of a model to natural examples requires scaling variables to ensure consistent extension of model results to other similar applications. Hence, the thermophysical properties and the system geometry need to be represented in terms of scaled quantities. In the case of our model of a crystal mush, these are the size of the crystals, the liquid viscosity, the thickness of the bed, and the rate of the incoming new intrusion that acts as to fluidize the crystal bed. One quantity that embodies all these degrees of freedom is the minimum fluidization velocity. In our simulations, liquid intrudes only a portion of the base of the crystal bed. We also know from our results described below that the fluidization occurs as a tapered geometry, an emergent property of the calculations, and we apply that ex post facto to ensure the proper scaling. Because of this, the Ergun equation must be modified to account for only the crystals that are fluidized in the region above the intrusion. As in Bergantz *et al.* (2015) and Schleicher *et al.* (2016), we use a modified  $U_{mf}$  calculation in our simulations, which accounts for the small injection region relative to the domain size (Cui *et al.*, 2014):

$$\frac{1}{2}\alpha BI_w^2 \ln\left(\frac{2H_0}{I_w}\right)U_{mf}^2 + \alpha AI_w\left(H_0 - \frac{I_w}{2}\right)U_{mf} = (I_w + H_0 \tan\alpha)H_0(\rho_c - \rho_l)g(1 - \varepsilon_l) \quad (2.1)$$

$$A = 150 \frac{(1 - \varepsilon_l)^2}{\varepsilon_l^3} \frac{\mu_l}{d_c^2} \quad (2.2)$$

$$B = 1.75 \frac{(1 - \varepsilon_l) \rho_l}{\varepsilon_l^3 d_c} \quad (2.3)$$

In these equations,  $\alpha$  is the angle from the vertical formed by the tapered geometry of the mixing bowl (Figure 2.1),  $I_w$  is the width of the injection region,  $H_0$  is the height of the crystal-liquid bed,  $U_{mf}$  is the minimum fluidization velocity,  $\varepsilon_l$  is the liquid fraction (porosity),  $\mu_l$  is the dynamic viscosity of the liquid,  $\rho_l$  is the liquid density,  $d_c$  is the crystal diameter,  $\rho_c$  is the crystal density, and  $g$  is the magnitude of gravitational acceleration.

Only one intrusion rate is exemplified in our detailed example presented here, however varied intrusion rates of the intruded liquid change the emergent behavior of the mush (Schleicher *et al.*, 2016). We introduce a non-dimensional velocity  $U^*$  which is the injected velocity of the liquid ( $U_0$ ) divided by the  $U_{mf}$  of the mush ( $U^* = U_0 / U_{mf}$ ). At low intrusion rates ( $U^* \ll 1$ ), the liquid is unable to fluidize the crystals and passes through the mush by porous flow. Intermediate intrusion rates ( $U^* \sim 1$ ) create a short, crystal-poor cavity, and higher intrusion rates ( $U^* > 1$ ) extend the cavity into a chimney (Philippe & Badiane, 2013). In magmatic systems, open-system intrusions may occur with liquid rising slowly through the mush, passing through the crystals as porous flow ( $U^* < 1$ ). Examples of this exist in Iceland and in other rift zone systems (Costa *et al.*, 2010; Thomson & MacLennan, 2013). Other intrusions can enter the mush with sufficient momentum to fluidize the crystals ( $U^* > 1$ ), leading to mixing and possibly eruption (Moore *et al.*, 2014; Neave *et al.*, 2013; Passmore *et al.*, 2012).

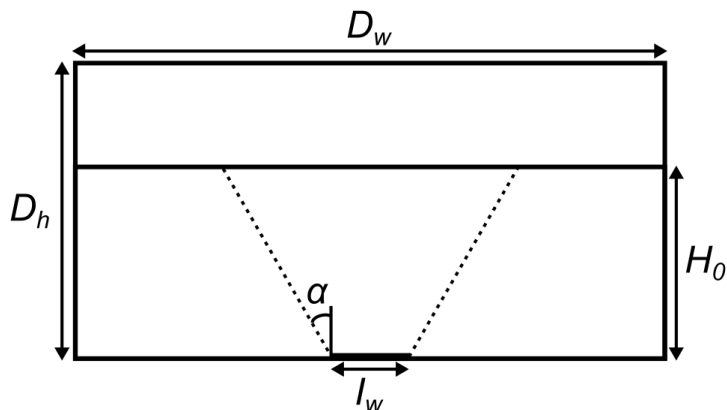


Figure 2.1. Schematic of the simulation domain ( $D_w$  is width,  $D_H$  is height) and emergent mixing bowl, illustrating variables used in Equations 2.1, 2.2, 2.3

## 2.4 THE CYCLE OF AN OPEN-SYSTEM INTRUSION EVENT

Below we describe the three stages that a model crystal-rich mush might experience during an open-system event where a portion of the resident mush is fully fluidized. These stages correspond to 1) the initial response of the mush to the intrusion, 2) the self-similar, quasi steady state stage, and 3) the shut-off stage at the end of the open-system event. Distinct multiphase regimes can exist simultaneously during these stages of the intrusion as a result of the changing particle volume fraction (Andreotti *et al.*, 2013; Jaeger *et al.*, 1996). The highest particle fraction regime ( $\geq 0.5$ ) is called the quasi-static state, where particles are in constant frictional and normal contact. Relative particle motion occurs by particle translation governed by the inter-particle geometry (Roux, 2009). At intermediate volume fractions ( $\sim 0.5-0.1$ ) is the dense granular regime (Jop, 2015; MiDi, 2004) where particles are fluidized, but frequent contacts between particles may be sustained (frictional) or collisional. At very low particle fractions ( $< 0.1$ ) the granular flow is in the dilute regime, where particle contacts are infrequent, and momentum is exchanged by collisions (Goldhirsch, 2003). These three granular regimes express the diversity of mechanical behavior exhibited by the mush throughout an open-system cycle. The simulation can be viewed in the supplemental material (Movie 2.1).

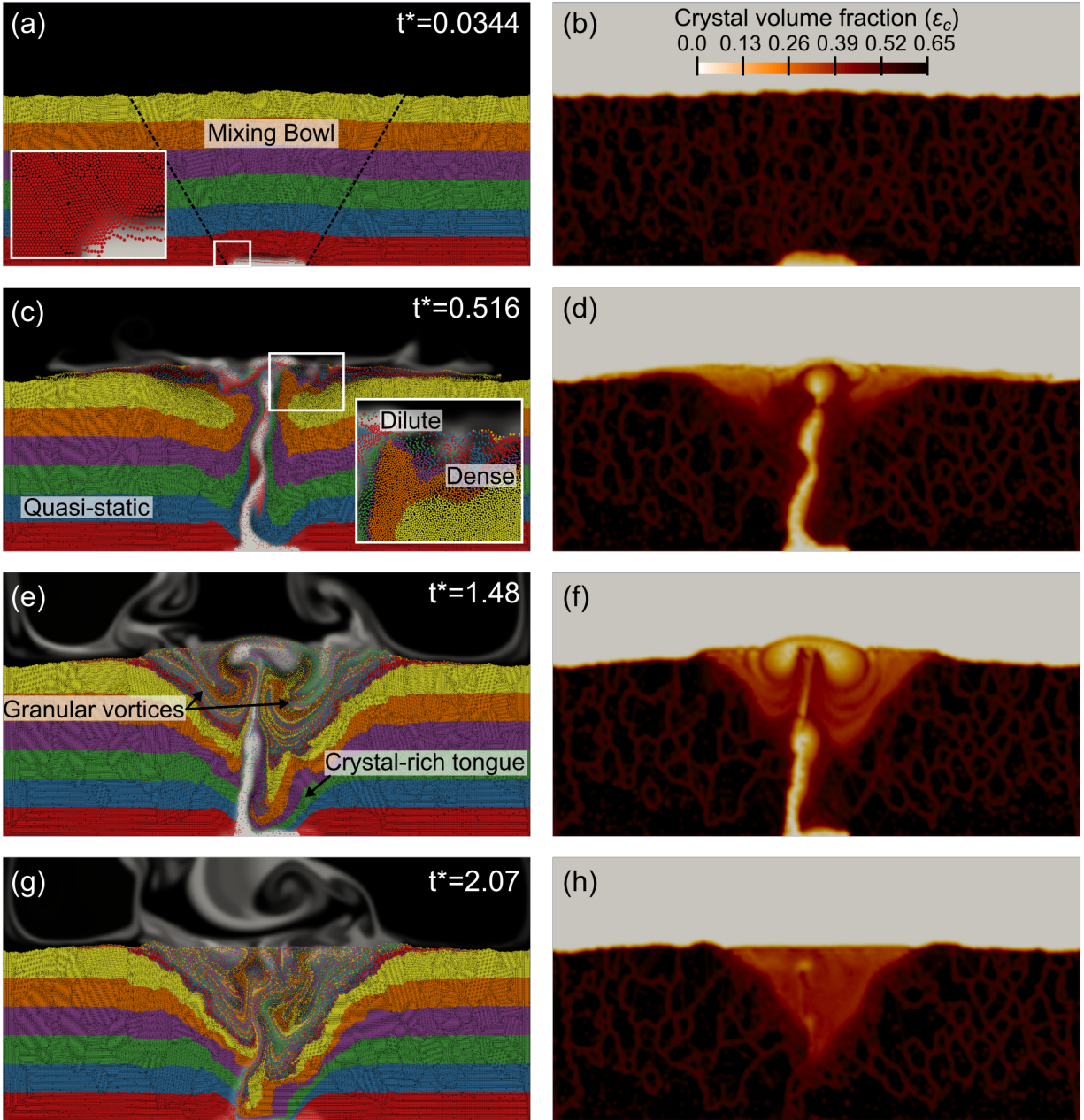


Figure 2.2. Four time steps from the simulation of the open-system intrusion, where  $t^*=(U_0/H_0)t$ . Subfigures (a), (c), (e), and (g) show the crystals (colored bands) and liquids (black for resident liquid, white for intruding liquid), while subfigures (b), (d), (f), and (h) show the crystal volume fraction for the same times. Black dashed lines in (a) represent the extent of the mixing bowl and inset image shows the lines of crystals forming the granular faults. Color bar in (b) illustrates the crystal volume fraction. The variations in crystal volume fraction within the bed represent the variable packing of the crystals from the initial random settling. See text for additional description and details.

#### 2.4.1 *Initially fluidizing the mush by intrusion of new magma*

When the new magma intrudes the resident crystal-rich mush, the mush responds as a viscoplastic material. The initial crystal packing in the bed ( $\epsilon_c \sim 0.6$ ) results in continuous contact between crystals (i.e. the quasi-static granular regime). Slight variation in crystal volume fraction exists in the bed (Figure 2.2b), which is the result of natural settling of the crystals to form the mush. At the start of the intrusion, pore-pressure created from the intruding liquid exceeds the frictional yield strength of the mush; the viscoplastic response of the mush includes vertical expansion and simultaneous fluidization along bounding crystal-liquid faults (Figure 2.2a). We use the term “fault” because the initial failure is one involving frictional forces, there is manifest material displacement across the interface, the interfaces persist with minor erosion along the surfaces, and the faults are at approximately  $60^\circ$  angles to the horizontal on both sides of the intrusion, as predicted by Mohr-Coulomb failure criteria. They are faults, rather than shear zones. At the crystal scale, each fault is not a single plane (line, in the case of the 2D simulation), but a band of crystals moving along  $60^\circ$  angles from the horizontal (see inset image in Figure 2.2a). The crystal networks can be  $\sim 10$ -100 crystals long, and the lateral extent of the crystals creating the macroscopic faults can be  $\sim 10$ -20 crystals wide. The faults delimit the region of the mush that is unlocked by fluidization, and this region is referred to as the mixing bowl.

The geometry of the mixing bowl is established by this initial response and is insensitive to changes in intrusion rates exceeding the  $U_{mf}$ . In this simulation the intrusion rate is 9.26 times the  $U_{mf}$  ( $U^*=9.26$ ). The mixing bowl is a robust feature indicating that the numerical experiments satisfy the criteria for a self-similar extensible result. For example, varying the mush height does not alter the angle of the faults delimiting the mixing bowl, even when the height of the bed is

less than half the width of the intrusion. As shown later in the simulation, most of the mixing that occurs in the mush is within the mixing bowl, the only portion of the mush that is mobilized.

The initial viscoplastic response of the mush is followed by block uplift of the resident mush within the mixing bowl, similar to experiments by Johnsen *et al.*, (2008). After the initial uplift, the intruding liquid forms a small crystal-poor cavity that breaks up into finger-like instabilities as penetrative convection of the new liquid enters the mush. Around each instability is a halo of fluidized crystals that propagates ahead of the intruding liquid. The fingers do not rise at the same rate, and the shear stress at their margins entrains them together to form a single, rising, crystal-poor feature (these dynamic features are best seen in the supplemental Movie 2.1). The length scales of this process are not recoverable by Saffman-Taylor viscous scaling (where less viscous material intrudes more viscous material) due to intermittent flow from particle jamming (Sandnes *et al.*, 2011). The rising intruding liquid entrains crystals from the base of the mush and carries them upwards to the top of the crystal bed. This crystal-fluid coupling hinders the formation of lasting crystal contacts, placing the low-crystal fraction instability within the dilute granular regime (Andreotti *et al.*, 2013; Burgisser *et al.*, 2005).

Once the initial instability has penetrated the entire mush the initial transient ends, leaving a feature we call the chimney (Figure 2.2c and 2.2d). The chimney is a region of continued throughput and high porosity, surrounded by variably fluidized mush. Outside of the dilute chimney, the mixing bowl remains in the quasi-static regime where the crystal volume fraction is close-packed. The upper portion of the mixing bowl has a lower crystal volume fraction and is in the dense granular regime.

#### 2.4.2 *The self-similar mixing bowl*

After the initial transient described above, the dynamics in the mixing bowl are governed by quasi steady state, self-similar behavior (Figure 2.2e) (self-similar describes an object or condition whose proportions remain the same as it gets larger or smaller; the features are scale invariant). The approximate geometry of the mixing bowl persists, although there is minor crystal transport from erosion of the bounding granular faults. The dominant feature within the mixing bowl is the crystal-poor chimney. Throughout the intrusion, the chimney rises through the mush with varicose and meandering instabilities (Huppert *et al.*, 1986). These forms of instability reflect the moderate Reynolds numbers ( $\sim 10-100$ ) of the chimney as it moves through the mush (see Figure 7 in Huppert *et al.* (1986)). The varicose instabilities cause liquid to arrive at the top of the mush in pulses, creating local variations in crystal fraction within the dense granular regions at the top of the mixing bowl (Figure 2.2f).

As the crystal-poor liquid rises through the mush, it entrains crystals from the base of the mixing bowl and the sides of the chimney. These crystals are carried to the top of the mush and deposited on either side of the chimney, while the chimney liquid bifurcates and rises to mingle with the resident liquid above the mush. The entrainment, vertical transport, and deposition of crystals by the chimney create counter-rotating “granular vortices” that mix the crystals and liquid at the top of the mixing bowl. The overturn time of these granular vortices is approximately the same as the transit time of a crystal through the entire chimney. Due to the meandering chimney, the vortices are not perfectly symmetric within the mixing bowl. However the persistent fluidization of the mixing bowl maintains a self-similar geometry. In addition to upwards translation of crystals by the chimney, coherent tongues of crystals move downwards along the crystal-liquid faults of the mixing bowl. This continued upwards and downwards

motion of the crystals extends the well-mixed portion of the mixing bowl towards the intrusion site. We have previously shown (Schleicher *et al.*, 2016) that the majority of the crystals within the entire mixing bowl eventually become well mixed.

#### 2.4.3 *Termination of intrusion and defluidization of the mush*

Once the new magma input is terminated, the mixing bowl begins to defluidize and collapse (Figure 2.2g and 2.2h). The collapse happens rapidly at the bottom, where low porosity, crystal-rich tongues slump into the former location of the chimney, reestablishing a quasi-static regime. This rapid collapse hinders additional mixing of the liquids, so a fossil chimney of intruded liquid remains. In the higher porosity core of the mixing bowl, the reestablishment of the close-packed mush occurs as hindered crystal settling. The top of the mixing bowl has a concave-up shape with pronounced shoulders, which formed as some crystals were transported out of the mixing bowl during the intrusion. Once the crystals have returned to a settled state, the mixing bowl will have a fossil kinematic and compositional character, distinct from the surrounding mush which was undisturbed by the intrusion.

## 2.5 GRANULAR MECHANICS AND THE VISCOUS AND COORDINATION NUMBERS

The three stages of the open-system event described above demonstrate the complexity of dynamic states that can be manifested by multiphase systems with high particle concentrations. Multiple hydrogranular regimes are present at any given time during the simulation; these regimes are distinguished by the local particle fraction, the timescales involved with particle motion, and the shear rate. This is because the transmission of force by hydrogranular interactions has numerous sources: collisions, enduring frictional contact, lubrication, and fluid viscous effects. This is especially the case in particle-rich systems such as those considered here,



where the forces and particle support are transmitted along quasi-linear force chains that appear stochastically (Cates *et al.*, 1998; Estep & Dufek, 2012; Sun *et al.*, 2010). This produces a support fabric composed of load-bearing particles and spectators (Cates *et al.*, 1998; Estep & Dufek, 2012; Sun *et al.*, 2010). The force chains that form the support fabric migrate in response to external forcing, such that a particle that is a spectator one moment may be load-bearing the next. Even in simple, unimodal mixtures this can often produce non-affine deformation and non-local conditions such that the stress at a point depends on the degree of mobility in the surroundings as well as the shear rate (Trulsson *et al.*, 2012).

One system property that has been invoked for distinguishing mechanical states is the critical crystal fraction associated with jamming,  $(\varepsilon_{c,c})$  (Marsh, 1981). A thorough discussion of jamming, which progresses through a succession of micro-and-macrofragile states (Cates *et al.*, 1998; Ness & Sun, 2016) to hard jamming when a critical shear stress (not shear rate) is exceeded (Peters *et al.*, 2016) is beyond the scope of this work so we simply adopt the findings of Ness & Sun (2015) where a threshold particle fraction for monodisperse spherical particles occurs between 0.57 and 0.59. The highest particle fractions define the quasi-static regime, where particle contacts are enduring and frictional contact is the primary mechanism of force transmission. The dense granular regime is challenging to generalize with a bulk rheology, since the behavior depends not only on volume fraction, but also sample preparation (Daerr & Douady, 1999), confining pressure, and shear rate (da Cruz *et al.*, 2005). Once the system reaches  $\varepsilon_{c,c}$ , the granular media macroscopically behaves as a plastic material, controlled by a friction criterion with a linear relationship between shear and normal stresses.

Despite this complexity, remarkably, the same approach that has been useful in illuminating the fundamental controls on dilute multiphase flow (Burgisser *et al.*, 2005) can be employed in

high-particle fraction conditions. That is, the microscopic response timescale of a single particle relative to the macroscopic timescale of the far-field forces acting on that particle can rationalize the multiphase physics. For example in the context of dilute flow, this is the ratio of the microscopic aerodynamic response time of a particle to the time a macroscopic carrier phase (fluid in this case) exerts a distinct force on it. This led to the introduction of a Stokes number that is the ratio of those two timescales. If the Stokes number is low the particle follows the fluid as a tracer, while if the Stokes number is high the particle is not bound to the fluid motion and is acting as a ballistic particle in the inertial state (Burgisser *et al.*, 2005).

The same notions of a particle response timescale relative to the behavior of the carrier phase emerge in dense multiphase flow (Cassar *et al.*, 2005; du Pont *et al.*, 2003). The premise is that particles exist in a granular framework where particle-particle contacts are idealized as points, and where force is collectively transmitted in a “granular continuum.” The mechanical connection between a particle and its neighbors is quantified by the particle coordination number,  $Z$ , which is a count of all the contacts between a particle and its neighbors. Conceptually, this granular continuum plays the same role in controlling the macroscopic scales as the fluid in dilute flows. Now if the granular framework is sheared, a particle can be displaced from its initial position and coordination state by macroscopic forces working against a microscopic restoring gravitational force (or some general restoring pressure for neutrally buoyant crystals), which will act to return it to the previous location. If the macroscopic forces acting on the particle carry it beyond its original location before the particle can reestablish contact with its neighbors in the granular continuum, the coordination number will approach zero. In this scenario, the particle is effectively an inertial or ballistic particle (even at low particle-Reynolds number), with respect to the granular continuum, just as in the dilute case.

This leads to a disassociation of the granular continuum, a reduction in the local particle volume fraction and a decrease in the number density of force chains.

The particle-fluid coupling can be quantified by the value of a Viscous number ( $I_v$ ) where it is assumed that the particle response time is governed by viscous forces (Ness & Sun, 2015; Trulsson *et al.*, 2012):

$$I_v = \frac{3\mu_l\dot{\gamma}}{2(\rho_c - \rho_l)gd_c} \quad (2.4)$$

Here  $\mu_l$  is the dynamic viscosity of the liquid,  $\dot{\gamma}$  is the local shear rate of the liquid (calculated at the computational cell-scale),  $\rho_c$  and  $\rho_l$  are the densities of the crystals and liquid, respectively,  $g$  is the gravitational acceleration, and  $d_c$  is the diameter of the crystals. As in dilute flows, a value of  $I_v \ll 1$  indicates that the particle will recover from any perturbation and reestablish contact with the granular surroundings, and enduring frictional contacts are the primary means of force transmission. If  $I_v \gg 1$  the particles lose contact with their neighbors, the granular mixture is disassociated, and particle interactions are primarily collisional; the multiphase mixture becomes a dilute granular flow. The Viscous number ignores numerous microphysical processes such as pore pressure and fluid transport through the adjacent granular media, dissipation associated with lubrication, non-spherical particle shape, non-ideal point contacts (with non-zero surface area), etc.

The granular state of the system at one time step is shown in Figure 2.3, which represents the same time step in Figure 2.2e and 2.2f. The location of the mixing bowl is outlined by red dashed lines. The background image illustrates the magnitude of the Viscous number on a logarithmic scale. The white lines represent equal volume fractions of fluid and particles ( $\varepsilon_c = 0.5$ ). In general,  $\varepsilon_c > 0.5$  on either side of the contour within the mush, and  $\varepsilon_c < 0.5$  in the chimney,

fluidized region, and crystal-free portion at the top. An exact value for  $\varepsilon_{c,c}$  has not been determined for our system, but the naturally settled bed of monodisperse crystals has an average particle fraction of 0.58, within the critical range for the transition found by Ness & Sun (2015). (polydisperse crystals with respect to size and shape will have a different average packing). Many of the crystals are in pockets of hexagonal packing, but variations from the initial random settling create thin regions of lower particle fractions (Figure 2.2b). These thin regions might represent volume fractions less than  $\varepsilon_c$ , but the dominant behavior of the mush outside of the mixing bowl is quasi-static, so we choose to illustrate a particle fraction of 0.5. The regions with the highest values of  $I_v$  also have particle fractions of 0.1 or less, corresponding to the dilute granular regime. Regions of the system with higher values of  $I_v$  vary through time as liquid in the chimney rises in pulses and meanders through the mixing bowl.

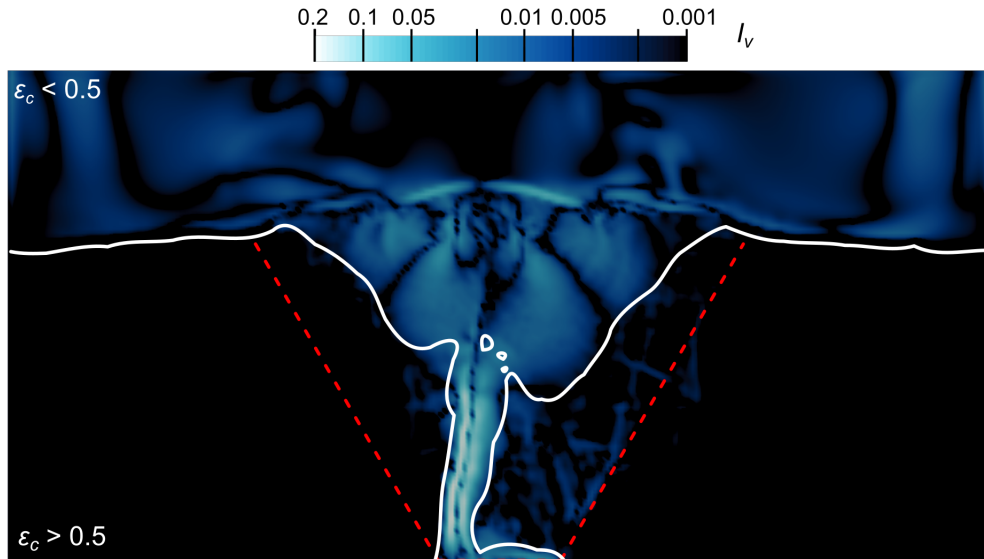


Figure 2.3. The Viscous number of the intrusion at  $t^*=1.48$  (Figure 2.2e and 2.2f). Red dashed lines show the mixing bowl and white lines represent equal volume fractions of liquid and crystals ( $\varepsilon_c = \varepsilon_l = 0.5$ ).  $I_v$  is illustrated by shades of blue, represented with a logarithmic scale.

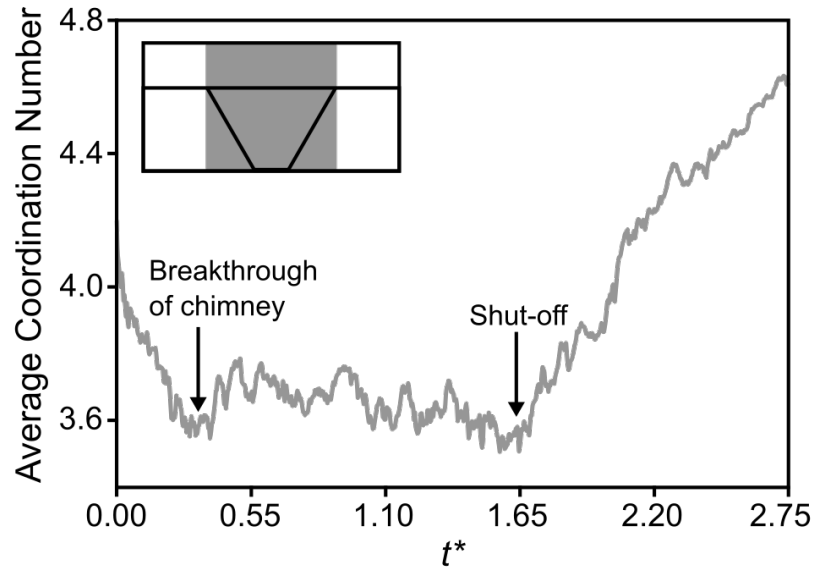


Figure 2.4. Average coordination number for crystals within the lateral extent of the mixing bowl (shown as grey box in the inset image) through time. The maximum coordination number for the monodisperse crystals is six, representing hexagonal packing. Also labeled are the times when the crystal-poor chimney breaks through the top of the crystal mush, and the timing of the end of the intrusion when the melt supply is shut off.

The coordination number,  $Z$ , is a measure of the availability of a particle to transmit and dissipate energy by collisional and frictional interactions. The porosity shown in Figure 2.2 is a cell-averaged property and is not a complete description of the local granular state of the system. Figure 2.4 shows the average coordination number as a function of scaled time, with  $t^*=(U_0/H_0)t$  for the simulation (Movie 2.2). Three distinct phases can be seen that correspond to the three stages described above: a transient start-up period where progressive fluidization produces dilation and a reduction in the coordination number, a quasi steady phase where the dissipation fluctuates around an average indicating both hydrodynamic and granular modes of dissipation, and the re-establishment of the granular state once the intrusion ceases. Note that during the collapse of the mixing bowl after the shut-off, the coordination number increases over the original value of the settled bed, reflecting the sensitivity to packing from settling to the proximity of other crystals. Lastly Figure 2.4 shows the coordination number has a high-

frequency component over-printing the long wavelength temporal behavior. Although our sampling density is not sufficient to do a spectral analysis, we suggest that the high-frequency component may reflect the stochastic “chatter” produced by force chains forming and dissipating as a result of the unsteadiness in the driving fluid flow. Hence it provides a window into the microscale mechanics that recovers a time-dependence not apparent in the velocity for example.

Previously, multiphase models for magma dynamics have employed a model for multiphase flow that is an extension of continuum models. Hence it might seem reasonable to represent the dynamics of the open-system event as a reduced system by invoking either a granular-fluid constitutive model (Boyer *et al.*, 2011) or a mixture continuum rheology with a suspension viscosity. However Figure 2.3 illustrates the challenges in trying to describe the dynamics in those contexts. The shear rate varies in time and space, and a local pressure as required by the model of Boyer *et al.* (2011) is not uniquely defined. Even in regions with low values of  $I_v$ , there is still local phase-relative-motion and mixing (Schleicher *et al.*, 2016). Extending the granular rheology approach to a non-local constitutive model (Kamrin & Koval, 2012) still requires an assumption of locally steady conditions which are not obtained in our results, nor likely to be found in nature. Comparisons between our DEM results and a continuum model for the same system (not shown here) with a yield strength and suspension rheology did not recover the same kinematic template as the higher resolution DEM model, and produced results that were significantly different in the distribution of strain, mixing and particle transport. This exposes the limitations of the suspension rheology approach in high-particle fraction systems and reaffirms the importance of resolving the micro-granular mechanics to adequately address the mechanics of crystal-rich magma mushes.

## 2.6 THE CRYSTAL RECORD OF THE OPEN-SYSTEM EVENT

Much of the evidence for open-system magmatic events comes from processes recorded at the crystal scale, such as zoned crystals and the existence of diverse crystal populations (Costa *et al.*, 2010; Kahl *et al.*, 2011, 2013; Viccaro *et al.*, 2016; Wallace & Bergantz, 2002). When crystals encounter magmatic environments of changing chemical potential, they can respond by growth, recording the changes through chemical zoning, or by dissolution, producing resorption features in the crystals. Open-system mixing can also bring together distinct crystal populations formed by crystals with different reaction histories.

Our particle-based simulations enable us to track crystals and the liquid in which they reside during the open system intrusion. This capability recovers the crystal gathering and dispersal dynamics. To illustrate crystal transport and reaction during an open-system event, we monitored three pairs of crystals that are proximal at the final time step of the simulation (Figure 2.5, supplemental Movie 2.3). These pairs represent crystals that would be adjacent in a thin section of a volcanic or plutonic sample. Figure 2.5a shows the trajectories of the three pairs of crystals throughout the simulation. White circles outlined in black indicate the initial locations of each crystal, and black circles outlined in white show the final position of the three crystal pairs. The grey band at the bottom illustrates the location of the intrusion, and white dotted lines represent the mixing bowl. The image in the background is the final time step of the simulation showing the mixing between the resident (black) and intruded (white) melts.

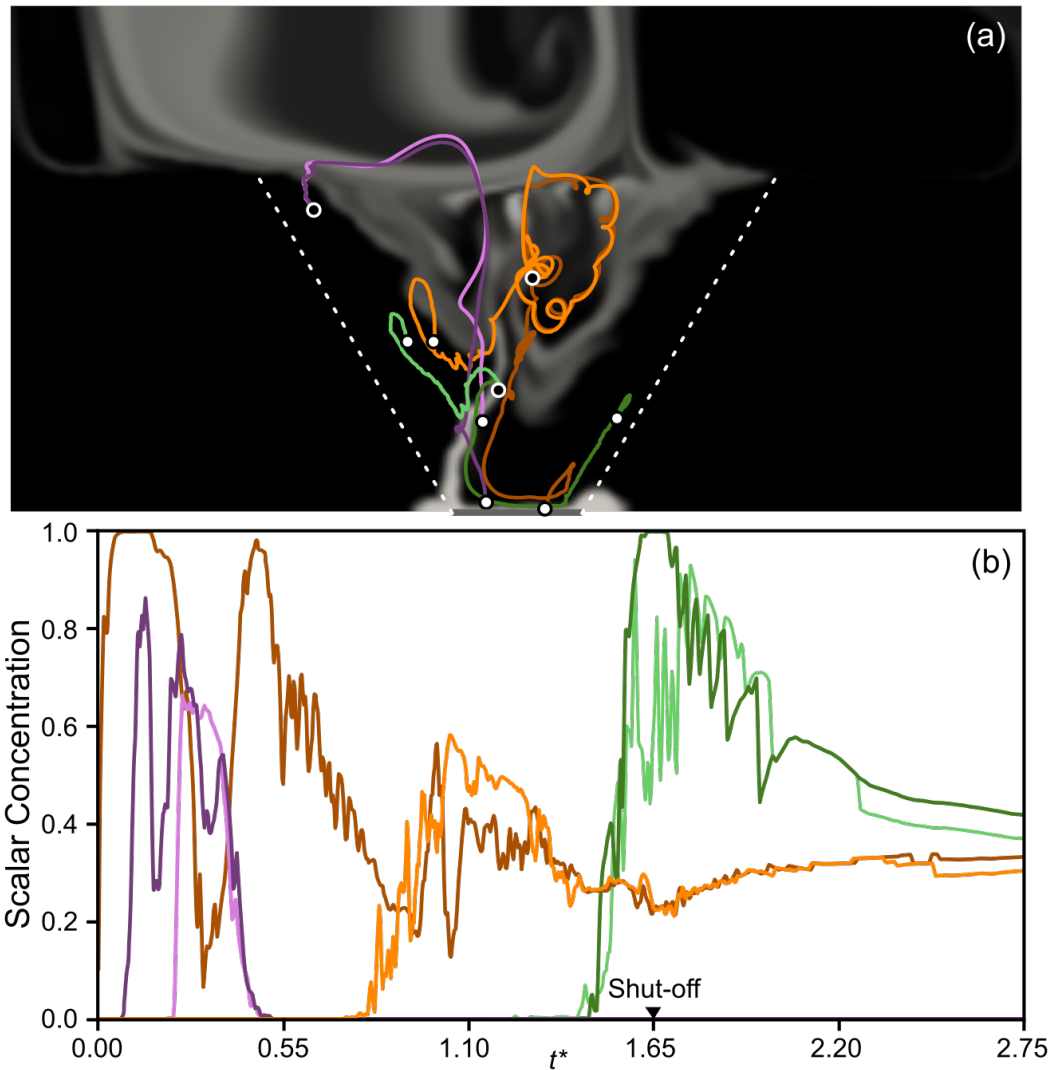


Figure 2.5. (a) Trajectories of 3 pairs of crystals monitored during the simulation. White circles with black outlines illustrate starting location for all crystals, and black circles with white outlines show the ending location of each crystal pair. White dashed lines show the mixing bowl. Resident (black) and intruding (white) liquids during the final time of the simulation are shown in the background. (b) The composition of the liquid scalar in which each of the crystals reside. Resident liquid has a scalar concentration of 0; intruding liquid has a value of 1. The arrow at  $t^*=1.65$  shows the end of the intrusion.

Monitoring the three pairs of crystals also illustrates the potential diversity in liquid composition a crystal could encounter during an open-system event (Figure 2.5b). The changing liquid composition is associated with a liquid scalar, which represents variations in temperature or chemical composition between the incoming and resident magmas. The liquids in our



simulation have been shown to have negligible changes in thermophysical properties, but maintain their compositional distinctions and potential for reaction, so the scalar simply expresses the proportions of intruding and resident liquids with values between zero and one: zero is the resident liquid (black), one is the intruding liquid (white), and values between zero and one are a mixture of the two liquids. Mixing takes place by both advection and chemical diffusion, and the diffusion equation is described in the Supplementary Text (Section 2.9). The horizontal axis is the non-dimensionalized time of the simulation, with  $t^*=(U_0/H_0)t$ . The arrow at  $t^*=1.65$  indicates the end of the intrusion.

The differences in the scalar concentrations encountered by the three pairs of crystals reflect the sensitivity to initial position and the kinematics of subsequent mixing. The purple crystals are initially directly above the intrusion, and are carried up through the mixing bowl by the fingering instabilities that eventually form the crystal-poor chimney. This is the only period of time when they encounter the intruding liquid. Once they reach the top of the mixing bowl, the purple crystals are deposited into the quasi-static edges of the mixing bowl, where little crystal-crystal and crystal-liquid relative motion occurs for the duration of the intrusion and resettling. The green crystals are initially on the edges of the mixing bowl, where the crystal-liquid faults form. Both crystals' motions roughly parallel the faults, first moving upwards as the mush expands to accommodate the intruding liquid, and then downwards as crystals slide down the faults to replace the central crystals entrained by the chimney. The green crystals only encounter the chimney liquid near the end of the intrusion, and approach a mixed scalar concentration of  $\sim 0.4$  as the crystals settle back into the mixing bowl.

The orange crystals encounter a greater diversity of granular regimes than the purple and green pairs. The dark orange crystal initially encounters the intruding liquid, but is left at the base when

the instability that carries it merges into the central chimney. Eventually it is entrained in the chimney, but its trajectory is not straight due to the varicose instabilities of the rising liquid. During this time, the light orange crystal remains in the quasi-static regime, traveling downwards through the mixing bowl until the chimney entrains it as well. Both orange crystals enter the dense, granular vortices, where they travel through the upper portion of the mixing bowl together, experiencing a full rotation. The dilute and dense regimes of the mixing bowl in this region promote crystal-crystal-liquid mixing, giving a final scalar concentration of  $\sim 0.3$  for the orange crystals. This value is lower than the green crystals residing near the fossil chimney liquid, which did not mix as thoroughly with the resident liquid.

We can use the variable scalar compositions encountered by the different crystals to determine what the crystals could record during the single open-system intrusion. We use the approach of Chen & Zhang (2008) (based on the work of Kerr (1995)) to calculate the convective reaction rate of two crystals as they encounter the intruding liquid during the simulation. As a crystal moves through a liquid with changing physicochemical conditions, a compositional boundary layer forms around the crystal. In convective reaction, the relative velocities of the crystal and liquid determine the thickness of the boundary layer, rather than a time-dependent boundary layer in the case of diffusion-controlled dissolution (Donaldson, 1985). Within the boundary layer, crystal reaction is controlled by the difference in timescales of diffusive mass transfer and interface reaction (Chen & Zhang, 2008). While this model of reaction is most simply described as dissolution, it can also be applied to crystal growth. However, crystal growth is complicated by the possibility of simultaneous growth on existing crystals and the nucleation of new crystals, which would produce different crystal size distributions and clustering (Špillar & Dolejš, 2013,

2014). Should the reaction rate be negative (indicating growth), it is assumed growth occurs only on pre-existing crystals.

To determine the olivine reaction rate, we use the MgO concentration in the crystals and liquid for the equilibrium-determining component as in Chen & Zhang (2008). We use the MELTS software (Gualda *et al.*, 2012) to calculate the equilibrium MgO weight percent in olivine crystals and basaltic liquid at a temperature 50°C colder than the liquidus, with the basalt starting composition from Rhodes (1995). The resident liquid and crystals are assumed to initially be at this lower temperature, and the intruding liquid is at the liquidus temperature. Over the temperature range considered, the density difference is only 0.6% so we use a constant density for the liquids. Numerical simulations with heat transfer (not shown) indicate there is little thermal inertia or thermal-chemical decoupling, so we use the scalar value tracking the intruding liquid as a proxy for the temperature of the liquid. We calculate the temperature using a linear relationship between the scalar concentration and temperature; a scalar value of zero has the temperature of the resident liquid, while a value of one represents the liquidus temperature. The results from MELTS provide a linear relationship between temperature and MgO composition, and we use this relationship to estimate the far-field liquid composition in which the crystals reside at every time step.

The convective reaction rate is given by Chen & Zhang (2008) as:

$$u = \frac{\beta D}{\delta} \tag{2.5}$$

which is composed of the diffusivity ( $D$ ) of the equilibrium-determining component (here MgO) and the compositional boundary layer thickness ( $\delta$ ). The boundary layer thickness is determined by the relative velocity between the crystal and the surrounding liquid, and the diffusivity of the

equilibrium-determining component (MgO) in the liquid (see Equations 7-10 in Chen & Zhang (2008)). The boundary layers calculated the simulation range between  $\sim 10^{-5}$ - $10^{-4}$  m. Also included in the convective reaction rate is a dimensionless parameter ( $\beta$ ) that determines crystal growth or dissolution (negative or positive value, respectively):

$$\beta = \frac{\rho_l (C_0 - C_\infty)}{\rho_c (C_c - C_0)} \quad (2.6)$$

This parameter depends on the densities of the liquid ( $\rho_l$ ) and crystal ( $\rho_c$ ), the MgO weight percent in the liquid within the crystal-liquid interface ( $C_0$ ), the far-field (i.e. the liquid computational cell) MgO weight percent ( $C_\infty$ ), and the MgO weight percent in the crystal ( $C_c$ ). We use the thermometer of Putirka (2008, Equation 13) to calculate the interface liquid composition as a function of temperature ( $T$ ), which is independent of pressure and the compositions of the far-field melt and crystal:

$$C_0 = \frac{T - 994.4}{26.3} \quad (2.7)$$

To apply this approach to our simulation, we assumed the crystals were initially in equilibrium with the resident liquid (i.e.  $C_0 = C_\infty$ ). However, the interface melt composition is independent of the composition of the crystals and the external melt (Equation 2.7), and because of this produces disequilibrium conditions when the crystals are stationary within the resident melt. The reaction rate calculation (Equation 2.5) is for convective reaction, therefore stationary crystals require a convection-free model that is beyond the scope of this study (Chen & Zhang, 2008; Liang, 2000). We only apply the calculation to crystals that are continuously moving relative to the liquid (the orange crystals from Figure 2.5). The light orange crystal does not

encounter the intruding liquid during the beginning of the intrusion, so we set the crystal reaction rate to zero during this time.

The results of the reaction calculation for the two orange crystals are shown in Figure 2.6. Both crystals experience positive reaction rates, indicating they only undergo dissolution when interacting with the intruding liquid. During the simulation, the dark orange crystal would dissolve a total of  $0.38 \mu\text{m}$  from the rim, while the light orange crystal, which encountered the intruding liquid later in the simulation, would dissolve  $0.25 \mu\text{m}$ . The high frequency variations in the crystals' dissolution rates are due to the changing scalar concentration (see Figure 2.5b) and relative velocity between each crystal and the surrounding liquid. Despite being highly variable, the relative velocities are low, with Reynolds numbers between  $\sim 10^{-4}$ -1. The average rates of dissolution for the examined crystals are  $13.7 \mu\text{m/hr}$  for the dark orange crystal, and  $12.6 \mu\text{m/hr}$  for the light orange crystal during the time it encountered the intruding liquid. Assuming constant dissolution rates with these averages, the  $2 \text{ mm}$  radius crystals would dissolve fully after  $\sim 6$ -7 days.

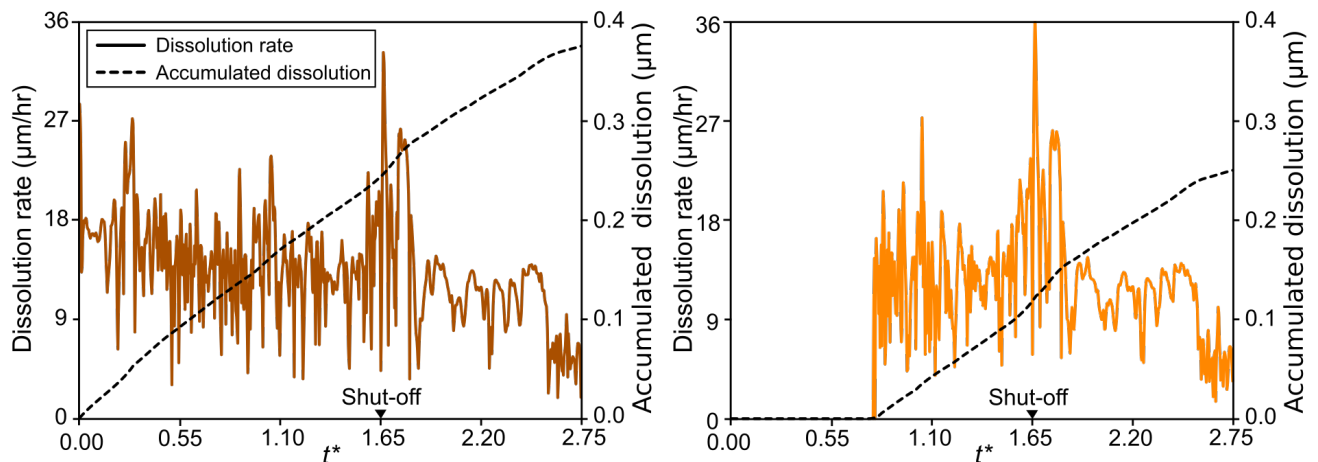


Figure 2.6. Dissolution experienced by the orange crystals from Figure 2.5. Solid light and dark orange lines show the dissolution rate that each crystal experiences during the simulation. Dashed black lines show the accumulated dissolution rate the both crystals experience during the simulation. The arrow at  $t^*=1.65$  shows the end of the intrusion.

The convective reaction rates calculated from the simulation fall within the range of rates from previous experiments and theoretical calculations for similar temperatures and compositions. Experiments by Donaldson (1985) gave dissolution rates for olivine at near-liquidus temperatures of 9-14  $\mu\text{m/hr}$ . Liang (2000) calculated theoretical rates for olivine solid solution diffusion-controlled (rather than convection-controlled) dissolution of  $\sim 3\text{-}36 \mu\text{m/hr}$ . The rates we calculate are lower than the hypothetical dissolution rate of 52.6  $\mu\text{m/hr}$  calculated by Chen & Zhang (2008), who considered a crystal falling in a melt with a constant, disequilibrium composition. The crystal and liquid compositions chosen for the example in Chen & Zhang (2008) represent a larger disequilibrium than the compositions in this study, which explains the faster dissolution rates. We conclude the rates calculated for the crystals represent realistic values when reacting by convective dissolution to the intruding liquid.

The reaction rates for the orange pair of crystals represent crystal dissolution when they encounter the intruding liquid. However, natural crystals can have reversely zoned rims, indicating the rims grew from a more primitive liquid prior to eruption. For crystal growth to occur in our simulation, the far-field composition of the melt ( $C_\infty$ ) would need a higher MgO content than that of the interface liquid ( $C_0$ ). These quantities are both calculated as functions of temperature (from MELTS and Equation 2.7), and for a given temperature,  $C_0$  is always greater than  $C_\infty$ . In the presented simulations, the crystal, interface liquid, and far-field liquid are at the same temperature, making crystal growth impossible. However, if the thermal inertia of a crystal were considered, it is possible for a crystal encountering a higher temperature far-field liquid to generate a thermal (and therefore, compositional) gradient that would promote crystal growth. This hypothesis requires additional simulations that include heat transfer to monitor the temperatures of the crystals and far-field liquid separately.

## 2.7 GEOLOGICAL IMPLICATIONS OF THE OPEN-SYSTEM MODEL

While our CFD-DEM model of intrusion of a melt into an olivine mush is highly simplified, we offer some tentative implications of the modeling that may illuminate conditions found in natural examples. The primary benefits of using CFD-DEM arise from the resolution of small-scale crystal-crystal mechanical interactions, and the tracking of individual crystal trajectories and response as mixing proceeds.

The resolution of crystal-scale interactions allows for extreme strain localization and frictional behavior to be modeled. It is this behavior that produces the distinct morphology of the mixing bowl. And similar processes operating in a mush may produce the frequent observation of cryptic internal contacts in plutons, which are often rootless in the sense that they do not obviously connect with any through-going externally derived tectonic feature. Rather, these features juxtapose elements of a crystal-mush with itself, producing cross-cutting looking features but without substantial changes in mode (Paterson, 2009). Hence any external or internal process that can produce pressure changes such that some fluidization can locally occur, releasing frictional crystal contacts, may produce what is recognized in the field as a contact. That contact itself may not have any significance in the sense of magmas that are temporally discordant and originate elsewhere. The simulations suggest that in hydrogranular systems like a crystal mush, frictional forces are to be expected and strain localization common. Hence models which invoke a continuum assumption to describe geological observations are not adequate for crystal-rich systems, perhaps to even as low as 30% crystallinity, and describing crystal-rich transport with notions taken from simple fluid dynamics as in Glazner, (2014), are inadequate to illuminate the diversity of behavior encountered in natural examples.

Another feature of the mixing process described above (also see Schleicher *et al.* (2016)) is that new magma injections interact with the mushy reservoir in a pulsating fashion. The fact that enclaves are very common in silicic rocks, but their feeder systems are rarely recognized suggests that the production of discrete enclaves and the “digestion” or break-up of their feeder system happens simultaneously. As seen in Figure 2.2, the pulsating mechanical response of the mush bifurcates the incoming magma. If the host magma was silicic and the incoming magma mafic and subject to chilling to produce a stable but ductile rind, this process would produce enclaves, and erase the distinct dike-like character of the feeder zone as suggested in Figure 2.2g. The simulations of crystal chemical response to open-system input, while highly simplified, make it clear that caution is warranted when using the crystal record of open-system events to infer distinct mixing episodes; the interested reader is directed to Schleicher *et al.*, (2016) for more discussion of mixing systematics. Although we consider only a few crystals here as proof of concept examples, even in this highly simplified scenario the crystal cargo is incredibly diverse. And although we are not in a position yet to offer quantitative statistical guidelines to address sample ergodicity in resolving distinct open system events, it is to be expected that proximal crystals will likely have discordant reaction time-series.

## 2.8 CONCLUSIONS

The presented simulation illustrates the localized response of a crystal-rich mush to an open-system intrusion. The emergence of the fluidized mixing bowl confines crystal and liquid mixing to this region, while the surrounding mush is relatively unaffected. Little to no intruded liquid passes through the mush into the overlying reservoir without some mixing with the resident liquid due to vertical transport and overturn in the mixing bowl. The self-similarity of the mixing bowl indicates that different intrusion rates or mush characteristics (e.g. liquid and crystal



composition, mush height, intrusion width) would generate a similar fluidized region, as long as the intruding liquid exceeds the minimum fluidization velocity of the mush. Prolonged intrusion could increase the lateral extent of the mixing bowl as crystals erode along the crystal-liquid faults, but the overall geometry would persist.

Although the simulation represents a geologically simple system, we document the mechanical and compositional diversity that can arise from an open-system intrusion. The mixing bowl and surrounding mush contain a variety of hydrogranular regimes, reflecting the changes in local crystal fraction and coordination number. The variation in these regimes leads to non-affine crystal and liquid motion within the mixing bowl. Crystals that are proximal at the end of the intrusion may have followed different trajectories through the mixing bowl and reacted with a variety of liquid compositions. While the tracked crystals in our simulation undergo only dissolution when reacting with the intruding liquid, natural systems with variable liquid temperatures and compositions could produce a complex crystal cargo, even from a single open-system event.

## 2.9 SUPPLEMENTARY TEXT

This supplementary text includes details of three supplementary movie files. It also provides details of the simulation methods, which include the model theory and governing equations, simulation initialization, and code validation.

### 2.9.1 *Supplementary movies*

Movie 2.1: movie of Figure 2.2, showing the simulation of the open-system intrusion into the crystal-rich mush. The left shows the crystals and liquids, and the right shows the corresponding crystal volume fraction.

Movie 2.2: The same simulated intrusion as Movie 2.1, but the crystals are colored based on their coordination number. Values range from one, representing crystals touching only one other crystal, to six where crystals are in hexagonal packing. Figure 2.4 shows the average coordination number of crystals within the indicated region (see Figure 2.4 inset) through time, calculated from this movie.

Movie 2.3: The same simulation as Movies 2.1 and 2.2, highlighting the crystals monitored in Figures 2.5 and 2.6. The three pairs of crystals have been shown with the same colors in these figures, but are 2.5 times larger than their actual size to increase their visibility.

## 2.9.2 *Simulation methods*

### 2.9.2.1 Multiphase fluid simulation theory and algorithm

We performed simulations using a modified version of the MFIx (Multiphase Flow with Interphase eXchange) numerical algorithm developed by the DoE supported National Energy and Technology Laboratory. It simulates multiphase flow by employing discrete element method-computational fluid dynamics (DEM-CFD). This is a Lagrangian-Eulerian approach for solid (crystal) and fluid (liquid) phases, respectively, where crystal phases are explicitly resolved and the liquid phase is treated as a continuum. This method allows us to model hydrodynamic, hydrodynamic-to-crystal, crystal-to-hydrodynamic and crystal-to-crystal interactions, that is, the so-called 4-way coupling. Collisions, sustained frictional contact, buoyancy, fluid drag and interphase momentum transport between phases are directly resolved with the soft-sphere approach, using a spring-and-dashpot system to model the contact forces (Cundall & Strack, 1979). The MFIx DEM-CFD algorithm has been verified and validated (Garg *et al.*, 2012a, 2012b; Li *et al.*, 2012) including the physical effects of chemical reactions (Li & Guenther,

2012); validation is discussed in detail below. Our simulations were run on the Stampede Cluster at the Texas Advanced Computing Center (TACC).

### 2.9.2.2 Governing equations

The liquid phase is described with the governing equations for mass and momentum conservation:

$$\frac{\partial \varepsilon_l \rho_l}{\partial t} + \nabla \cdot (\varepsilon_l \rho_l \mathbf{v}_l) = 0 \quad (2.8)$$

$$\frac{D}{Dt} (\varepsilon_l \rho_l \mathbf{v}_l) = \nabla \cdot \overline{\overline{S}}_l + \varepsilon_l \rho_l \mathbf{g} - \mathbf{I}_{lc} \quad (2.9)$$

Here,  $\varepsilon_l$  is the volume fraction of the liquid phase,  $\rho_l$  is the liquid density,  $\mathbf{v}_l$  is the liquid phase velocity vector,  $\mathbf{g}$  is the gravitational acceleration,  $\mathbf{I}_{lc}$  is a coupling term that involves the transfer of momentum between the liquid and crystal phases, and  $\overline{\overline{S}}_l$  is the liquid-phase stress-tensor, given by:

$$\overline{\overline{S}}_l = -P_l \overline{\overline{I}} + \overline{\overline{\tau}}_l \quad (2.10)$$

$$\overline{\overline{\tau}}_l = 2\mu_l \overline{\overline{D}}_l + \lambda_l \text{tr}(\overline{\overline{D}}_l) \overline{\overline{I}} \quad (2.11)$$

$$\overline{\overline{D}}_l = \frac{1}{2} \left[ \nabla \mathbf{v}_l + (\nabla \mathbf{v}_l)^T \right] \quad (2.12)$$

$P_l$  is the liquid-phase pressure,  $\overline{\overline{I}}$  is the identity matrix, and  $\overline{\overline{\tau}}_l$  is the liquid-phase shear stress tensor.  $\mu_l$  and  $\lambda_l$  are the dynamic viscosity and second coefficient of viscosity for the liquid phase, and  $\overline{\overline{D}}_l$  is the strain rate tensor. The second coefficient of viscosity is typically small but included here for completeness.

An advection-diffusion equation is employed to model transport of a scalar attached to the liquid phase. This scalar acts as an inert tracer of a compositional field associated with new magma and is shared by mixing between the resident and incoming liquids:

$$\frac{\partial}{\partial t}(\varepsilon_l \rho_l C_l) + \nabla \cdot (\varepsilon_l \rho_l \mathbf{v}_l C_l) = \nabla \cdot (D_l \nabla C_l) \quad (2.13)$$

Here  $C_l$  is the concentration of the liquid scalar and  $D_l$  is the diffusion coefficient for the scalar in the liquid phase. The cation diffusivity in basaltic melts is typically of order  $10^{-10}$  m<sup>2</sup>/s (Richter *et al.*, 2003). This produces a scalar Peclet number of at least order  $10^5$  for the most active regions of flow for the duration of the simulations. Therefore, the scalar diffusivity was set to zero with no noticeable change in the scalar field. Hence modeled variations in the scalar field are entirely due to advective mixing and numerical diffusion. We did not quantify the effects of numerical diffusion on scalar mixing.

The crystals in the simulation are Lagrangian particles, with coupled equations solved for individual crystals at each time step. The position of the crystals and their linear and angular momentum are calculated according to Newton's Laws:

$$\frac{d\mathbf{X}^{(i)}(t)}{dt} = \mathbf{V}^{(i)}(t) \quad (2.14)$$

$$m^{(i)} \frac{d\mathbf{V}^{(i)}(t)}{dt} = \mathbf{F}_T^{(i)}(t) = m^{(i)} \mathbf{g} + \mathbf{F}_d^{(i \in k)}(t) + \mathbf{F}_c^{(i)}(t) \quad (2.15)$$

$$I^{(i)} \frac{d\boldsymbol{\omega}^{(i)}(t)}{dt} = \mathbf{T}^{(i)}(t) \quad (2.16)$$

The superscript  $(i)$  represents each crystal within the domain,  $\mathbf{X}^{(i)}(t)$  is the crystal position,  $\mathbf{V}^{(i)}(t)$  is the crystal linear velocity, and  $m^{(i)}$  is the  $i^{\text{th}}$  crystal's mass.  $\mathbf{F}_T^{(i)}(t)$  is the sum of the forces

acting upon the  $i^{th}$  crystal,  $\mathbf{F}_d^{(i \in k)}(t)$  is the total drag force on the  $i^{th}$  crystal in the  $k^{th}$  liquid cell, and  $\mathbf{F}_c^{(i)}(t)$  is the contact force from interactions with other crystals. The equation for angular velocity,  $\boldsymbol{\omega}^{(i)}(t)$ , includes the  $i^{th}$  crystal's moment of inertia  $I^{(i)} = \frac{m^{(i)}d_c^{(i)}}{10}$  and the sum of the torques  $\mathbf{T}^{(i)}(t)$  acting on the  $i^{th}$  crystal.

Additional details of the implementation of the spring-and-dashpot model for calculating collisional forces used in MFIX can be found in the documentation of the MFIX-DEM algorithm (Garg *et al.*, 2012b). The values of the crystal-crystal coefficient of friction, restitution, and spring constant required for DEM are 0.1, 0.1, and  $10^5$  kg/s<sup>2</sup>, respectively. The sensitivity of model outcomes to the choice of DEM parameters depends on the dynamic regime considered (Paulick *et al.*, 2015) although it has been noted particle dynamics in fluidized beds are not very sensitive to the choice of DEM contact parameters (Tsuji *et al.*, 1993). The coefficients of friction ( $\mu_f$ ) for non-compacted, olivine crystals in melt have never been measured. Hence we assessed the sensitivity of both the quasi-static and fully-fluidized model results to variations in contact friction from values of 0.03 to 0.5. Neither the quasi-static results, the formation of fluidized granular eddies, nor the mixing characteristics changed significantly over this interval, so a value of 0.1 was used.

For brevity we do not repeat the development of the DEM model in-depth where the restitution coefficients and spring constants are defined; the interested reader is directed to Garg *et al.* (2012a, 2012b). The value of the restitution coefficient ( $e$ ) changes for collisions of particles in a viscous liquid, as shown by experimental results (Yang & Hunt, 2006). The authors defined a parameter called the binary Stokes number for colliding particles in a viscous liquid:

$$St_B = \frac{m^*(U_1 - U_2)}{6\pi\mu_l(r_c^*)^2} \quad (2.17)$$

where  $m^*=(1/m_1+1/m_2)^{-1}$  and  $r_c^*=(1/r_1+1/r_2)^{-1}$  are the reduced mass and radius of the two particles in the collision, respectively,  $(U_1-U_2)$  is the relative approach velocity of the particles, and  $\mu_l$  is the fluid dynamic viscosity. The restitution coefficient of two colliding particles increases with increasing  $St_B$ . Our simulations generate  $St_B \ll 1$ , therefore based on the empirical data of particle-particle and particle-wall interaction in a viscous fluid the choice of  $e = 0.1$  is appropriate (Yang & Hunt, 2006).

The values used for the particle stiffness coefficients ( $k_n, k_t$ ) are smaller than those of the natural materials because using the actual values incurs simulation times that exceed any practical limits. However it has been shown in validation studies that reducing the particle stiffness coefficients (spring constants) does not produce measureable error, and this is common practice throughout the CFD-DEM community (Nakamura & Watano, 2007). A DEM study (Coetzee & Els, 2009) demonstrated that particle stiffness coefficients below  $10^5 \text{ kg/s}^2$  resulted in variable internal friction angle within the granular material. However, for  $k_n$  values at and above  $10^5 \text{ kg/s}^2$  and low particle friction coefficients ( $\mu_f < 0.2$ ), the angle of internal friction did not vary as a function of stiffness coefficient. We also performed a sensitivity study of the stiffness coefficients and found values that satisfy validation and do not give unrealistic compaction of the particle bed.

### 2.9.2.3 Simulation initialization and properties

The simulations are 2.5-D, with the third dimension equaling the width of a crystal. Our simulation is for a dike-like body whose long dimension is into-and-out-of the plane of the domain, so 3-D edge effects are ignored and the liquid motion is governed by the quasi-2-D

geometry. Accurate resolution of both the liquid and crystal dynamics requires that the liquid continuum grid-cell size has to be less than 1/19.3 of the domain size, and larger than 1.63 crystal diameters (Peng *et al.*, 2014). We performed grid resolution studies and found that at a grid cell of 2.5 crystal diameters gave stable and reproducible results. The number of crystals is well above the minimum required to recover scalable, ensemble-averaged behavior (Ness & Sun, 2015).

The injection rate used in the simulation falls within the range of magma ascent rates of  $10^{-4}$ - $10^1$  m/s for volcanoes in a range of tectonic settings as estimated by geochemical, petrographic, and geophysical studies (Girard & Stix, 2009; Parks *et al.*, 2012; Rutherford, 2008). Specifying the intrusion rate is appropriate for modeling open-system events driven by momentum, rather than by thermal or compositional buoyancy. This choice of input style is motivated by the common occurrence of a complex crystal cargo in mixed magmas, with crystal clots, rapidly created disequilibrium features, and evidence for near instantaneous mingling of large volumes of magma (Costa *et al.*, 2010; Davidson *et al.*, 2001; Wallace & Bergantz, 2005), all of which indicate that many open-system events are strongly forced and can undergo mixing and mingling. In addition many open-system events have evidence that the open-system process has sufficient energy to overcome viscosity barriers producing mingled magmas with crystal transfer (Ruprecht *et al.*, 2012) as well as evidence of crystals transported out of a crystal mush which requires fluidization.

Solid boundaries have a no-slip boundary condition for the fluid and a wall-friction law for the crystals, but the majority of fluid and particle motion occurs far from the walls, so boundary conditions have little influence on the dynamics.

#### 2.9.2.4 Code validation

The validation of numerical models of dense multiphase mixtures is challenging. This is because granular-fluid mixtures are usually opaque, making optical measurements of laboratory experiments difficult. Inserting instruments into experimental systems would interfere with the flow field by particle-instrument interactions. In addition, the large number of degrees of freedom and many-body interactions produce emergent behavior, non-local and non-affine deformation such as shear-localization, dilatancy and jamming, all of which are not always repeated in duplicate experiments. Laboratory experiments can have multi-modal grain sizes with variable density and roughness, which is hard to duplicate in a numerical model for validation. Hence validation of numerical models for dense multiphase systems is usually based on the statistics of many realizations from an experimental test-bed that recovers the largest scales of the dynamics such as the global properties of mixing, pressure-drop, bed-height, or other measures of system-scale, granular ensemble behavior.

Numerous exercises have been previously performed on the MFIX-DEM code as validation studies (Li *et al.*, 2012). This has included quasi-static granular flow such as run-out to reproduce the repose angle of glass beads, and under more dynamic conditions, simple multiphase shear flow, particle segregation and unmixing, as well as fully fluidized states. MFIX-DEM results and analog experiments gave very good agreement across the entire dynamic range. However we also developed validation exercises.

As our simulations exemplify a dynamic cycle from static to fully-fluidized, we must demonstrate validation for both these states. The Viscous number,  $I_v$ , and critical particle volume fraction,  $\varepsilon_{c,c}$ , framework (defined in the main text) provide a basis for identifying which dynamic regime and validation protocols are appropriate (Ness & Sun, 2015). The Viscous number is zero in the initial quasi-static regime where the volume fraction is near critical at the random packing



of approximately 0.6. In the fully fluidized regime the Viscous number is variable with values spanning more than an order of magnitude and with a variable crystal volume fraction that is below the critical crystal volume fraction.

The validation of the initial quasi-static state where the mixing bowl is first formed was based on replicating the fluidization of granular soils (Alsaydalani & Clayton, 2014). Our model reproduced the same geometry and conditions as the analog experiments, indicating that our implementation of MFIX-DEM is recovering the quasi-static, viscoplastic, dense phase behavior. In this regime, crystal collisions are unimportant and are primarily frictional. Instead, sustained contact forces produce stress chains and the formation of bounding faults that create the mixing bowl. The formation of these bounding faults is followed by the Reynolds' dilatancy leading to the initiation of fluidization. Our simulations capture this process, in accord with experimental results (Alsaydalani & Clayton, 2014).

After the initial quasi-static response that forms the mixing bowl, four time scales compete to control the subsequent fluidization: one associated with the shearing from the momentum flux, one associated with the relaxation time of the crystal-crystal contacts, one associated with the steady forcing of gravity, and one associated with the dissipation from liquid viscosity. For the values of the Viscous number from our simulations, which is never greater than unity, the fluidized portion of the system is always in a quasi-Newtonian regime. Direct validation for this regime is difficult to obtain as no existing experiments satisfied all the scaling requirements for verisimilitude. Alternatively, we invoke a previous MFIX validation exercise (Li *et al.*, 2012) of a bubbling fluidized bed as a proxy validation for our fluidized regime, as it has body forces and non-steady behavior. However it is in a more fluidized dynamic regime where the Viscous number is greater, and so the dissipation mechanisms are not going to be weighted the same as

they are in our simulations. Nonetheless, that validation exercise, which may in fact be a more challenging validation test example than ours, produced excellent agreement with experiments. In summary, our implementation of MFIX code meets validation as far as can be determined from the existing analog experiments.

## Chapter 3. TIME SCALES OF CRYSTAL MIXING IN MAGMA MUSHES

*Originally published in the journal Geophysical Research Letters*

Co-authored by Jillian M. Schleicher, George W. Bergantz, Robert E. Breidenthal, Alain Burgisser

### 3.1 INTRODUCTION

The compositional diversity and eruptive behavior of volcanic systems are often attributed to magma mixing. An obstacle to understanding the mixing processes is that the crystal cargo is complex, as expressed by crystal textures and chemical zoning (Charlier *et al.*, 2007; Davidson *et al.*, 2005, 2007; Ginibre *et al.*, 2007; Martin *et al.*, 2010; Wallace & Bergantz, 2005). This complexity arises from crystal and melt transfer during repeated open-system reintrusion events (Kahl *et al.*, 2011; Perugini & Poli, 2012; Ruprecht *et al.*, 2012), the remobilization of cumulates (Klemetti & Clyne, 2014; Passmore *et al.*, 2012), and the mechanical entrainment of antecrysts from the magma chamber walls and floor (Davidson *et al.*, 2007). Because of this complexity, identifying the time scales over which crystal-rich magmas transition from one spatial distribution and thermodynamic state to another by mixing has been elusive.

Numerous schemes have been employed to quantify mixing in magmas and the Earth's mantle. Mixing has often been described in terms of the evolution of Eulerian scalar field variables, as implemented in continuum numerical simulations, often including passive tracers (Oldenburg *et al.*, 1989; Tackley & King, 2003; van Keken & Zhong, 1999), analog laboratory experiments (Jellinek *et al.*, 1999; Laumonier *et al.*, 2014; Sato & Sato, 2009; Turner & Campbell, 1986), or a mixture of dynamic and kinematic elements in a reduced system amenable to chaotic analysis (Lyapunov exponents, chaotic advection, and twist maps) (Bergantz, 2000; Coltice & Schmalzl,

2006; Farnetani & Samuel, 2003; Ferrachat & Ricard, 1998; Kellogg & Turcotte, 1990; Perugini *et al.*, 2012). However, it is an open question if these methods can be applied to multiphase systems such as crystal-rich, non-Brownian multiphase mixtures, as they can exhibit nonaffine deformation and nonlocal rheology (Bouzid *et al.*, 2013; Lemaître *et al.*, 2009).

The mixing, or dispersion, of granular mixtures differs from that of pure fluids. (In this study we use the terms crystals and particles interchangeably.) The distribution of non-Brownian particles in a multiphase mixing system reflects the competition between flow-induced advection and particle segregation, the latter a process without parallel in single-phase fluids. Processes intended to produce multiphase mixing may instead cause the granular fraction to separate or unmix because of particle properties such as density or size; in non-Brownian systems this produces metastable, nonuniform particle distributions. Even in dilute, low-Reynolds number flow, particles can migrate across streamlines (Guazzelli & Morris, 2012), and particles of low ( $\ll 1$ ) but different Stokes numbers can be locally separated (Bec *et al.*, 2005). In dense viscous suspensions, lubrication forces can make it difficult to initiate the phase-relative motion required to mix a suspension (Mutabaruka *et al.*, 2014). Hence, there is no a priori reason to expect that the mixing of crystals, being of finite size and mass, can be modeled as tracers, nor that simply quantifying the global strain rate within the mixing domain provides a reliable metric of particle trajectory and hence the progress of crystal mixing.

### 3.2 A MIXING PARADIGM FOR CRYSTAL-RICH MAGMA MUSHES

The most significant difficulty in understanding crystal-rich magma mixing is the absence of real-time observational constraints on the volumes and mechanisms involved. However, recent two-dimensional numerical modeling of open-system events in crystal-rich magma mushes using discrete element method-computational fluid dynamics modeling (DEM-CFD) provides a

template for quantifying mixing, and we employ that template here to further quantify crystal-rich mixing (Bergantz *et al.*, 2015). The DEM-CFD method explicitly considers frictional, collisional, translational, buoyant, lubrication, and viscous particle-particle-fluid coupling at the crystal scale, and the mechanical coupling between the resident and intruding liquids and the crystal mush.

Specifically, (Bergantz *et al.*, 2015) demonstrated that at the start of a reintrusion event, a crystal mush at random close packing can respond initially as a viscoplastic material when intruded from below by a pure melt. The propagation of granular-fluid stresses associated with a new intrusion creates localized conjugate failure modes or soft faults, and these delimit a fluidized region called the mixing bowl. Figure 3.1a shows the essential features of the mixing bowl, which approximates the maximum available volume of the crystal pile available for mixing. Following the initial viscoplastic response, portions of the mixing bowl can become fluidized and participate in time-dependent overturn and mixing as shown in Figure 3.1b and in the supplemental Movie 2.1.

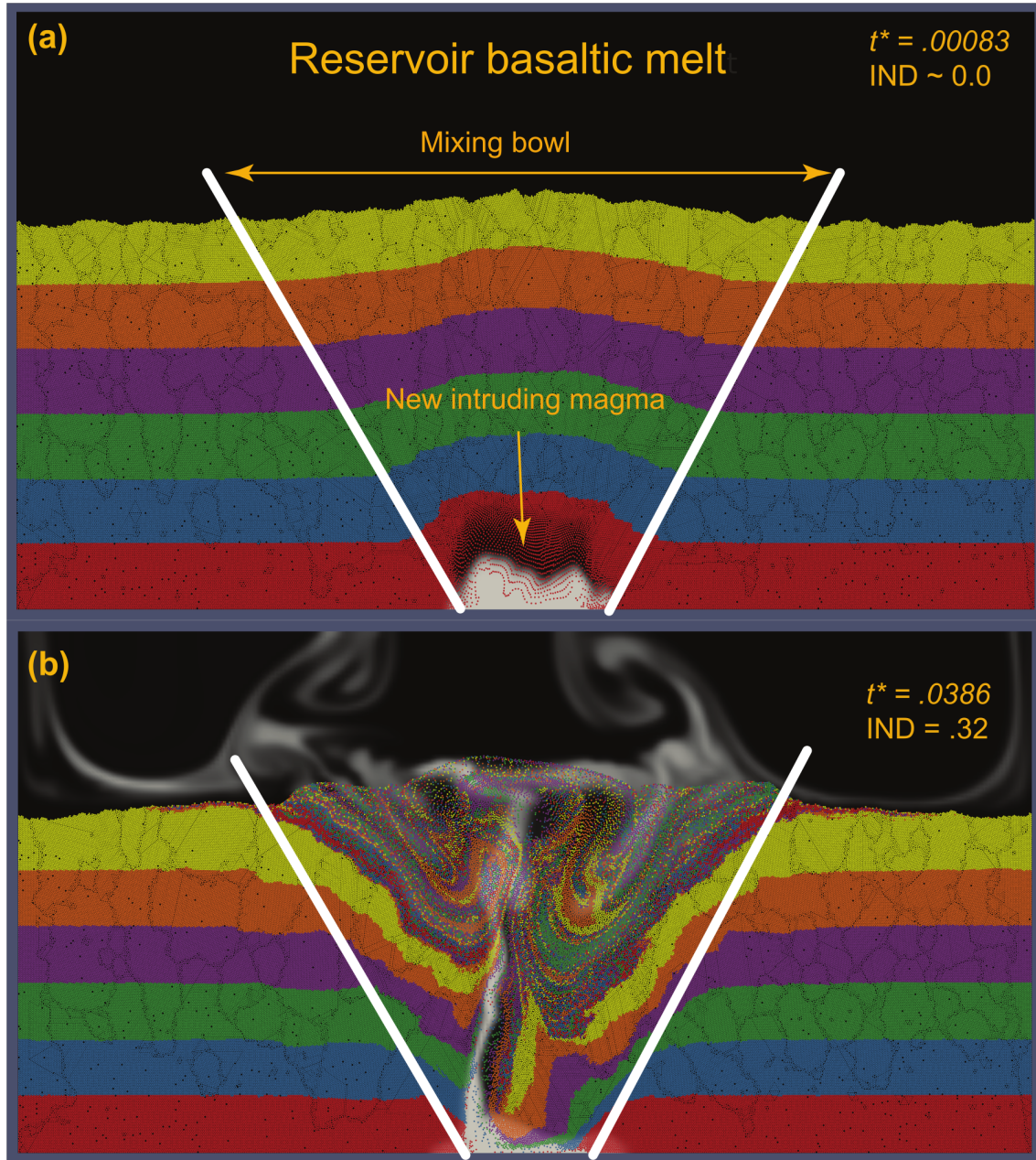


Figure 3.1. Two time steps taken from the simulation of an open-system event in basaltic mush. (a) An olivine mush with about 40% porosity is shown in side view. Resident basaltic liquid is colored black, and new magma, colored white, intrudes from below. The interplay between pore pressure and crystal contact properties induces a viscoplastic response that creates a mixing bowl and (b) causes overturn, subsequently mixing crystals and melts.

For crystal mixing to occur within a crystal-rich mush, intruding melt must fluidize settled crystals by locally decreasing their packing. At a minimum, this requires that the intruding melt enters the crystal mush at a sufficient rate to overcome the weight of the crystals in the bed. This

rate is known as the minimum fluidization velocity,  $U_{mf}$ . The  $U_{mf}$  of a system is typically calculated using the Ergun equation (Equation 3.1), with the condition that the drag force on the particles from the injected fluid equals the weight of the bed (Equation 3.4):

$$\frac{-\Delta P}{H_0} = \alpha U_0 + \beta U_0^2 \quad (3.1)$$

$$\alpha = 150 \frac{(1 - \varepsilon_f)^2}{\varepsilon_f^2} \frac{\mu_f}{d_p^2} \quad (3.2)$$

$$\beta = 1.75 \frac{(1 - \varepsilon_f) \rho_f}{\varepsilon_f^3} \frac{1}{d_p} \quad (3.3)$$

$$(1 - \varepsilon_f)(\rho_p - \rho_f)g = \alpha U_{mf} + \beta U_{mf}^2 \quad (3.4)$$

Here  $\Delta P$  is the fluid pressure drop across a particle bed of height  $H_0$ ,  $U_0$  is the superficial velocity entering the base of the system,  $\varepsilon_f$  is the fluid fraction (porosity),  $\mu_f$  is the dynamic viscosity of the fluid,  $\rho_f$  is the fluid density,  $d_p$  is the particle diameter,  $\rho_p$  is the particle density, and  $g$  is the magnitude of gravitational acceleration. This calculation only considers the pressure drop across the bed in a mixture of particles and fluid and does not consider the effect of granular forces such as contact friction or geometrical jamming that will impact the true minimum velocity for fluidization.

Following Bergantz *et al.*, (2015), new melt intrudes only a portion of the base of the lateral extent of the mush in our simulations. The mixing bowl (Figure 3.1) is tapered and opens upward; therefore, the Ergun equation must be modified. The modified calculation of  $U_{mf}$  accounts for the small injection region relative to the domain size (Cui *et al.*, 2014):

$$\frac{1}{2}\theta\beta I_w^2 \ln\left(\frac{2H_0}{I_w}\right)U_{mf}^2 + \theta\alpha I_w\left(H_0 - \frac{I_w}{2}\right)U_{mf} = (I_w + H_0 \tan\theta)H_0(\rho_p - \rho_f)g(1 - \varepsilon_f) \quad (3.5)$$

where  $\theta$  is the angle from the vertical at the edges of the fluidized region (mixing bowl) and  $I_w$  is the width of the intrusion inlet. This modified equation defines a dimensionless velocity,  $U^* = U_0/U_{mf}$ , for the system. In the case that  $U^* < 1$ , melt enters the domain at a rate lower than  $U_{mf}$ , moving through the mush as porous flow. When  $U^* > 1$ , the melt enters at a rate exceeding  $U_{mf}$  and fluidizes the crystals, as is the case in the presented simulations.

### 3.3 CALCULATING OPEN-SYSTEM MIXING IN CRYSTAL MUSH

#### 3.3.1 *Quantifying the mixing of discrete phases*

The quantification of particle mixing has obvious industrial applications, and at least 40 different schemes have been proposed to quantify the mixing of solid particles (Poux *et al.*, 1991). In almost all cases, a single metric was sought that gives a measure of the goodness of mixing throughout the entire active region. The requirements for a general index of mixing should (Doucet *et al.*, 2008): (1) satisfy sample size, frame invariance, and ergodicity requirements; (2) have a connection to the spatial coordinates to identify the major and minor directions of the progress of mixing; (3) have grid independence; and (4) resolve both weak and strong mixing. Weak mixing or “color mixing” is defined as a process where there is a progressive loss of the spatial correlation of the mixing constituents from an initial distribution as mechanically neutral, colored particles. Strong mixing refers to the additional loss of spatial correlation of properties usually leading to segregation such as size, density, or shape. It follows that any system mixed in the strong sense is also mixed in the weak sense.



### 3.3.2 The initial neighbor distance mixing index

To quantify the progress of crystal mixing in a magma mush, we employ the initial neighbor distance (IND) mixing index (Deen *et al.*, 2010). The IND varies from an initial condition value of zero, to a maximum of unity, which is the random, well-mixed state. The IND satisfies the requirements listed in Section 3.3.1 above and, unlike the Lacey Index of mixing used by Bergantz *et al.*, (2015), does not depend on grid size. In our application of the IND, the requirement of ergodicity is automatically satisfied because we evaluate all the particles that are available to be mixed (Figure 3.2).

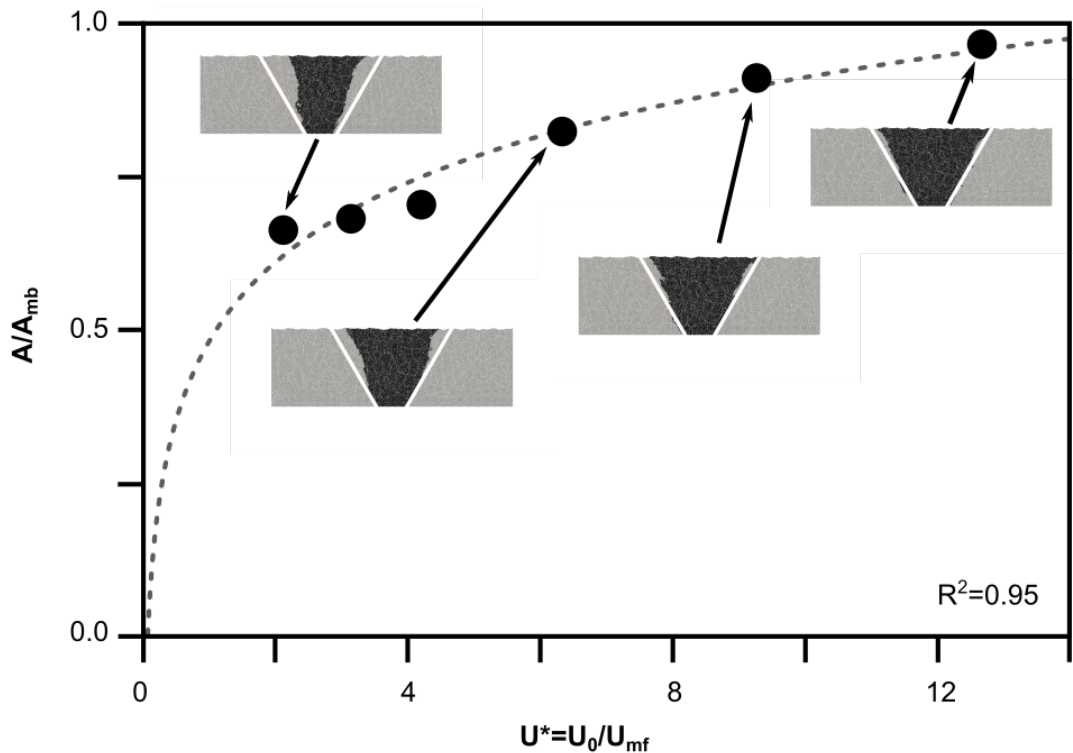


Figure 3.2. The volume (area, for our 2-D simulations) of magma that is mobilized by the intruding crystal-free magma depends on the mass flux of the intrusion. Data points represent the area fraction of mobilized crystals,  $A$ , to mixing bowl crystals,  $A_{mb}$ , and are fit with a logarithmic function (dashed line). A logarithmic fit is used to give an area fraction of zero as the mass flux goes to zero. Inset images display the mobilized crystals for four  $U^*$  values. Grey regions are stationary crystals, black regions are mobilized crystals, and white lines delimit the mixing bowl with  $60^\circ$  angles from the horizontal on either side of the intrusion.

The IND mixing index is obtained by recording the distances between initially neighboring particles at the start of mixing and summing them at every subsequent time step as the particles are dispersed. This is done for all initially active particles in the mixing domain. Because the kinematics of fluidized magma mushes can be complex, particles move apart and together, which produces noise in the initial neighbor distance time series. To reduce this noise, a second time series is created consisting of the distance between each particle and a random particle. The final IND is created from the ratio of the summed initial neighbor distances:

$$IND = \frac{\sum_{N_{part}} r_{ij} - d_p}{\sum_{N_{part}} r_{ik} - d_p} \quad (3.6)$$

Here  $N_{part}$  is the number of particles involved in the mixing calculation (see Figure 3.2),  $r_{ij}$  is the distance between particle  $i$  and its initial nearest neighbor particle  $j$ , and  $r_{ik}$  is the distance between particle  $i$  and its random, initially paired particle  $k$ .

### 3.4 CHARACTERISTIC CRYSTAL MIXING TIME CALCULATION

#### 3.4.1 *Dimensionless time scale and mixing time calculation*

The choice of a characteristic time scale for dense suspension mixing is not obvious because it is controlled by a large number of degrees of freedom reflecting both fluid and granular modes of mechanical coupling and dissipation (Marzougui *et al.*, 2015; Ness & Sun, 2015). To first order, mixing in our simulations results from vertical transport in the central chimney and large-scale overturns within the fluidized region. The proposed scaling properties treat the suspension as a single-phase mixture, the Reynolds number ( $Re$ ) of which is:

$$Re = \frac{\rho_{mix} U_0 \sqrt{A} / 2}{\mu_{mix}} \quad (3.7)$$

where  $\rho_{mix}$  is the mixture density ( $\rho_{mix} = \varepsilon_f \rho_f + (1 - \varepsilon_f) \rho_p$ ),  $U_0$  is the fluid velocity entering through the inlet (dike), and  $A$  is the area of active fluid and particles defined below. The mixture viscosity,  $\mu_{mix}$ , is calculated using the relative viscosity:  $\mu_{mix} = \mu_f \mu_{rel}$ . We use the relationship proposed by Stickel & Powell (2005):

$$\mu_{rel} = \left( 1 - \frac{1 - \varepsilon_f}{\varepsilon_{p,max}} \right)^{-2.5 \varepsilon_{p,max}} \quad (3.8)$$

where  $\varepsilon_{p,max}$  is the maximum packing fraction of particles, here chosen as 0.65. We also note that evaluating  $Re$  at the inlet instead of in the mixing bowl decreases it by a factor of 2.

In single-phase flows, viscous forces prevail when  $Re < 1$ . The vorticity of large-scale vortices decays by direct viscous stresses over the entire active area. The time scale for mixing is proportional to the rotation time of these large-scale vortices. Their size is constrained by the mixing bowl, they are driven by the thrust coming from the inlet, and the bulk viscosity opposes resistance to their rotation. Dimensional arguments similar to those used by Breidenthal *et al.*, (1990) yield the following characteristic time scale for the viscous regime:

$$t_{mix-v} = \frac{\sqrt{A}}{U_0} \mu_{rel} \quad (3.9)$$

This time scale can be thought of as the travel time across the active area ( $A$ ) multiplied by the bulk viscosity contrast of the resident and injected magmas.

This viscous time scale is ultimately determined only by the thrust at the inlet and the active area of fluid and particles. The logarithmic relationship between area and  $U^*$  (and hence,  $U_0$ , for systems with the same  $U_{mf}$ ) discussed below, means that  $U_0$  controls  $t_{mix-v}$ : higher values of  $U_0$

result in lower  $t_{mix-v}$ . The four presented simulations start with the same initial bed packing and fluid viscosity, so the relative viscosity term is constant. Therefore, a second viscous mixing timescale removes the  $\mu_{rel}$  term from Equation 3.9, and includes only the ratio of the square root of the area and the intrusion velocity.

In single-phase flows with  $Re > 1$ , mixing can be simply ascribed to just two scales, the Taylor and the Batchelor layers (Broadwell & Breidenthal, 1982; Broadwell & Mungal, 1991; Dimotakis, 2005). These are the diffusive spatial scales associated with the largest and the smallest eddies in the flow. As  $Re$  increases, the sizes of the largest and smallest eddies, as well as their diffusive scales, spread further apart. At a  $Re$  of order  $O(10^3)$  in a single-phase system, there is an increase in molecular-scale mixing at the mixing transition. The characteristic time scale for mixing in the inertial regime is given as (Breidenthal *et al.*, 1990):

$$t_{mix-i} = \sqrt{\frac{A^{3/2} \rho_{mix}}{\rho_f U_0^2 I_w}} \quad (3.10)$$

The characteristic mixing time can be thought of as the ratio of the mass of material in the active area to the injection thrust.

Below the mixing transition, the flow is not self-similar and there is no well-defined size for the small-scale vortices, so there is essentially no Batchelor layer. Large-scale motions control mixing in a single- and condensed-phase system and particle dispersion in a two-phase system. Non-Brownian particle dispersion differs from the mixing of a scalar field variable in that it does not depend on a progressive reduction in scale by repeated stretching. Hence, global strain rate may not provide a reliable proxy for the progress of dispersion and multiphase mixing. As a result, mixing and dispersion below the mixing transition do not depend on  $Re$ .

While  $Re$  characterizes the dynamics of the motions within the active area, the ratio  $t_{mix-i}/t_{mix-v}$  characterizes the respective effectiveness of inertial and viscous forces in advancing the actual mixing process by large-scale vortices.  $Re$  of our simulations straddle unity and  $t_{mix-i}/t_{mix-v}$  is well below unity. This suggests that while  $t_{mix-v}$  is the most appropriate choice in our runs to calculate the dimensionless times as  $t^* = t/t_{mix-v}$ , the role of inertial forces cannot be neglected. This is reflected by the fact that using  $t_{mix-i}$  instead of  $t_{mix-v}$  to calculate  $t^*$  collapses the data equally well. The second viscous time scale,  $t_{mix-v}$  without the viscosity ratio, also collapses the data. The range of  $t^*$  values for this alternative viscous time scale for falls between 0 and  $\sim 10$ , indicating this may be a more appropriate time scaling.

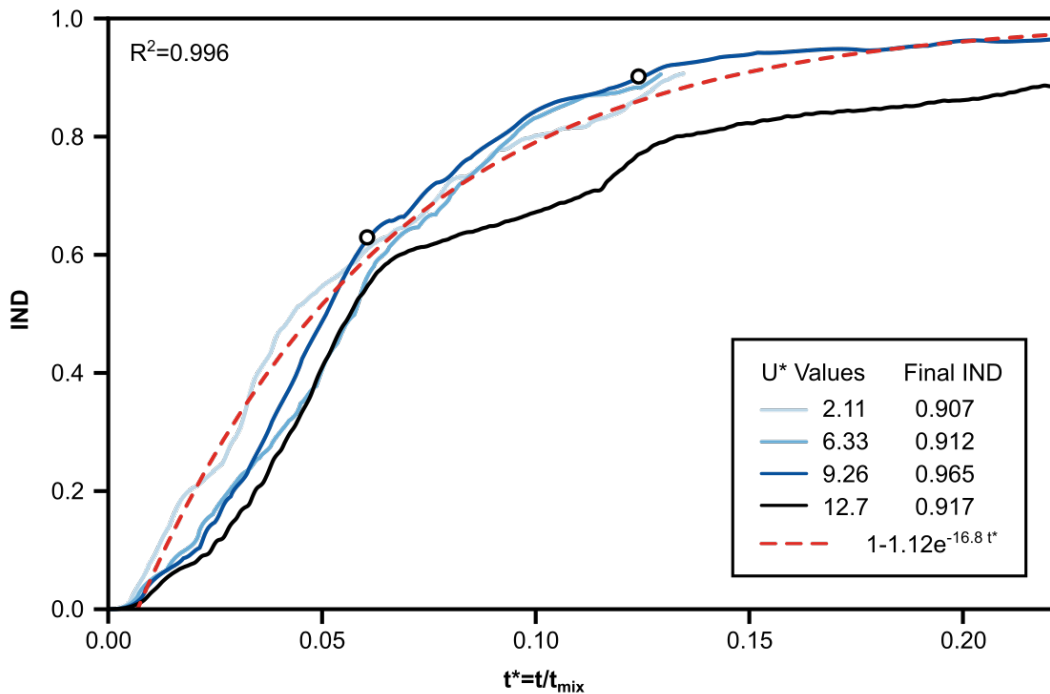


Figure 3.3. The initial neighbor distance (IND) as a function of dimensionless time ( $t^*$ ) for four intrusion rates. Time is nondimensionalized by the characteristic mixing time given in Equation 3.9. An exponential curve (red dashed line) is fit to the IND curves for three  $U^*$  intrusion rates. The black curve is not included in the fit; see text for discussion. White circles with black outlines display the times and IND values used in Figure 3.4.

The four simulations shown in Figure 3.3 have  $Re$  varying from approximately 0.5 to 5. This variation is associated with the progressive onset of pulsing and active bifurcation of the central chimney (Figure 3.1b). Pulsing is created by the interplay between the collapse of one margin of the mixing bowl into the base of the fluidized core, followed by the subsequent buildup of pressure from continuously supplied new melt that is then released as a pulse that rises in the central chimney. This pulse undergoes internal circulation and induces small-scale granular vortices described in previous simulations (Bergantz *et al.*, 2015). However, the appearance of these new, smaller scales of overturn and fluid motion do not seem to produce significant additional crystal separation. It follows that the particle dispersion is essentially independent of  $Re$  and of  $t_{mix-i}/t_{mix-v}$ , for all  $U^* > 1$  given that the range of these two dimensionless quantities in magmatic applications are unlikely to exceed  $O(10^2)$  and  $O(1)$ , respectively. In summary, Equation 3.9 works because the primary contributions to the increasing value of the IND are vertical transport in the chimney, lateral transport at the mush-reservoir interface, and large-scale circulation in the mixing bowl, which are the dominant mechanisms of dispersion. Simply indexing the crystal mixing to the strain history may misrepresent the time scales of crystal separation.

Some care is required to estimate the area term,  $A$ . Although the mixing bowl (Figure 3.1) approximates the spatial scale of the initial plastic response of the mush, the entire mixing bowl may not be subsequently fluidized. Hence, the area term must be adjusted to reflect the portion of the mixing bowl that is active or unlocked. Figure 3.2 provides an empirical estimate of the active area as a function of the input velocity and the bed characteristics

$$\frac{A}{A_{mb}} = 0.187 \ln(U^*) + 0.481 \quad (3.11)$$

The logarithmic relationship chosen for  $A/A_{mb}$  and  $U^*$  recovers the requirement that the active area of particles approaches zero as the input velocity decreases to zero.

We performed four numerical experiments at different values of  $U^*$  and calculated the characteristic mixing response using the IND method. All experiments used the same geometry and boundary conditions as shown in Figure 3.1 but with different values of the input mass flux. The results are shown in Figure 3.3 where the IND as a function of scaled time is shown. Although the experiments were not terminated at the same value of the IND, they all show an exponential approach to mixing; the three experiments with the lowest  $U^*$  exhibiting a statistically significant collapse to a common exponential relationship (Figure 3.3). The black curve, for a  $U^*$  of 12.7, was not included in the exponential relationship as it shows a distinctly different trajectory. Despite having a greater input velocity and hence thrust, the  $U^* = 12.7$  experiment shows a delayed mixing time scale compared to the others. Examination of the simulation reveals that the  $U^* = 12.7$  is so vigorous that some particles in the active region are carried completely out of the mixing bowl, where they are deposited and so removed from any further mixing, yet are still included in the IND calculation. While this process contributes to the global redistribution of crystals, it produces an apparent delay in the progress of mixing as defined by the IND metric.

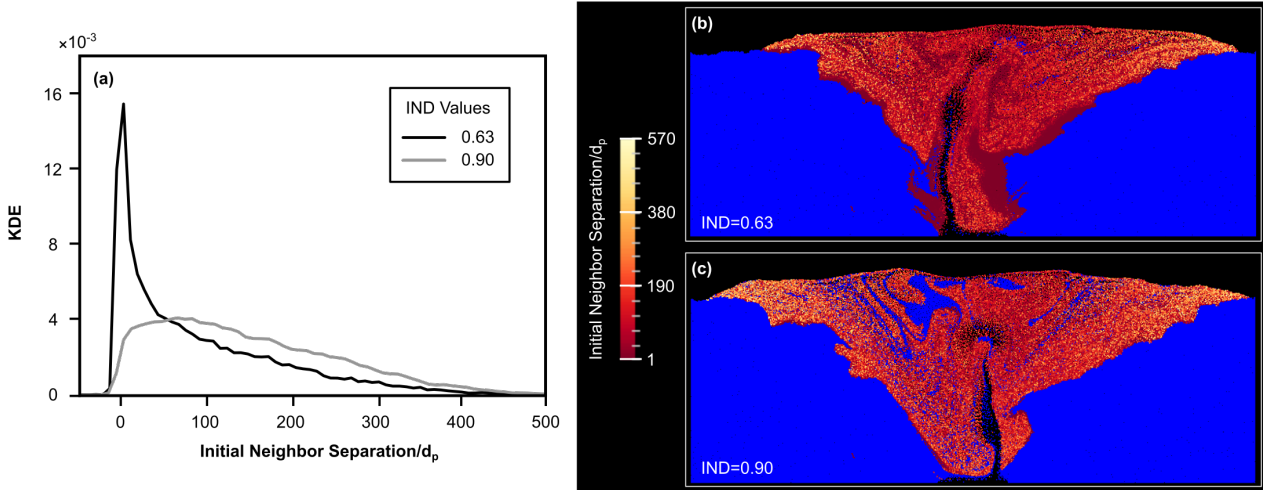


Figure 3.4. (a) The Kernel density estimation (KDE) of the distribution of distances between crystals and their initial neighbors for the  $U^* = 9.26$  intrusion for IND equal to 0.63 and 0.9. The KDE of the distances at the initial time (IND = 0) has a peak around 1, as many crystals are within one crystal diameter of their initial neighbor. Continued intrusion disperses the crystals, lowering the peak, and extending the tail of the curve to greater particle separation and hence degree of mixing. (b) Initial neighbor distances of particles considered for the IND calculation at an IND of 0.63. (c) Initial neighbor distances of these same particles at an IND of 0.90. Blue regions within the mixing bowl in (b) and (c) are crystals entrained from the walls, and not included in the IND calculation.

While the IND provides a single measure for the goodness of mixing of active particles within the entire domain, there will be a distribution around this value, with some portions better mixed than others. We illustrate this in Figure 3.4a, which is the kernel density estimation, KDE, of the particle pair distances at two points in time. The KDE was constructed using the adaptive kernel density estimator, based on linear diffusion as proposed by Botev *et al.*, (2010), which avoids uncertainties associated with KDE bandwidth selection (Rudge, 2008; Vermeesch, 2012). Two curves are shown for the simulation with  $U^* = 9.26$  representing IND values of 0.63 and 0.90, which are also shown as small circles in Figure 3.3. Figure 3.4b and 3.4c illustrate how the particle spacing distribution changes as a function of the IND, with a noticeable change going from an IND of 0.63 to 0.90. The KDE and particle spacing distribution for IND equal to 0.63 (Figure 3.4a and 3.4b) show that a significant number of particles are still in close proximity to



their initial neighbor. A practical implication of this is that it would take numerous geological samples to adequately characterize the diversity of mixing conditions that coexisted during the open-system event. When the IND equals 0.9, Figure 3.4a and 3.4c show that the distance between initial particle pairs is distributed more uniformly and is much greater. Nonetheless, even at an IND of 0.9, some elements of the system remain relatively unmixed.

### 3.4.2 *Applications to natural systems*

Here we exemplify the application of the IND framework to a natural example at two values of the input mass flux. Consider a 500 m thick crystal mush, composed of basaltic melt and olivine crystals, as might be found in an ocean island, mid-ocean ridge or a composite system like Iceland. We use a melt viscosity and density of 2 Pa s and 2650 kg/m<sup>3</sup>, respectively. The crystal density is 3300 kg/m<sup>3</sup> and diameters are 0.002 m, creating an overall mush porosity of 0.4. If a crystal-free basaltic intrusion enters the mush from a meter-wide dike, the minimum fluidization velocity of the system is 0.005 m/s. Using the relationships described above, an intrusion entering at  $U^* = 9.26$  would fluidize a volume of  $\sim 130,000$  m<sup>3</sup> per meter of dike length normal to the mixing bowl span. The crystals in the active area would achieve an IND mixing value of 0.9 after 20 h of sustained intrusion, based on the viscous time scale given in Equation 3.9. If the inertial time scale is used, it increases this duration by a factor of 8. The amount of new melt that would have come into the system is  $\sim 3400$  m<sup>3</sup>, which is  $\sim 2.6\%$  of the volume activated by the intrusion. This is a mass flux rate of approximately 0.0015 km<sup>3</sup>/yr, roughly two orders of magnitude lower than the long-term rate calculated for the Kilauea system (Poland *et al.*, 2012) and about one order of magnitude lower than that estimated for the Hekla volcano in south Iceland (Geirsson *et al.*, 2012). If the input dike length is greater, the corresponding input

velocity will be lower to match the same mass flux, and the  $U^* = 2.11$  may provide a better estimate of the input velocity and fluidization potential. Under these conditions it will take approximately 73 h of continuous magma input to reach an IND of 0.9. For these same conditions, the viscous time scaling without the viscosity ratio gives IND = 0.9 mixing times of approximately 13 h and 2 days for  $U^* = 9.26$  and  $U^* = 2.11$ , respectively. Given the geophysically constrained estimates of mass flux into basaltic systems, we conclude that the active crystal cargo of a natural basaltic crystal mush will likely be well mixed during reintrusion events on a time scale of days to tens of days (Costa *et al.*, 2010; Kahl *et al.*, 2015).

### 3.5 SUMMARY AND CONCLUSIONS

Crystal mixing in basaltic magma mushes was quantified by introduction of the initial neighbor distance (IND) method. The IND method satisfies many of the criteria for a robust metric of mixing and provides a global measure of the loss of spatial correlation from an initial distribution of crystals in the crystal-rich mush. The IND was applied to a model open-system reintrusion event in a basaltic magma chamber, and two characteristic mixing time scales were introduced that allow for the estimation of the time to mixing under a variety of geologically relevant conditions. A kernel distribution estimation was employed to illustrate the distribution of local crystal segregation scales around the global IND value. Application to natural basaltic systems reveals that mixing of a basaltic crystal mush can occur within days with geologically inferred magma intrusion rates.

## Chapter 4. MUSH MOBILIZATION AND MIXING IN THE 1868 ERUPTION OF MAUNA LOA, HAWAII

### 4.1 INTRODUCTION

#### 4.1.1 *Crystal populations*

Magmatic systems typically contain diverse populations of crystals formed and brought together by processes such as intrusion, disaggregation of cumulates, mixing, and assimilation of previously crystallized material (Cooper *et al.*, 2016; Kahl *et al.*, 2011; Moore *et al.*, 2014; Viccaro *et al.*, 2016). Each population of crystals reflects the chemical, mechanical, and thermodynamic conditions of their growth and residence within a magmatic system (Jerram & Martin, 2008; Streck, 2008), and distinguishing the conditions that formed the populations helps to infer how magma moves through the crustal magmatic system (Gaffney, 2002; Kahl *et al.*, 2011). Plutons integrate tens of thousands to millions of years of storage (Barboni & Schoene, 2014; Cooper, 2015; Cooper & Kent, 2014) that are punctuated by magmatic processes occurring on timescales as short as days to months (Barboni & Schoene, 2014; Cooper *et al.*, 2016; Cooper & Kent, 2014; Kahl *et al.*, 2011; Moore *et al.*, 2014). The large timescales involved in pluton assembly can hinder the identification of individual processes that generate populations of crystals, though magmatic structures which form during late-stage mixing and intrusion events can be preserved (Paterson, 2009). Volcanic eruptions sample the near-instantaneous state of a magma reservoir, and erupted crystals contain records of magmatic processes from a range of timescales. Crystal growth, dissolution, and diffusion can record (or erase) the sequence of magmatic processes that occurred throughout the existence of the crystal (Cooper, 2015; Costa *et*

*al.*, 2010; Kahl *et al.*, 2011; Moore *et al.*, 2014; Ruprecht *et al.*, 2008). The remainder of this study will focus on volcanic products and their record of magmatic processes.

Crystal populations are defined by a combination of textural characteristics and crystal compositions which provide insight into the origin and history of the populations (Jerram & Martin, 2008; Streck, 2008). Textural characteristics of crystals include the size distribution of crystals (Jerram & Martin, 2008; Marsh, 1988, 1998) and the morphology of crystals (e.g. resorption features, skeletal crystals, kink banding, clustering) (Helz, 1987; Jerram *et al.*, 2003; Welsch *et al.*, 2013). Compositional populations include the mineralogy in the samples (e.g. (Neave *et al.*, 2014; Passmore *et al.*, 2012); the major, minor, trace elemental, and/or isotopic composition of crystals (Davidson *et al.*, 2007; Hansen & Grönvold, 2000; Thomson & Maclennan, 2013); the ages of crystals (Cooper, 2015; Eppich *et al.*, 2012); the compositions of melt inclusions within the crystals (Danyushevsky *et al.*, 2004; Tuohy *et al.*, 2016; Wallace *et al.*, 2015); and the type of chemical zoning (Kahl *et al.*, 2011, 2013, 2015; Lynn *et al.*, 2017; Moore *et al.*, 2014; Viccaro *et al.*, 2016; Wallace & Bergantz, 2002, 2004, 2005). These populations reflect the stages of transport and storage experienced by the crystals, and thus can be used to infer magmatic conditions and processes in the reservoir prior to eruption.

Multiple populations of crystals within a single eruption indicate that multiple magmatic environments contributed to the crystal assemblage. A magmatic environment, as in Kahl *et al.*, (2011), is defined by the thermodynamic, chemical, and mechanical conditions within a magmatic reservoir. Distinct magmatic environments can exist as physically separate reservoirs throughout the crust, or as regions within the same reservoir with thermal, chemical, and crystal-fraction variability. Identifying the conditions within magmatic environments (e.g. depth, pressure, temperature, composition) helps to infer how magma moves through the reservoir

(Gaffney, 2002; Kahl *et al.*, 2011, 2013, 2015; Tuohy *et al.*, 2016). An important caveat is that if a crystal passes through an environment or experiences a magmatic process that occurs in a timescale too short to be recorded by the crystal, no record of this event or environment will exist (Ruprecht *et al.*, 2008). Additionally, crystal dissolution can erase the record of a magmatic environment; this could be recorded as a sharp break in compositional zoning through the crystal. Previous studies by Kahl *et al.* (2011, 2013) and Viccaro *et al.* (2016) used diffusion modeling for different crystal populations to estimate timing of magma transfer through magmatic environments, and found these timescales correlated with geophysical and degassing monitoring data. These results indicate it is possible for crystals to record residence in and movement between multiple magmatic environments prior to their eruption.

We studied olivine crystals from a simple example of an erupted mush, the 1868 picrite eruption of Mauna Loa. The goals of this study are to determine whether there are distinct magmatic environments sourcing the Southwest Rift Zone (SWRZ) of Mauna Loa by identifying crystal populations in a single eruption, and to understand mobilization and mixing processes that occurred within the reservoir prior to the eruption. The focus of many previous studies of Mauna Loa lavas has been on geochemical and isotopic variation in whole-rock compositions to investigate the source of magma (e.g. Cohen *et al.* (1996); Kurz *et al.* (1995); Rhodes (1983, 2015)). Long-term, major-element homogeneity of Mauna Loa whole-rock samples has been interpreted as the result of a frequently replenished, shallow summit magma reservoir that feeds both the summit caldera and rift zones (Rhodes, 1983, 1988). However, to understand the conditions of mobilization and mixing within the rift reservoir system, it is necessary to also study samples at the crystal scale. A number of previous Mauna Loa studies, primarily from drill cores, submarine flows, and rift eruptions, looked at variation in olivine cores (Figure 4.1). The

range of core compositions for Mauna Loa olivine falls between Fo<sub>80</sub>-Fo<sub>90</sub>, and NiO concentrations between 0.3-0.6wt%. The studies that measured zoning found most olivine crystals have normally zoned rims, with only rare reversely zoned crystals (Baker *et al.*, 1996; Garcia *et al.*, 1995; Garcia, 1996). In this study we identify crystal populations from the 1868 eruption, distinguished by their composition and variety of Fo and NiO zoning.

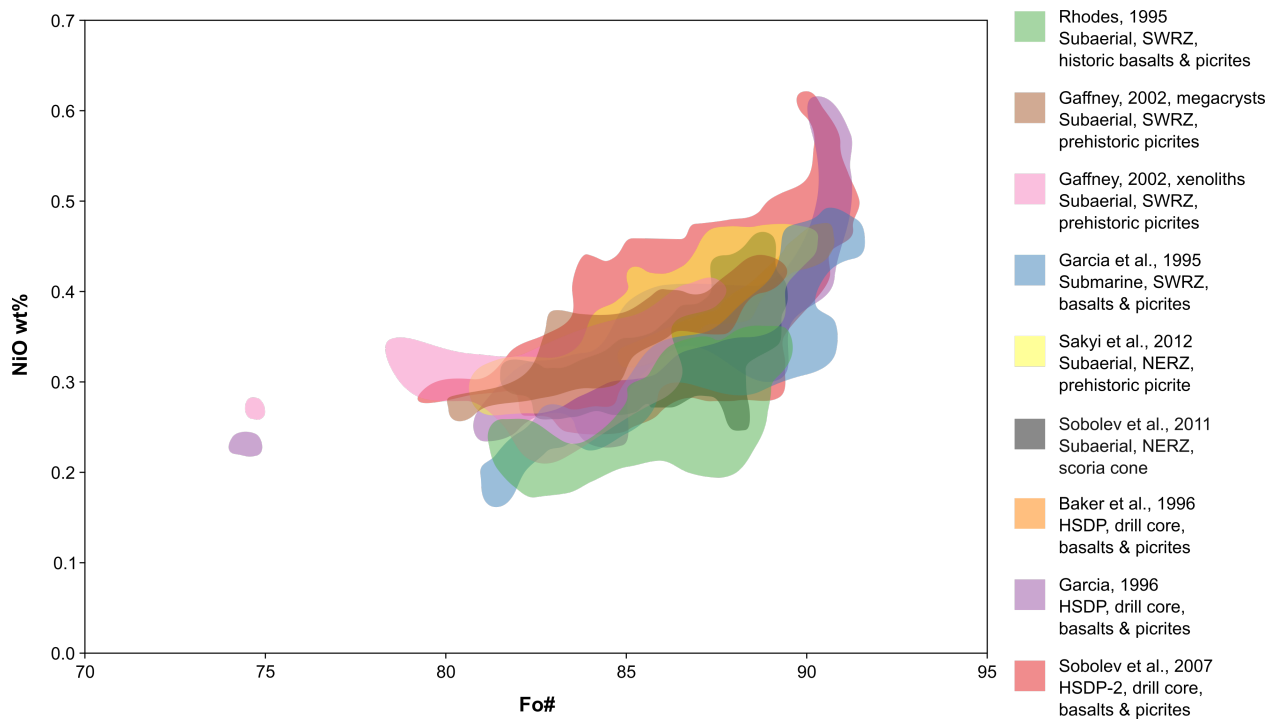


Figure 4.1. NiO-Fo plot showing ranges of previously analyzed olivine crystals from Mauna Loa. Data are from: Baker *et al.* (1996); Gaffney (2002); Garcia *et al.* (1995); Garcia (1996); Rhodes (1995); Sakyi *et al.* (2012); Sobolev *et al.* (2007, 2011).

#### 4.1.2 *Mauna Loa, Hawaii, 1868*

The Mauna Loa picrite eruption of 1868 occurred at the end of a two-week sequence of tectonic and volcanic events. Seismicity began on March 27, coinciding with a small eruption at Mokuaweoweo, the summit caldera of Mauna Loa (Hitchcock, 1911). Thousands of earthquakes occurred during the following days, culminating on April 2 with the largest earthquake in

recorded Hawaiian history, estimated at magnitude 7.9 (Figure 4.2a). The earthquake generated a tsunami that inundated the southeast coast of the island along Kilauea, and a three-mile long landslide that occurred near Wood Valley.

On April 6, pumice and ash erupted at Kahuku along the SWRZ, and on April 7, lava erupted from vents between 600-900m in elevation (Rhodes, 1995). The eruption lasted five days, with fountains of lava at the main vent (Hitchcock, 1911). The flow began as pahoehoe and traveled more than 18 km to the ocean in four hours, creating the Puu Hou littoral cones. A steep cliff bisected the flow, and accounts report the initial pahoehoe was followed by a'a moving across the pastureland to the east of the cliff (Hitchcock, 1911). In total the eruption produced 0.123 km<sup>3</sup> of lava (Lockwood & Lipman, 1987).

The 1868 picrite was an unusual eruption in Hawaiian recorded history. It occurred during a period of high-magma flux to Mauna Loa between 1843-1887 (Lockwood & Lipman, 1987), which produced primitive and picritic rift and radial vent eruptions in 1852, 1855, 1859, and 1868 (Rhodes, 1995; Rhodes & Hart, 1995; Riker *et al.*, 2009). These eruptions also had high quenching temperatures for Mauna Loa subaerial lavas, some exceeding 1200°C (Riker *et al.*, 2009). Lavas erupted during this period contained decreased incompatible element concentrations, possibly because the high magma flux prevented them from stalling in the shallow reservoirs where magma normally would cool and fractionate before eruption (Rhodes & Hart, 1995). Incompatible element concentrations gradually returned to higher levels beginning in 1899 (Tilling *et al.*, 1987), coinciding with a declining magma supply rate (Lockwood & Lipman, 1987; Rhodes & Hart, 1995). This shift in magma supply could represent the end of the period of numerous rift-zone eruptions on Mauna Loa, and indicate a return in the future to increased summit activity (Lockwood, 1995). The 1868 eruption immediately followed the

magnitude 7.9 earthquake, which was the result of slip along the décollement at 9 km depth in the crust (Wyss, 1988). It is possible that the earthquake disrupted the Mauna Loa magmatic system, draining the magma stored in the summit reservoir into the SWRZ which allowed the deeper, olivine-rich magmas to erupt (Tilling *et al.*, 1987; Walter & Amelung, 2006). However, a similar picrite erupted in 1852 from the Northeast Rift Zone, making it likely that both picrites erupted as the result of tapping into deeper, olivine-rich magmas during the period of increased magma supply (Rhodes, 1995). These unique aspects of the 1868 eruption could provide evidence for conditions within parts of the Mauna Loa reservoir system that would not normally be active during typical subaerial or rift eruptions, thus making it an ideal flow to investigate reservoir conditions and magma transport.

## 4.2 SAMPLES AND METHODS

### 4.2.1 *Sample locations*

Samples were collected from the upper parts of the flow (Figure 4.2), from deposits of both pahoehoe and a'a. Samples included lava with low (<10%) olivine contents (referred to as “basalts”), lava with high (30-40%) olivine contents (“picrites”), one tephra sample, and lavas containing xenoliths (which were not analyzed in this study).

### 4.2.2 *Modal abundances*

Olivine modal abundances for 22 samples were determined using stitched images from a petrographic microscope. Olivine crystals larger than those in the groundmass were traced in each image using the vector graphics software Inkscape. Modal abundances of olivines, vesicles, and groundmass (which included rare plagioclase and orthopyroxene crystals that were larger than the groundmass) were determined using the image processing software, ImageJ. Olivine



contents are reported as dense rock percentages, with only areas from olivine and groundmass considered.

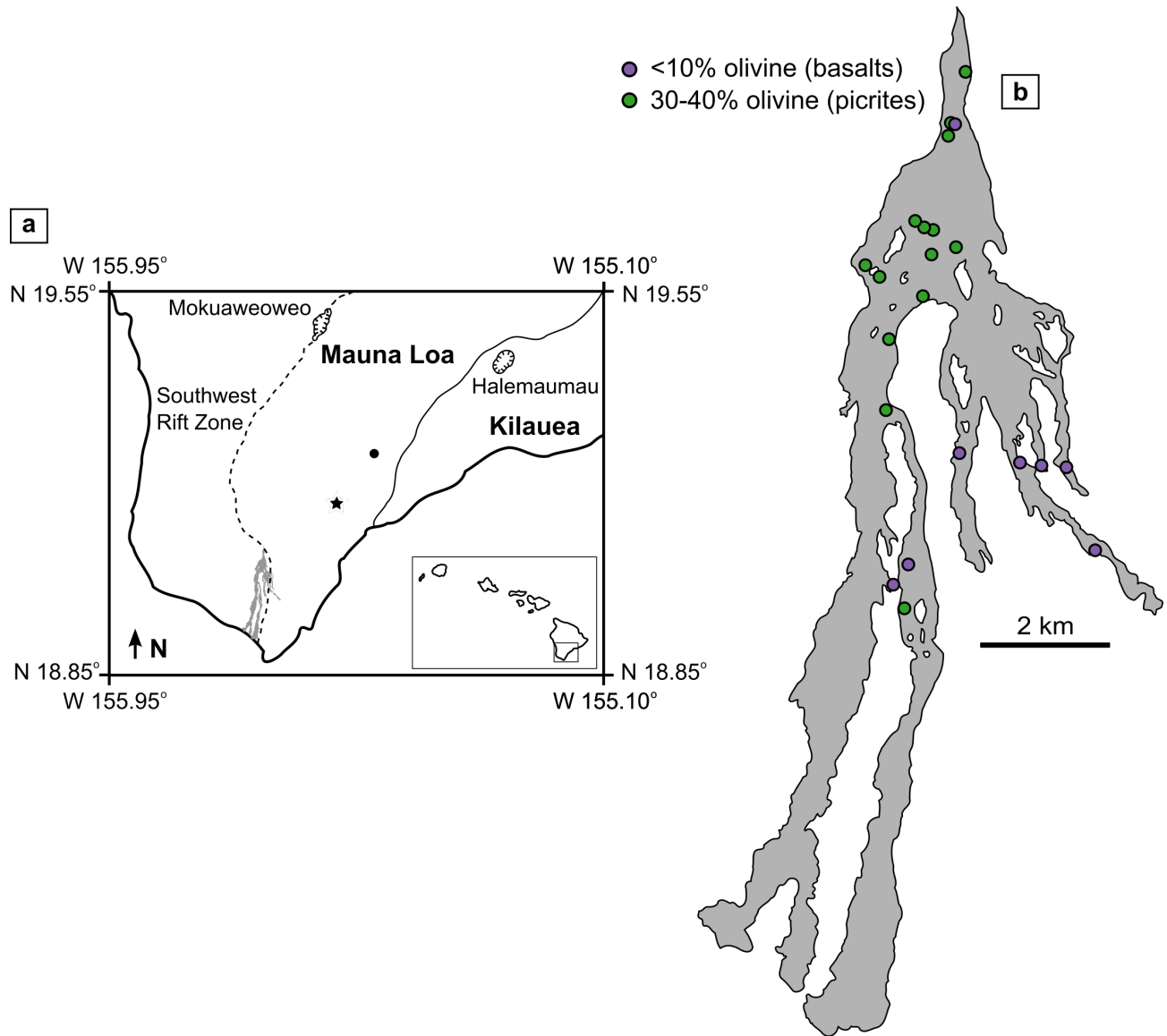


Figure 4.2. Map of the 1868 southwest rift eruption of Mauna Loa, Hawaii. a) Map includes a portion of Mauna Loa and Kilauea volcanoes and their summit calderas. Inset image shows the Hawaiian Islands, and the location of the map. The SWRZ of Mauna Loa is labeled with a dashed line, and the 1868 eruption is shown in grey. The star shows the epicenter of the magnitude 7.9 earthquake that preceded the eruption, and the circle shows the location of the landslide that resulted from the earthquake. b) The lava flow field outline with sample locations; purple dots represent samples with less than 10% olivine crystals (basalts), and green dots represent samples with 30-40% crystals (picrites).

#### 4.2.3 *X-ray Fluorescence*

Twenty-two samples were analyzed using X-ray fluorescence (XRF) at the University of Massachusetts, Amherst with a Philips PW2400 sequential spectrometer. Whole rock abundances of major and trace elements (Nb, Zr, Y, Sr, Rb, Pb, Ga, Zn, Ni, Cr, V, Ce, Ba, La) were measured using methods in (Rhodes & Vollinger, 2004).

#### 4.2.4 *Electron Microprobe*

Crystals from 12 samples were analyzed using a five spectrometer JEOL Hyperprobe JXA-8500F at the University of Hawaii. Point analyses were taken with a 20kV accelerating voltage and a 200nA beam current. Peak counting times were 60 seconds, and backgrounds were measured for 30 seconds on each side of the peaks. Analyses include Si, Mg, Ca, Ni, and Fe. Crystals were analyzed at the core and rim with point analyses, and 1-7 line scans per sample were taken. Prior to measuring the line scans, backscatter electron (BSE) images of the crystals were analyzed using ImageJ to determine preliminary zoning patterns; this avoided spending unnecessary time measuring constant compositional plateaus in the cores. The beam diameter for both the points and line scans was 2  $\mu\text{m}$ , and the line scans were taken with points spaced between 5-7  $\mu\text{m}$ . Line scans were taken perpendicular to crystal faces, and locations were chosen away from corners. BSE images were analyzed using ImageJ to avoid sloping zoning profiles due to sectioning effects (Shea *et al.*, 2015a). Repeat analyses on San Carlos and Spring Water standard olivine were measured after every two to three line scans or sets of point analyses.  $\text{SiO}_2$  and MgO analyses were corrected based on peak drifts measured from analyzing the standards, and these corrections were applied to line scan measurements taken between standards. Two-sigma precision values from repeat analyses of the San Carlos analyses are: 0.47wt% for  $\text{SiO}_2$ , 0.32wt% for MgO, 0.17wt% for FeO, 0.008wt% for NiO, and 0.009wt% for CaO. Data are

presented with error bars relating to the day in which the measurements were made, so they may appear smaller than the overall standard analyses.

### 4.3 RESULTS

#### 4.3.1 *Whole rock*

Bulk rock compositions follow an olivine-control trend for both major and trace elements (Rhodes, 1983, 1995), and fall along major element trends previously established in samples representing over ~600kyr of Mauna Loa magmatic history (Rhodes, 2015). Two varieties of samples are distinguished by their olivine content (Figure 4.3). We will refer to these as basalts, with olivine contents lower than 10% and whole rock Mg# ~60-65, and picrites, with olivine contents between 30-40% and whole rock Mg# ~77-81 (where  $Mg\# = 100 (Mg^{2+} / (Mg^{2+} + Fe^{2+}))$ ). The basalts and picrites are not spatially segregated (Figure 4.2), with the exception of low-olivine a'a lobes to the east of the cliff. This part of the flow was reported as occurring later in the four-day eruption (Hitchcock, 1911).

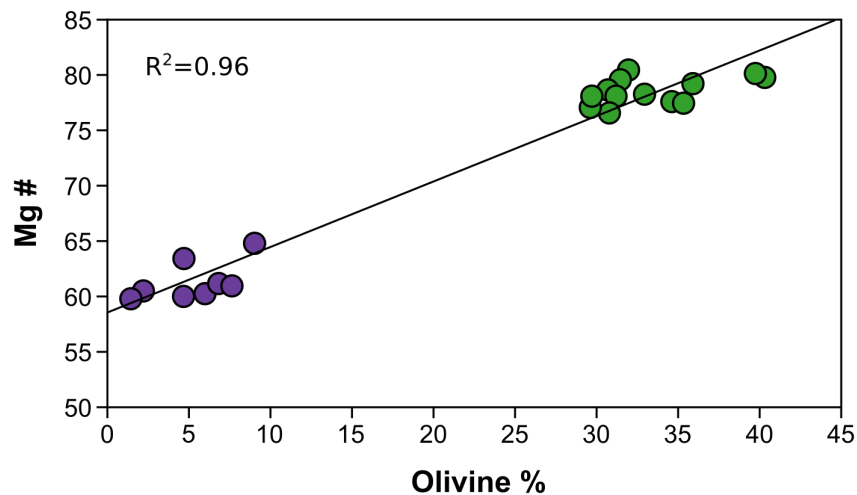


Figure 4.3. Whole rock Mg# ( $100 * (Mg^{2+} / (Mg^{2+} + Fe^{2+}))$ ) against olivine % in samples. Purple and green dots represent basalts and picrites, respectively.

Olivine crystals are subhedral to euhedral in samples of both the basalts and picrites, present as both single crystals and clusters. Crystals range from <1mm to 1cm in their longest dimension. The basalts contain plagioclase and orthopyroxene crystals that are larger than the groundmass. Additional information on these mineral phases can be found in (Rhodes, 1995).

#### 4.3.2 *Microprobe*

##### 4.3.2.1 Core and rim analyses

Of the twelve samples analyzed by microprobe, four were basalts and eight were picrites. The measured olivine core compositions fall between Fo<sub>78.2</sub>-Fo<sub>89.5</sub> (Fo# = 100 (Mg<sup>2+</sup> / (Mg<sup>2+</sup> + Fe<sup>2+</sup>))), with little distinction between core ranges for the basalts (Fo<sub>78.2</sub>-Fo<sub>89.2</sub>) and picrites (Fo<sub>80.5</sub>-Fo<sub>89.5</sub>). Both the basalt and picrite core composition distributions have peaks at ~Fo<sub>89</sub> and have similar compositions as those from previous studies (Figure 4.4). The slightly higher Fo values of the previously studied olivines could be the result of more primitive magmas sourcing submarine eruptions (Garcia *et al.*, 1995). Compared to whole rock compositions, olivine cores in the basalts tend to have values around the equilibrium field for a partition coefficient of  $K_D = 0.345 \pm 0.018$  (Matzen *et al.*, 2011), both above and below the range expected for crystals in equilibrium with the whole rock compositions (Figure 4.5). The whole-rock Mg# for the basalts and picrites fall in distinct groups, with basalt values between Mg# = 59.9-64.8, and picrite values between Mg# = 76.5-80.5. The olivine compositions that would be in equilibrium with the picrite whole rock Mg# values are higher (~Fo<sub>90</sub>-Fo<sub>92</sub>) than any crystal analyzed in this study. Instead, the picrite olivine cores have Fo values below the equilibrium field, indicating these high Mg# samples are the result of olivine accumulation.

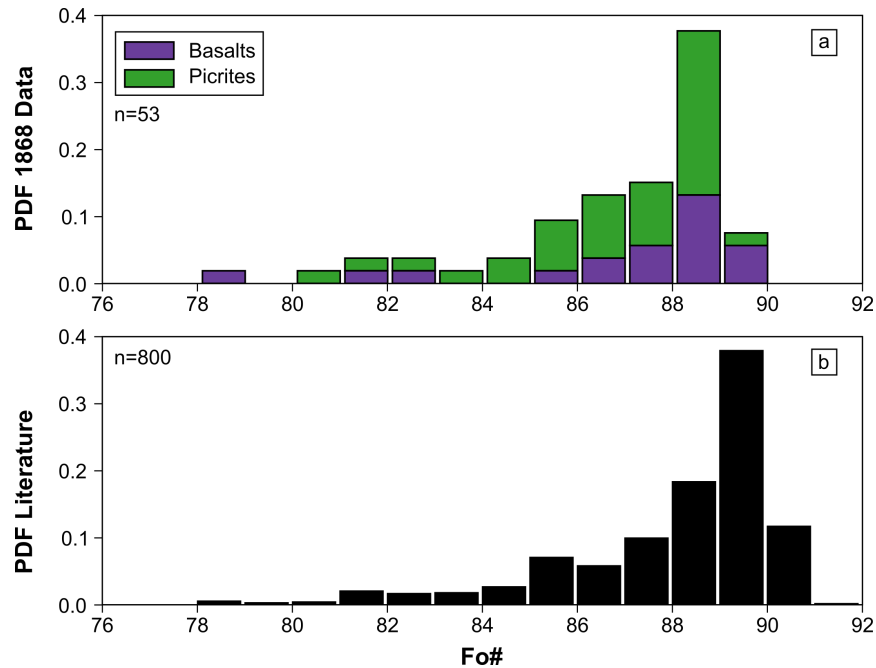


Figure 4.4. Probability distribution functions of Fo# in olivine cores. a) Olivine cores from 53 crystals from the 1868 eruption of Mauna Loa (this study). Cores are the average plateau compositions of crystals. Crystals from basalt samples are shown in purple, and those from picrites are shown in green. Bars representing picrites and basalts are stacked, not overlapping. b) Olivine core compositions from previous studies of Mauna Loa olivines; see references in Figure 4.1.

The range of olivine rim compositions is between  $Fo_{72.5}$ - $Fo_{85.2}$ . Rim values are only considered from crystals for which the final points in each line scan had acceptable totals. While we do not have glass compositional analyses, previous studies by Rhodes (1995) and Wilkinson & Hensel (1988) include microprobe analyses of glass and groundmass in samples from the 1868 eruption. Rims from this study with concentrations greater than  $Fo_{82}$  fall in the equilibrium range ( $Fo_{81}$ - $Fo_{85}$ ) calculated using  $K_D = 0.345 \pm 0.018$  (Matzen *et al.*, 2011) for these glass and groundmass compositions. Crystals in this study with rims lower than  $Fo_{80}$  are spread between  $Fo_{72}$ - $Fo_{79}$ , and do not have a clear distribution peak to indicate an equilibrium melt composition. Defining the true rim of a crystal can be difficult, so it is possible that “rim” analyses actually sample somewhere in the zoned part of the crystal.

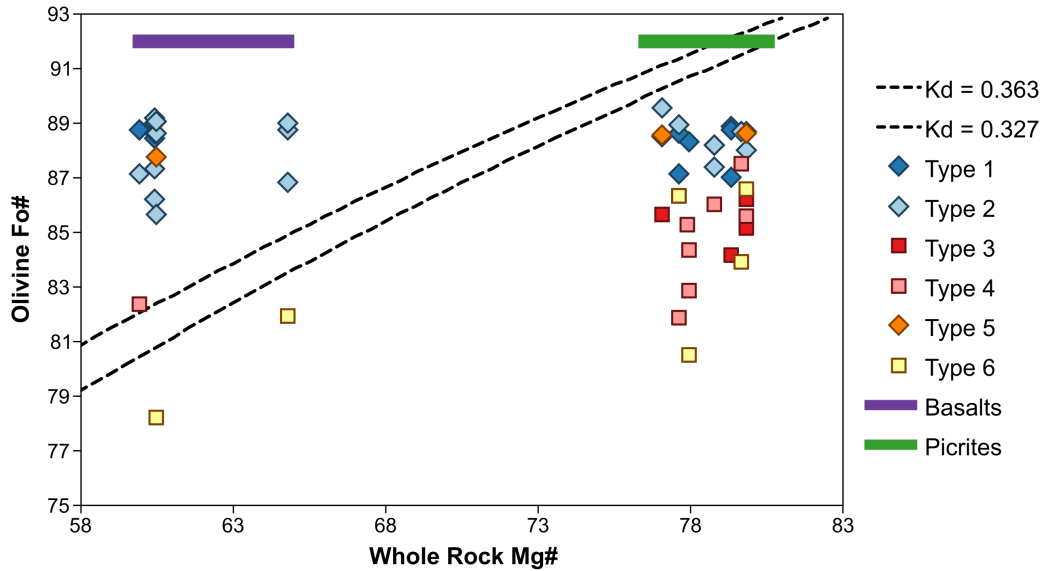


Figure 4.5. Olivine core Fo# compositions (average core plateaus) plotted with their corresponding sample whole rock Mg#. Dashed black lines represent equilibrium ranges between olivine and whole rock compositions, with  $K_D = 0.345 \pm 0.018$  (Matzen *et al.*, 2011). Purple and green bars at the top of the plot represent range of whole rock compositions for all analyzed samples of basalts and picrites, respectively (the vertical position does not imply an equilibrium Fo#). Symbols distinguish the six zoning types found in olivine crystals; see text for additional details.

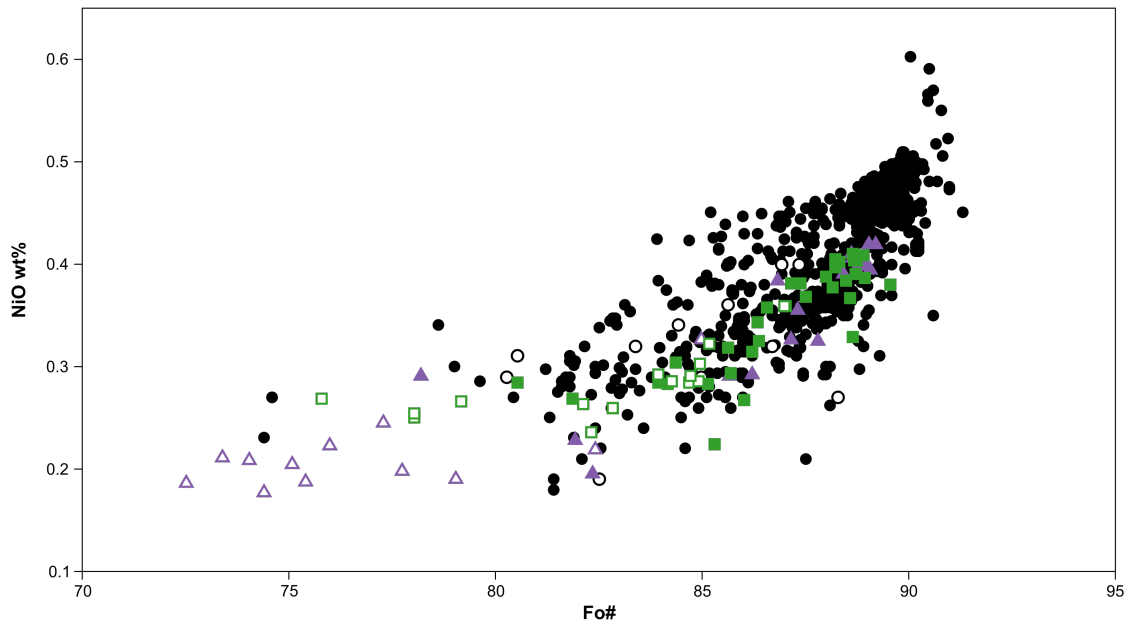


Figure 4.6. Measured NiO wt% plotted against Fo# in olivines from the 1868 eruption (purple triangles and green squares symbols for basalts and picrites, respectively) and Mauna Loa olivines from previous studies (black circles); see references in Figure 4.1. Filled symbols represent core analyses, and open symbols are rims. All analyses from literature data are plotted

as filled symbols, unless specified as rims. Core analyses are average plateau compositions, and rim points only include analyses that had acceptable totals at the crystal rims. Error bars from this study are smaller than the symbol size.

Olivine crystals from the 1868 eruption have core and rim compositions consistent with the trends of previous studies of Mauna Loa olivine (Figure 4.6). We focus on NiO-Fo relationships for this study, but our CaO-Fo and SiO<sub>2</sub>-Fo relationships also correspond with those of previous studies. The highest Fo# olivine crystals from the 1868 eruption have lower NiO compositions than some of the crystals from previous studies. These lower NiO values could reflect differences in the parental liquid compositions; Lynn *et al.*, (2017) demonstrated variations of ~0.1wt% NiO in olivine can occur from changes of ~100 ppm Ni in the parental melt; however, they went on to demonstrate that this variation for high Fo olivine (>Fo<sub>88</sub>) is more likely caused by variations in parental melt SiO<sub>2</sub> contents, which affect melt polymerization and nickel partition coefficients. At lower Fo values (<Fo<sub>88</sub>), NiO variation in olivine is due to magmatic processes including fractional crystallization, mixing, and diffusion (Lynn *et al.*, 2017). Most previously analyzed olivine from the SWRZ have similar ranges of NiO for given Fo values as those in this study (Figure 4.1); the higher NiO olivine crystals originating from other parts of Mauna Loa could experience different magmatic conditions than those erupting from the SWRZ.

#### 4.3.2.2 Crystal zoning

Olivine crystals in both the picrites and basalts exhibit normal and reverse zoning of Fo# (Figure 4.7). Normally zoned crystals have core compositions between Fo<sub>87.1</sub>-Fo<sub>89.5</sub>, with the exception of three normally zoned basalt crystals with core compositions below Fo<sub>87</sub> (Figure 4.5). Zoned crystals have wide homogeneous core plateaus (100s of microns up to >1mm), and narrow zoned rims ~50-100 microns from the edge of the crystal. Reverse zoning occurs with an increase in Fo relative to the core plateau, and then a drop to Fo values equal to, or lower than,

the core plateau composition at the outermost rim, making a hook-shape profile. Reverse zoning exists in only three of the nineteen basalt crystals analyzed. Previous studies of Mauna Loa olivine found reverse Fo zoning to be rare, and typically less than 1 Fo-unit (Baker *et al.*, 1996; Garcia *et al.*, 1995; Garcia, 1996), but olivine crystals erupted from Kilauea do commonly exhibit reverse zoning (Helz, 1987). Reversely zoned crystals in this study have an average Fo difference of 1 Fo-unit from the core plateau to maximum Fo, though the range of differences for all analyzed crystals is between 0.2-3.8 Fo-units.

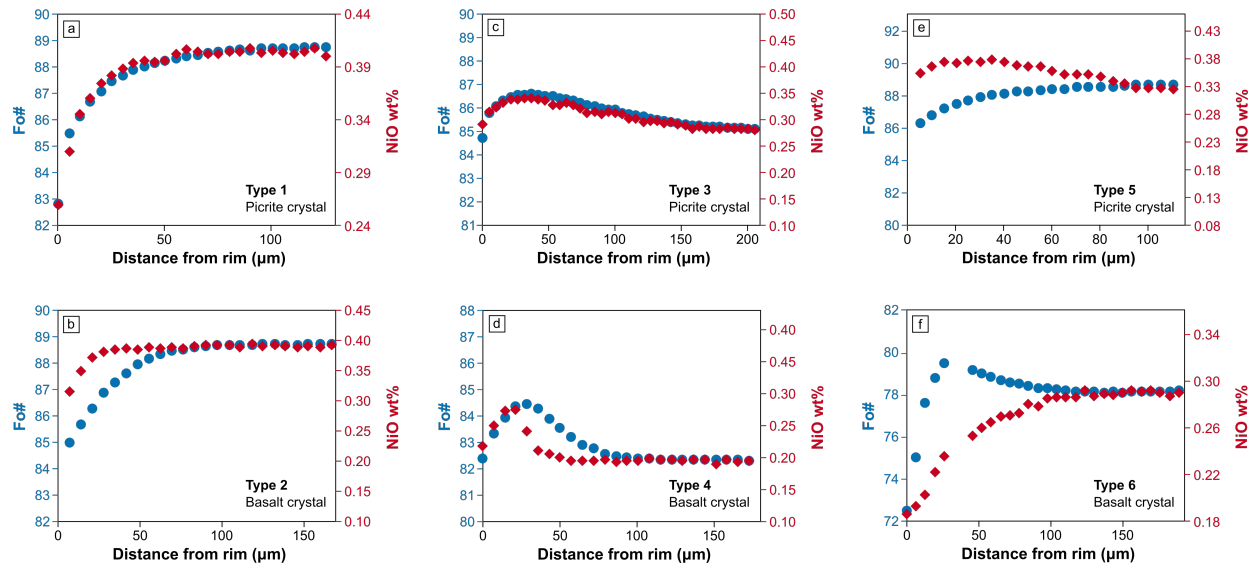


Figure 4.7. Examples of the 6 zoning varieties defined by olivine Fo# (blue circles) and NiO wt% (red diamonds) compositions; see text for more details. Note the changes in scales for all values and distances. Points within the traverses with unacceptable totals are not shown, and error bars for analyses are smaller than the size of the symbols.

We also consider NiO zoning in the olivine. Nickel, a compatible element in olivine that substitutes for iron and magnesium in the olivine crystal lattice, often corresponds to Fo zoning in olivine. We track both Fo and NiO for the crystal traverses, using the variety of zoning and the lengths of the zoned rims to define six main zoning populations (Figure 4.7, Table 4.1). All but nine analyzed crystals have zoning patterns that match for Fo and NiO (i.e. both components show normal or reverse zoning) (Figure 4.7a-d). We define the length of the zoned rim for a



crystal as the distance from the rim where variation from the mean core plateau composition of Fo or NiO exceeds the analytical error. We frequently see agreement between the plateau lengths for Fo and NiO in crystals with matching zoning varieties (Figure 4.7a,c). However, the lengths of these plateaus can be decoupled for Fo and NiO in both normally and reversely zoned crystals (Figure 4.7b,d). This decoupling is likely due to the differences in diffusion coefficients for Fe-Mg and Ni in olivine (Chakraborty, 2010). Nickel diffuses more slowly in olivine than Fe-Mg diffusion, which is consistent with the smaller rims in NiO than Fo (Figures 4.7b,d). The remaining nine crystals have mismatched zoning patterns for NiO and Fo, with one component normally zoned and the other reversely zoned (Figure 4.7e,f). In later discussion, these six zoning populations will be referred to as Types 1-6 (Table 4.1). All six types occur in crystals from both basalts and picrites, except Type 3, which only occurs in picrite crystals.

Table 4.1. Description of six zoning population types

Type	Fo Zoning	NiO Zoning	Fo-NiO coupling	Percent of analyzed olivine crystals
1	Normal	Normal	Coupled	22.6%
2	Normal	Normal	Decoupled	35.8%
3	Reverse	Reverse	Coupled	7.5%
4	Reverse	Reverse	Decoupled	17.0%
5	Normal	Reverse	Decoupled	5.7%
6	Reverse	Normal*	Decoupled	11.3%

\*Zoning is normal or unzoned (the crystal has a constant composition throughout the traverse, within analytical error).

These populations are primarily defined by the variety of zoning in NiO and Fo, but the zoning makes up only the outermost 50-100 microns of the crystal. The cores are much wider, and likely preserve conditions closer to those in which the crystals grew and/or were stored. Most of the normally zoned crystals with matching NiO zoning (Types 1 & 2) form a cluster at high Fo and NiO compositions (Figure 4.8), and all crystals with normal Fo zoning (Types 1, 2, & 5) contain cores with similar Fo values (Fo<sub>85.7</sub>-Fo<sub>89.5</sub>). The cores of reversely zoned crystals (Types 3, 4, &

6) have a larger range ( $Fo_{78.2}$ - $Fo_{87.5}$ ) (Figure 4.8). Distributions of core NiO values do not show distinct peaks in either the normally or reversely zoned crystals (except for the highest NiO-Fo olivines in Types 1 & 2), with normal zoning ranges between 0.29-0.42wt% NiO and reverse zoning ranges between 0.20-0.37wt% NiO.

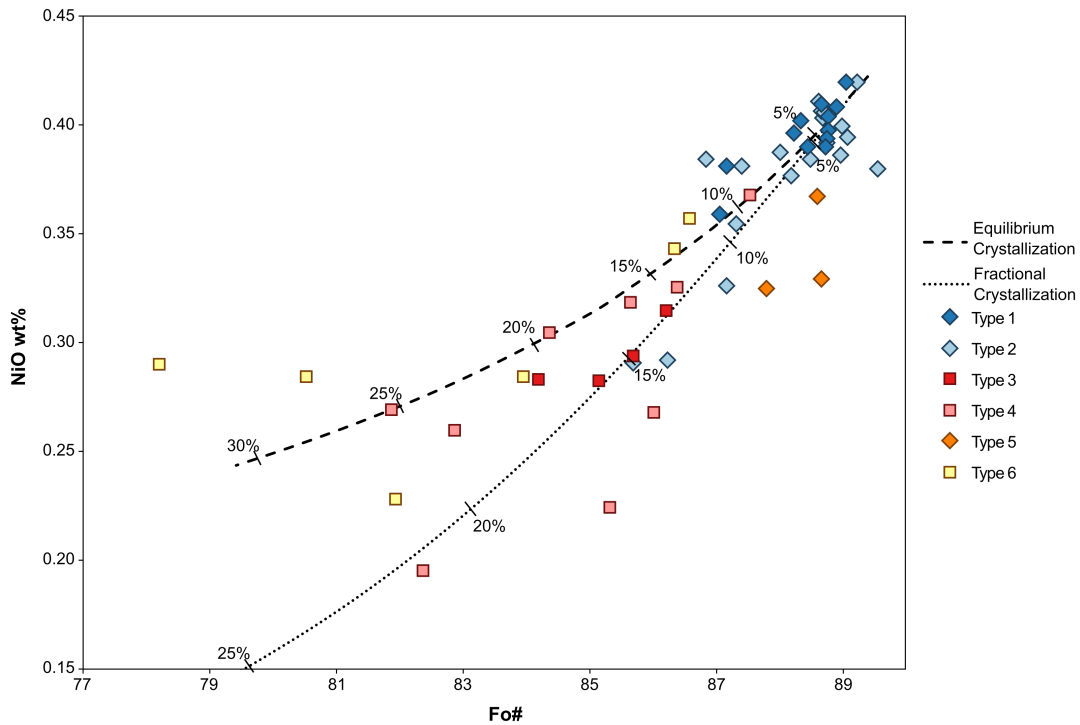


Figure 4.8. NiO-Fo relationships for cores of all crystal traverses, distinguished by zoning types. Diamond symbols represent crystals with normal zoning in Fo, square symbols represent reverse Fo zoning, and colors distinguish the NiO-Fo zoning relationships. Lines indicate the results of MELTS simulations at 1kbar, 0.3wt% H<sub>2</sub>O, starting value of 0.083wt%, and degrees of crystallization are indicated by percentages; see text for more details.

## 4.4 DISCUSSION

### 4.4.1 *Crystallization conditions of olivine*

The existence of the six zoning types in the basalts and picrites indicate that even a simple magmatic system has the potential to generate multiple populations of crystals. These populations are likely the result of a combination of crystal growth and storage in multiple magmatic environments, mixing of magmas between these environments, and diffusive re-

equilibration. In order to understand the conditions under which these different olivine populations developed, we ran MELTS simulations (Ghiorso & Gualda, 2015; Gualda *et al.*, 2012) to calculate the equilibrium mineral/melt assemblage for two parental compositions from Rhodes (1995) and (2015) (Table 4.2). Rhodes (1995) calculated a parental melt composition for the 1868 eruption, starting with MgO melt concentrations that would be in equilibrium with the highest Fo# olivine analyzed. He then calculated other components using MgO-oxide relationships from whole rock analyses. The starting composition of Rhodes (2015) includes parental compositions estimated for young lavas (<200ka) from Mauna Loa. We tested four initial NiO contents for the Rhodes (2015) starting composition: 0.09wt% and 0.11wt% from Lynn *et al.* (2017), and 0.064wt% and 0.083wt% from Gaffney (2002); these were also used as the starting composition of Rhodes (1995) in addition to his original estimate of 0.034wt%. We used an oxygen fugacity of QFM-1 based on measurement of a sample of 1868 glass Rhodes & Vollinger (2004). Each crystallization simulation began at 1500°C, with a temperature step of 1°C, and had a constant pressure of 1, 2, or 3 kbar. We tested a range of water contents (0.0, 0.1, 0.2, 0.3wt%) from melt inclusion measurements of Mauna Loa olivine (Fo<sub>88</sub>) (Wallace *et al.*, 2015).

The MELTS experiments with a starting composition from Rhodes (2015), a NiO composition of 0.083wt% from Gaffney (2002), water contents 0.1-0.3wt%, and a pressure of 1 kbar recreated many of the Ni-Fo relationships in core plateau compositions for olivine crystals from this study (Figure 4.8). Cores from Types 1 and 2 olivine appear to follow the fractional crystallization trend, though at high NiO-Fo values, equilibrium and fractional crystallization predict similar compositions. The lower Fo cores in Types 3 & 4 olivine, where both NiO and Fo

are reversely zoned, have a wider range of compositions and fall on both trends predicted by equilibrium and fractional crystallization.

Table 4.2. Starting compositions for MELTS simulations

	Rhodes (1995)	Rhodes (2015)
SiO <sub>2</sub>	50.29	48.44
TiO <sub>2</sub>	1.86	1.58
Al <sub>2</sub> O <sub>3</sub>	11.83	10.10
Fe <sub>2</sub> O <sub>3</sub>	1.22	12.27*
FeO	9.88	
MnO	0.17	0.17
MgO	13.00	17.40
CaO	9.07	7.96
Na <sub>2</sub> O	1.85	1.66
K <sub>2</sub> O	0.36	0.27
P <sub>2</sub> O <sub>5</sub>	0.22	0.17
NiO	0.034, 0.064, 0.083	0.064, 0.083, 0.09, 0.11
H <sub>2</sub> O	0, 0.1, 0.2, 0.3	0, 0.1, 0.2, 0.3

\*total Fe is expressed as Fe<sub>2</sub>O<sub>3</sub> for Rhodes (2015).

All values are in oxide wt%

Many of the crystals have homogeneous cores that are hundreds of microns wide, much larger than the widths of their rims, indicating they were kept at equilibrium conditions for much of their existence. Rhodes (1995) interpreted the 1852 and 1868 picrites to be the result of sampling a deeper, olivine-rich portion of a density-stratified magma reservoir, which is thermally and compositionally buffered by frequent intrusions of more primitive magma. A pressure of 1kbar produced the most reasonable mineral assemblages, with additional phases forming around 1170°C. Using a simple calculation of pressure and depth, with a constant density of 2800 kg/m<sup>3</sup>, 1kbar corresponds to a depth of ~3.6km. Previous geophysical and ground deformation studies of Mauna Loa inferred depths of the central summit reservoir to be 3-4km deep (Decker *et al.*, 1983; Okubo, 1995). Additionally, melt inclusions in Mauna Loa olivine (Fo<sub>88</sub>) from the Northeast Rift Zone indicate residence at shallow depths (0.5-1.1kbar) (Wallace *et al.*, 2015).

These depths therefore agree with the interpretation of Rhodes (1995) that these picrites represent magmas from the deeper portions of a density-stratified, shallow reservoir.

The MELTS simulations also predicted some of the evolving trends of NiO and Fo in the analyzed olivine crystal traverses (Figure 4.9). Many of the normally zoned picrite olivine crystals in Types 1 and 2 have zoned rims with fairly linear NiO-Fo relationships. Costa *et al.* (2008) showed NiO-Fo trends become more linear after a crystal undergoes diffusion, which is not modeled by MELTS. Basalt olivine crystals in Types 1 and 2 have cores that fall along the fractional crystallization trend. Moving through these crystals, the rims have kinked, concave-up trends, which Costa *et al.* (2008) demonstrated occurs in crystals growing in fractionally crystallizing magmas. The basalt compositions frequently extend beyond the NiO-Fo relationships where olivine was the only crystallizing phase as calculated by MELTS. We do not include compositions predicted when additional mineral phases crystallize because MELTS does not account for NiO partitioning into minerals other than olivine. Olivine was the only crystal phase present until 1200°C (with liquidus temperatures ~1420°C), after which clinopyroxene, orthopyroxene, and plagioclase crystallized. These minerals are consistent with the phases observed in the basalt samples, indicating that temperatures around 1200°C are present in part of the reservoir system encountered by some or all of the magma sourcing the 1868 eruption.

The cores of many of the reversely zoned crystals in olivine Types 3 and 4, from both picrites and basalts, also plot near the MELTS predicted fractional crystallization trend. The most primitive (i.e. highest NiO-Fo) compositions in some of these crystal traverses follow the fractional crystallization trend, which could indicate mixing occurred between multiple magmas related by fractional crystallization. These primitive compositions in the rims do not occur as plateaus, which would indicate the crystals resided in more primitive magmas until their

eruption. Instead they return to lower values at their rims, forming a hook-shaped profile. This could be the result of growth in an evolving liquid, or diffusive re-equilibration with a more evolved liquid. Mismatched NiO and Fo zoning distances in the rims of these crystals could reflect diffusion, due to the faster rate of iron-magnesium diffusion than nickel.

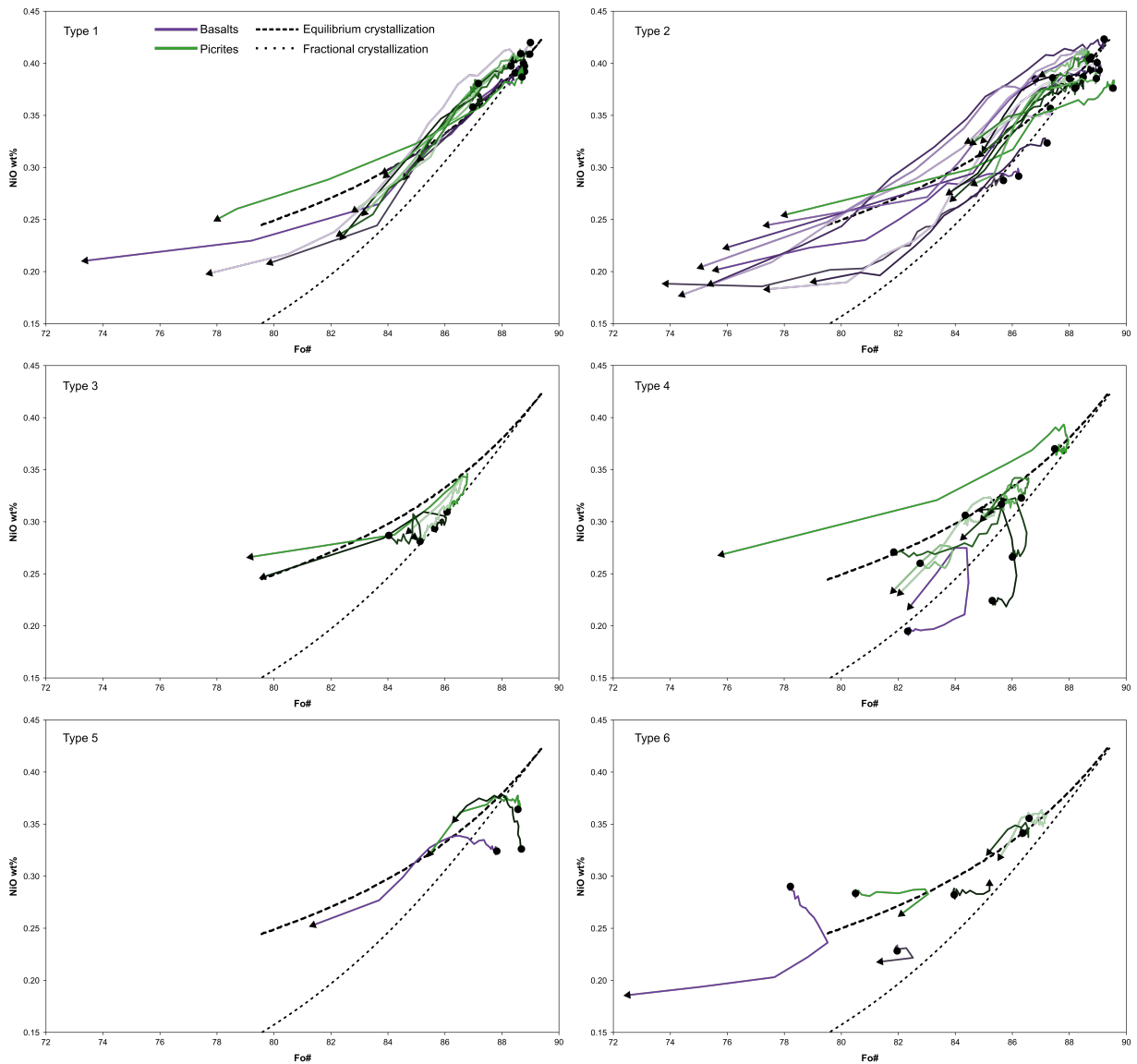


Figure 4.9. Evolution of NiOwt% and Fo# for the traverses of all crystals analyzed, separated by zoning types. Purple lines represent traverses from basalt crystals, and green lines are traverses from picrite crystals. Black circles and arrows represent olivine core and rim compositions, respectively. Dashed and dotted lines show crystallization trends calculated from MELTS, with the same conditions as in Figure 4.8.

The trends in the last two zoning populations, Types 5 and 6, do not follow the results of MELTS or those of the previous four types. Type 5, which has normal zoning in Fo, has very slight reverse zoning in NiO in two of the three crystals. These zoning patterns likely began with reverse zoning in both NiO and Fo. As the crystals resided in the reservoir, diffusive re-equilibration removed the reverse zoning of Fo faster than that of NiO, and thus, generated a normal zoning pattern in Fo while retaining the reverse NiO zoning. Type 6 crystals are much more complicated. They do not follow the trends predicted by MELTS, nor do they have similar core compositions or evolution of NiO-Fo relationships. These crystals are likely the result of a complex combination of magma mixing and diffusion. The Type 6 crystals identified in this study are in all different samples, and exist in both basalts and picrites.

#### 4.4.2 *The reservoir system of Mauna Loa*

The olivine crystals analyzed in this study represent the sampling of multiple magmatic environments and processes within the reservoir system of Mauna Loa. The high Fo# euhedral olivine cores likely crystallized and accumulated in the shallow summit reservoir, where replenishment from more primitive melts keeps the composition and temperature relatively constant (Rhodes, 1983, 1988). These crystals are frequently euhedral and do not exist as clusters forming from dense cumulates, but as single crystals or crystals growing in twinned pairs or ordered groupings (Welsch *et al.*, 2013). The high magma flux during this period (Lockwood & Lipman, 1987) could have kept the crystals in near-suspension, rather than forming dense olivine cumulates previously inferred for Hawaiian volcanoes (Clague & Denlinger, 1994).

The mobilization of the olivine-rich magma (mush) could have occurred from magmatic intrusions, similar to processes described in Chapter 2 of this dissertation. The intrusion of new magma would require additional storage space in the reservoir, so the mobilized mush could

have moved from the summit reservoir to the SWRZ reservoir system. These reservoirs are less frequently replenished than the central reservoir, which leads to melt evolution as mineral phases beyond olivine crystallize and form xenoliths (Gaffney, 2002). These magmas are considered evolved compared to the primitive magmas sourcing the summit reservoir, but based on MELTS simulations, additional phases begin crystallizing with  $\sim\text{Fo}_{77-79}$  olivine, after  $\sim 30\%$  crystallization from both the fractional and equilibrium crystallization runs.

After mobilization, crystals and melt from the mush likely mixed with the more evolved rift reservoir magmas. The distinct olivine contents in the picrites and basalts suggest that incomplete mixing occurred between the magmas. However, most of the olivine zoning types are represented in both picrites and basalts, which requires that some crystal exchange occurred between the two magmas. The varieties of zoning demonstrated by the six olivine populations indicate the crystals have complex histories, which include a series of multiple mixing events and storage in different conditions over a range of time scales.

Olivine crystals with similar core compositions making up Types 1 & 2 likely formed and grew in the same magmatic environments; the differences in their rim compositions and zoning could have resulted from different timescales of storage and incomplete mixing. The high Fo olivine cores in Types 1 & 2 represent those that grew in the central reservoir, with normally zoned rims forming from diffusive re-equilibration or growth in the more evolved rift magma. The decoupled zoning profiles for Fo and NiO in Type 2 crystals reflect the faster diffusion of iron-magnesium exchange than the diffusion of nickel; these crystals were likely stored in the more evolved magmas for longer than those of Type 1. The Type 1 & 2 olivine in the basalts generally have lower Fo rims than the olivine in the picrites, suggesting incomplete mixing between the mush and the rift reservoir melts.



Types 3 & 4 with reverse zoning tend to have more evolved cores than those of Types 1 & 2. These crystals could have originated in the rift reservoir, or grown from a mixture of the mush and rift magmas. The most primitive portions of the zoning profiles frequently fall along crystallization trends for the primitive magma calculated with MELTS. Entrainment of these cores by a mixture of the mush and rift magmas could have led to growth on the pre-existing crystals, in magma more primitive than the one in which they originally grew or were stored. The return to more evolved compositions at the outermost rim of the hook-shaped profiles once again suggests storage in a more evolved melt, with the crystals growing or undergoing diffusive equilibrium. The decoupled zoning profiles in Type 4 could reflect differences in storage timescales of the reversely zoned crystals. Crystal storage over even longer timescales could also explain the crystals of Type 5. The olivine making up this population could have originally been reversely zoned in both Fo and NiO. If they were stored in evolved melts long enough, the differences in diffusion timescales would have erased the original reverse zoning of Fo, generating a normal profile. The slower diffusion of nickel would have preserved the original reverse zoning if the crystals erupted before this zoning could also be diffusively erased.

The crystals of Type 6 are more difficult to explain. The cores of these crystals do not have similar Fo-NiO relationships to suggest similar growth and storage conditions. The mismatch in zoning type between NiO and Fo cannot be easily explained by crystal growth followed by diffusion: if the crystal began with a reverse zoning profile, the slower diffusion of nickel should produce a mismatch like that in Type 5. A series of growth, mixing, and diffusion events are likely required to explain the diversity of zoning seen in this final population, suggesting the storage and transport of olivine crystals through the mush and rift reservoirs are not straightforward.

This study of the 1868 eruption of Mauna Loa demonstrates that even a simple magmatic system can generate distinct populations of crystals. In order to determine the sequence of magmatic events that created these populations, it is necessary to consider the mechanics and geochemistry of the mush at both the crystal- and reservoir-scales. Resolving both these scales using the models in Chapters 2 and 3 demonstrates the crystal-scale control on magmatic mobilization, crystal and liquid mixing, and the formation of distinct magmatic environments within a single system. The results of these simple models can begin to provide insight into the complexities of magma mixing and the formation of crystal populations.

#### 4.4.3 *Future work: diffusion modeling*

Future work for this project includes using the diffusion software DIPRA (Girona & Costa, 2013) to recreate the different zoning patterns observed in the crystals from this eruption. If the zoning patterns can be successfully modeled, this will provide estimates of crystal residence timescales in a given magmatic environment. Understanding the residence times of crystals in these different conditions within Mauna Loa's magma reservoir could provide information about the transport of magma, especially during periods of high rift zone activity. As explained in Shea et al. (2015a), at least 20 crystal zoning patterns from a given population are needed to estimate accurate timescales. Following this advice, we have enough transects to accurately estimate the normally zoned crystals with high Fo cores ( $>F_{0.87}$ ).

## BIBLIOGRAPHY

- Alsaydalani, M. O. A. & Clayton, C. R. I. (2014). Internal Fluidization in Granular Soils. *Journal of Geotechnical and Geoenvironmental Engineering* **140**, 4013024.
- Andreotti, B., Forterre, Y. & Pouliquen, O. (2013). *Granular Media: Between Fluid and Solid*. Cambridge University Press.
- Baker, M. B., Alves, S. & Stolper, E. M. (1996). Petrography and petrology of the Hawaii Scientific Drilling Project lavas: Inferences from olivine phenocryst abundances and compositions. *Journal of Geophysical Research: Solid Earth* **101**, 11715–11727.
- Baker, S. & Amelung, F. (2012). Top-down inflation and deflation at the summit of Kīlauea Volcano, Hawai‘i observed with InSAR. *Journal of Geophysical Research (Solid Earth)* **117**, B12406.
- Barboni, M. & Schoene, B. (2014). Short eruption window revealed by absolute crystal growth rates in a granitic magma. *Nature Geoscience* **7**, 524–528.
- Bec, J., Celani, A., Cencini, M. & Musacchio, S. (2005). Clustering and collisions of heavy particles in random smooth flows. *Physics of Fluids* **17**, 73301.
- Bergantz, G. W. (2000). On the dynamics of magma mixing by reintrusion: implications for pluton assembly processes. *Journal of Structural Geology* **22**, 1297–1309.
- Bergantz, G. W. & Breidenthal, R. E. (2001). Non-stationary entrainment and tunneling eruptions: A dynamic link between eruption processes and magma mixing. *Geophysical Research Letters* **28**, 3075–3078.
- Bergantz, G. W., Schleicher, J. M. & Burgisser, A. (2015). Open-system dynamics and mixing in magma mushes. *Nature Geoscience* **8**, 793–796.
- Botev, Z. I., Grotowski, J. F. & Kroese, D. P. (2010). Kernel density estimation via diffusion. *The Annals of Statistics* **38**, 2916–2957.
- Bouzig, M., Trulsson, M., Claudin, P., Clément, E. & Andreotti, B. (2013). Nonlocal Rheology of Granular Flows across Yield Conditions. *Physical Review Letters* **111**, 238301.
- Boyer, F., Guazzelli, E. & Pouliquen, O. (2011). Unifying suspension and granular rheology. *Physical review letters* **107**, 188301.
- Breidenthal, R. E., Buonadonna, V. R. & Weisbach, M. F. (1990). Molecular mixing via jets in confined volumes. *Journal of Fluid Mechanics* **219**, 531–544.
- Broadwell, J. E. & Breidenthal, R. E. (1982). A simple model of mixing and chemical reaction in a turbulent shear layer. *Journal of Fluid Mechanics* **125**, 397–410.

- Broadwell, J. E. & Mungal, M. G. (1991). Large-scale structures and molecular mixing. *Physics of Fluids A: Fluid Dynamics* **3**, 1193–1206.
- Burgisser, A. & Bergantz, G. W. (2011). A rapid mechanism to remobilize and homogenize highly crystalline magma bodies. *Nature* **471**, 212–215.
- Burgisser, A., Bergantz, G. W. & Breidenthal, R. E. (2005). Addressing complexity in laboratory experiments: the scaling of dilute multiphase flows in magmatic systems. *Journal of Volcanology and Geothermal Research* **141**, 245–265.
- Campbell, C. S. (2006). Granular material flows – An overview. *Powder Technology* **162**, 208–229.
- Cassar, C., Nicolas, M. & Pouliquen, O. (2005). Submarine granular flows down inclined planes. *Physics of Fluids (1994-present)* **17**, 103301.
- Cates, M. E., Wittmer, J. P., Bouchaud, J.-P. & Claudin, P. (1998). Jamming, force chains, and fragile matter. *Physical Review Letters* **81**, 1841–1844.
- Chakraborty, S. (2010). Diffusion Coefficients in Olivine, Wadsleyite and Ringwoodite. *Reviews in Mineralogy and Geochemistry* **72**, 603–639.
- Charlier, B. L. A., Bachmann, O., Davidson, J. P., Dungan, M. A. & Morgan, D. J. (2007). The Upper Crustal Evolution of a Large Silicic Magma Body: Evidence from Crystal-scale Rb–Sr Isotopic Heterogeneities in the Fish Canyon Magmatic System, Colorado. *Journal of Petrology* **48**, 1875–1894.
- Chen, Y. & Zhang, Y. (2008). Olivine dissolution in basaltic melt. *Geochimica et Cosmochimica Acta* **72**, 4756–4777.
- Clague, D. A. & Denlinger, R. P. (1994). Role of olivine cumulates in destabilizing the flanks of Hawaiian volcanoes. *Bulletin of Volcanology* **56**, 425–434.
- Coetzee, C. J. & Els, D. N. J. (2009). Calibration of discrete element parameters and the modelling of silo discharge and bucket filling. *Computers and Electronics in Agriculture* **65**, 198–212.
- Cohen, A. S., Keith O’Nions, R. & Kurz, M. D. (1996). Chemical and isotopic variations in Mauna Loa tholeiites. *Earth and Planetary Science Letters* **143**, 111–124.
- Coltice, N. & Schmalzl, J. (2006). Mixing times in the mantle of the early Earth derived from 2-D and 3-D numerical simulations of convection. *Geophysical Research Letters* **33**.
- Cooper, K. M. (2015). Timescales of crustal magma reservoir processes: insights from U-series crystal ages. *Geological Society, London, Special Publications* **422**, 141–174.
- Cooper, K. M. & Kent, A. J. R. (2014). Rapid remobilization of magmatic crystals kept in cold storage. *Nature* **506**, 480–483.

- Cooper, K. M., Sims, K. W. W., Eiler, J. M. & Banerjee, N. (2016). Timescales of storage and recycling of crystal mush at Krafla Volcano, Iceland. *Contributions to Mineralogy and Petrology* **171**, 1–19.
- Costa, F., Coogan, L. A. & Chakraborty, S. (2010). The time scales of magma mixing and mingling involving primitive melts and melt–mush interaction at mid-ocean ridges. *Contributions to Mineralogy and Petrology* **159**, 371–387.
- Costa, F., Dohmen, R. & Chakraborty, S. (2008). Time Scales of Magmatic Processes from Modeling the Zoning Patterns of Crystals. *Reviews in Mineralogy and Geochemistry* **69**, 545–594.
- Costa, F. & Morgan, D. (2011). Time constraints from chemical equilibrium in magmatic crystals. In: Dosseto, A., Turner, S. & Van-Orman, J. (eds) *Timescales of Magmatic Processes*. John Wiley & Sons, 125–159.
- Cui, X., Li, J., Chan, A. & Chapman, D. (2014). Coupled DEM–LBM simulation of internal fluidisation induced by a leaking pipe. *Powder Technology* **254**, 299–306.
- Cundall, P. A. & Strack, O. D. L. (1979). A Discrete Numerical Model for Granular Assemblies. *Geotechnique* **29**, 47–65.
- da Cruz, F., Emam, S., Prochnow, M., Roux, J.-N. & Chevoir, F. (2005). Rheophysics of dense granular materials: Discrete simulation of plane shear flows. *Physical Review E* **72**, 21309.
- Daerr, A. & Douady, S. (1999). Sensitivity of granular surface flows to preparation. *EPL (Europhysics Letters)* **47**, 324.
- Danyushevsky, L. V., Leslie, R. a. J., Crawford, A. J. & Durance, P. (2004). Melt Inclusions in Primitive Olivine Phenocrysts: the Role of Localized Reaction Processes in the Origin of Anomalous Compositions. *Journal of Petrology* **45**, 2531–2553.
- Davidson, J. P., Hora, J. M., Garrison, J. M. & Dungan, M. A. (2005). Crustal forensics in arc magmas. *Journal of Volcanology and Geothermal Research* **140**, 157–170.
- Davidson, J. P., Morgan, D. J., Charlier, B. L. A., Harlou, R. & Hora, J. M. (2007). Microsampling and Isotopic Analysis of Igneous Rocks: Implications for the Study of Magmatic Systems. *Annual Review of Earth and Planetary Sciences* **35**, 273–311.
- Davidson, J., Tepley III, F., Palacz, Z. & Meffan-Main, S. (2001). Magma recharge, contamination and residence times revealed by in situ laser ablation isotopic analysis of feldspar in volcanic rocks. *Earth and Planetary Science Letters* **184**, 427–442.
- Decker, R. W., Koyanagi, R. Y., Dvorak, J. J., Lockwood, J. P., Okamura, A. T., Yamashita, K. M. & Tanigawa, W. R. (1983). Seismicity and surface deformation of Mauna Loa Volcano, Hawaii. *EOS Transactions* **64**, 545–547.

- Deen, N. G., Willem, G., Sander, G. & Kuipers, J. A. M. (2010). Numerical Analysis of Solids Mixing in Pressurized Fluidized Beds. *Industrial & Engineering Chemistry Research* **49**, 5246–5253.
- Dimotakis, P. E. (2005). Turbulent Mixing. *Annual Review of Fluid Mechanics* **37**, 329–356.
- Donaldson, C. H. (1985). The rates of dissolution of olivine, plagioclase, and quartz in a basalt melt. *Mineralogical Magazine* **49**, 683–693.
- Doucet, J., Bertrand, F. & Chaouki, J. (2008). A measure of mixing from Lagrangian tracking and its application to granular and fluid flow systems. *Chemical Engineering Research and Design* **86**, 1313–1321.
- du Pont, S. C., Gondret, P., Perrin, B. & Rabaud, M. (2003). Granular avalanches in fluids. *Physical Review Letters* **90**, 44301.
- Dufek, J. & Bergantz, G. W. (2007). Suspended load and bed-load transport of particle-laden gravity currents: the role of particle–bed interaction. *Theoretical and Computational Fluid Dynamics* **21**, 119–145.
- Eppich, G. R., Cooper, K. M., Kent, A. J. R. & Koleszar, A. (2012). Constraints on crystal storage timescales in mixed magmas: Uranium-series disequilibria in plagioclase from Holocene magmas at Mount Hood, Oregon. *Earth and Planetary Science Letters* **317–318**, 319–330.
- Ergun, S. (1952). Fluid flow through packed columns. *Chemical Engineering Progress* **48**, 89–94.
- Estep, J. & Dufek, J. (2012). Substrate effects from force chain dynamics in dense granular flows. *Journal of Geophysical Research: Earth Surface* **117**, F01028.
- Farnetani, C. G. & Samuel, H. (2003). Lagrangian structures and stirring in the Earth’s mantle. *Earth and Planetary Science Letters* **206**, 335–348.
- Ferrachat, S. & Ricard, Y. (1998). Regular vs. chaotic mantle mixing. *Earth and Planetary Science Letters* **155**, 75–86.
- Forterre, Y. & Pouliquen, O. (2008). Flows of Dense Granular Media. *Annual Review of Fluid Mechanics* **40**, 1–24.
- Gaffney, A. M. (2002). Environments of Crystallization and Compositional Diversity of Mauna Loa Xenoliths. *Journal of Petrology* **43**, 963–981.
- Garcia, M. O. (1996). Petrography and olivine and glass chemistry of lavas from the Hawaii Scientific Drilling Project. *Journal of Geophysical Research: Solid Earth* **101**, 11701–11713.

- Garcia, M. O., Hulsebosch, T. P. & Rhodes, J. M. (1995). Olivine-Rich Submarine Basalts from the Southwest Rift Zone of Mauna Loa Volcano: Implications for Magmatic Processes and Geochemical Evolution. In: Rhodes, J. M. & Lockwood, J. P. (eds) *Mauna Loa Revealed: Structure, Composition, History, and Hazards*. American Geophysical Union, 219–239.
- Garg, R., Galvin, J., Li, T. & Pannala, S. (2012a). Open-source MFIX-DEM software for gas–solids flows: Part I—Verification studies. *Powder Technology* **220**, 122–137.
- Garg, R., Galvin, J., Li, T. & Pannala, S. (2012b). Documentation of open-source MFIX–DEM software for gas–solids flows. .
- Geirsson, H. *et al.* (2012). Volcano deformation at active plate boundaries: Deep magma accumulation at Hekla volcano and plate boundary deformation in south Iceland. *Journal of Geophysical Research: Solid Earth* **117**, B11409.
- Geist, D. J., Fornari, D. J., Kurz, M. D., Harpp, K. S., Adam Soule, S., Perfit, M. R. & Koleszar, A. M. (2006). Submarine Fernandina: Magmatism at the leading edge of the Galápagos hot spot. *Geochemistry, Geophysics, Geosystems* **7**, Q12007.
- Gerbi, C., Johnson, S. E. & Paterson, S. R. (2004). Implications of rapid, dike-fed pluton growth for host-rock strain rates and emplacement mechanisms. *Journal of Structural Geology* **26**, 583–594.
- Ghiorso, M. S. & Gualda, G. A. R. (2015). An H<sub>2</sub>O–CO<sub>2</sub> mixed fluid saturation model compatible with rhyolite-MELTS. *Contributions to Mineralogy and Petrology* **169**, 53.
- Ginibre, C., Wörner, G. & Kronz, A. (2007). Crystal Zoning as an Archive for Magma Evolution. *Elements* **3**, 261–266.
- Girard, G. & Stix, J. (2009). Buoyant replenishment in silicic magma reservoirs: Experimental approach and implications for magma dynamics, crystal mush remobilization, and eruption. *Journal of Geophysical Research: Solid Earth* **114**, B08203.
- Girona, T. & Costa, F. (2013). DIPRA: A user-friendly program to model multi-element diffusion in olivine with applications to timescales of magmatic processes. *Geochemistry, Geophysics, Geosystems* **14**, 422–431.
- Glazner, A. F. (2014). Magmatic life at low Reynolds number. *Geology* **42**, 935–938.
- Goldhirsch, I. (2003). Rapid Granular Flows. *Annual Review of Fluid Mechanics* **35**, 267–293.
- Gualda, G. A. R., Ghiorso, M. S., Lemons, R. V. & Carley, T. L. (2012). Rhyolite-MELTS: a modified calibration of MELTS optimized for silica-rich, fluid-bearing magmatic systems. *Journal of Petrology* **53**, 875–890.
- Guazzelli, É. & Morris, J. F. (2012). *A Physical Introduction to Suspension Dynamics*. Cambridge University Press.

- Hansen, H. & Grönvold, K. (2000). Plagioclase ultraphyric basalts in Iceland: the mush of the rift. *Journal of Volcanology and Geothermal Research* **98**, 1–32.
- Helz, R. T. (1987). Diverse olivine types in lava of the 1959 eruption of Kilauea Volcano and their bearing on eruption dynamics. *U.S. Geological Survey Professional Paper* **1350**, 691–722.
- Hitchcock, C. H. (1911). *Hawaii and Its Volcanoes*. Hawaiian Gazette Company.
- Hodge, K. F., Carazzo, G. & Jellinek, A. M. (2012). Experimental constraints on the deformation and breakup of injected magma. *Earth and Planetary Science Letters* **325–326**, 52–62.
- Huber, C., Bachmann, O. & Dufek, J. (2012). Crystal-poor versus crystal-rich ignimbrites: A competition between stirring and reactivation. *Geology* **40**, 115–118.
- Huppert, H. E., Sparks, R. S. J., Whitehead, J. A. & Hallworth, M. A. (1986). Replenishment of magma chambers by light inputs. *Journal of Geophysical Research: Solid Earth* **91**, 6113–6122.
- Jaeger, H. M., Nagel, S. R. & Behringer, R. P. (1996). Granular solids, liquids, and gases. *Reviews of Modern Physics* **68**, 1259–1273.
- Jellinek, A. M., Kerr, R. C. & Griffiths, R. W. (1999). Mixing and compositional stratification produced by natural convection: 1. Experiments and their application to Earth's core and mantle. *Journal of Geophysical Research: Solid Earth* **104**, 7183–7201.
- Jerram, D. A., Cheadle, M. J. & Philpotts, A. R. (2003). Quantifying the Building Blocks of Igneous Rocks: Are Clustered Crystal Frameworks the Foundation? *Journal of Petrology* **44**, 2033–2051.
- Jerram, D. A. & Martin, V. M. (2008). Understanding crystal populations and their significance through the magma plumbing system. *Geological Society, London, Special Publications* **304**, 133–148.
- Johnsen, Ø., Chevalier, C., Lindner, A., Toussaint, R., Clément, E., Måløy, K. J., Flekkøy, E. G. & Schmittbuhl, J. (2008). Decompaction and fluidization of a saturated and confined granular medium by injection of a viscous liquid or gas. *Physical Review E* **78**, 51302.
- Johnson, D. J., Eggers, A. A., Bagnardi, M., Battaglia, M., Poland, M. P. & Miklius, A. (2010). Shallow magma accumulation at Kīlauea Volcano, Hawai‘i, revealed by microgravity surveys. *Geology* **38**, 1139–1142.
- Jop, P. (2015). Rheological properties of dense granular flows. *Comptes Rendus Physique* **16**, 62–72.
- Kahl, M., Chakraborty, S., Costa, F. & Pompilio, M. (2011). Dynamic plumbing system beneath volcanoes revealed by kinetic modeling, and the connection to monitoring data: An example from Mt. Etna. *Earth and Planetary Science Letters* **308**, 11–22.



- Kahl, M., Chakraborty, S., Costa, F., Pompilio, M., Liuzzo, M. & Viccaro, M. (2013). Compositionally zoned crystals and real-time degassing data reveal changes in magma transfer dynamics during the 2006 summit eruptive episodes of Mt. Etna. *Bulletin of Volcanology* **75**, 1–14.
- Kahl, M., Chakraborty, S., Pompilio, M. & Costa, F. (2015). Constraints on the Nature and Evolution of the Magma Plumbing System of Mt. Etna Volcano (1991–2008) from a Combined Thermodynamic and Kinetic Modelling of the Compositional Record of Minerals. *Journal of Petrology* **56**, 2025–2068.
- Kamrin, K. & Koval, G. (2012). Nonlocal constitutive relation for steady granular flow. *Physical Review Letters* **108**, 178301.
- Kellogg, L. H. & Turcotte, D. L. (1990). Mixing and the distribution of heterogeneities in a chaotically convecting mantle. *Journal of Geophysical Research: Solid Earth* **95**, 421–432.
- Kerr, R. C. (1995). Convective crystal dissolution. *Contributions to Mineralogy and Petrology* **121**, 237–246.
- Klemetti, E. W. & Clyne, M. A. (2014). Localized Rejuvenation of a Crystal Mush Recorded in Zircon Temporal and Compositional Variation at the Lassen Volcanic Center, Northern California. *PLOS ONE* **9**, e113157.
- Kurz, M. D., Kenna, T. C., Kammer, D. P., Rhodes, J. M. & Garcia, M. O. (1995). Isotopic Evolution of Mauna Loa Volcano: A View From the Submarine Southwest Rift Zone. In: Rhodes, J. M. & Lockwood, J. P. (eds) *Mauna Loa Revealed: Structure, Composition, History, and Hazards*. American Geophysical Union, 289–306.
- Laumonier, M., Scaillet, B., Arbaret, L. & Champallier, R. (2014). Experimental simulation of magma mixing at high pressure. *Lithos* **196**, 281–300.
- Lemaître, A., Roux, J.-N. & Chevoir, F. (2009). What do dry granular flows tell us about dense non-Brownian suspension rheology? *Rheologica Acta* **48**, 925–942.
- Li, T., Garg, R., Galvin, J. & Pannala, S. (2012). Open-source MFI-X-DEM software for gas-solids flows: Part II — Validation studies. *Powder Technology* **220**, 138–150.
- Li, T. & Guenther, C. (2012). MFI-X-DEM simulations of change of volumetric flow in fluidized beds due to chemical reactions. *Powder Technology* **220**, 70–78.
- Liang, Y. (2000). Dissolution in molten silicates: effects of solid solution. *Geochimica et Cosmochimica Acta* **64**, 1617–1627.
- Lockwood, J. P. (1995). Mauna Loa Eruptive History—The Preliminary Radiocarbon Record. In: Rhodes, J. M. & Lockwood, J. P. (eds) *Mauna Loa Revealed: Structure, Composition, History, and Hazards*. American Geophysical Union, 81–94.

- Lockwood, J. P. & Lipman, P. W. (1987). Holocene eruptive history of Mauna Loa volcano. *U.S. Geological Survey Professional Paper* **1350**, 509–535.
- Lynn, K. J., Shea, T. & Garcia, M. O. (2017). Nickel variability in Hawaiian olivine: Evaluating the relative contributions from mantle and crustal processes. *American Mineralogist* **102**, 507–518.
- Marsh, B. D. (1981). On the crystallinity, probability of occurrence, and rheology of lava and magma. *Contributions to Mineralogy and Petrology* **78**, 85–98.
- Marsh, B. D. (1988). Crystal size distribution (CSD) in rocks and the kinetics and dynamics of crystallization. *Contributions to Mineralogy and Petrology* **99**, 277–291.
- Marsh, B. D. (1998). On the Interpretation of Crystal Size Distributions in Magmatic Systems. *Journal of Petrology* **39**, 553–599.
- Martin, V. M., Davidson, J., Morgan, D. & Jerram, D. A. (2010). Using the Sr isotope compositions of feldspars and glass to distinguish magma system components and dynamics. *Geology* **38**, 539–542.
- Marzougui, D., Chareyre, B. & Chauchat, J. (2015). Microscopic origins of shear stress in dense fluid–grain mixtures. *Granular Matter* **17**, 297–309.
- Matzen, A. K., Baker, M. B., Beckett, J. R. & Stolper, E. M. (2011). Fe–Mg Partitioning between Olivine and High-magnesian Melts and the Nature of Hawaiian Parental Liquids. *Journal of Petrology* **52**, 1243–1263.
- McKenzie, D. (1984). The Generation and Compaction of Partially Molten Rock. *Journal of Petrology* **25**, 713–765.
- MiDi, G. D. R. (2004). On dense granular flows. *The European Physical Journal E* **14**, 341–365.
- Moore, A., Coogan, L. A., Costa, F. & Perfit, M. R. (2014). Primitive melt replenishment and crystal-mush disaggregation in the weeks preceding the 2005–2006 eruption, 9° 50' N, EPR. *Earth and Planetary Science Letters* **403**, 15–26.
- Mutabaruka, P., Delenne, J.-Y., Soga, K. & Radjai, F. (2014). Initiation of immersed granular avalanches. *Physical Review E* **89**, 52203.
- Nakamura, H. & Watano, S. (2007). Numerical modeling of particle fluidization behavior in a rotating fluidized bed. *Powder Technology* **171**, 106–117.
- Neave, D. A., MacLennan, J., Hartley, M. E., Edmonds, M. & Thordarson, T. (2014). Crystal Storage and Transfer in Basaltic Systems: the Skuggafjöll Eruption, Iceland. *Journal of Petrology* **egu058**.

- Neave, D. A., Passmore, E., Maclennan, J., Fitton, G. & Thordarson, T. (2013). Crystal–melt relationships and the record of deep mixing and crystallization in the ad 1783 Laki Eruption, Iceland. *Journal of Petrology* **54**, 1661–1690.
- Ness, C. & Sun, J. (2015). Flow regime transitions in dense non-Brownian suspensions: Rheology, microstructural characterization, and constitutive modeling. *Physical Review E* **91**, 12201.
- Ness, C. & Sun, J. (2016). Two-scale evolution during shear reversal in dense suspensions. *Physical Review E* **93**, 12604.
- Okubo, P. G. (1995). A Seismological Framework for Mauna Loa Volcano, Hawaii. In: Rhodes, J. M. & Lockwood, J. P. (eds) *Mauna Loa Revealed: Structure, Composition, History, and Hazards*. American Geophysical Union, 187–197.
- Oldenburg, C. M., Spera, F. J., Yuen, D. A. & Sewell, G. (1989). Dynamic mixing in magma bodies: Theory, simulations, and implications. *Journal of Geophysical Research: Solid Earth* **94**, 9215–9236.
- Parks, M. M. *et al.* (2012). Evolution of Santorini Volcano dominated by episodic and rapid fluxes of melt from depth. *Nature Geoscience* **5**, 749–754.
- Passmore, E., Maclennan, J., Fitton, G. & Thordarson, T. (2012). Mush disaggregation in basaltic magma chambers: Evidence from the ad 1783 Laki Eruption. *Journal of Petrology* **53**, 2593–2623.
- Paterson, S. R. (2009). Magmatic tubes, pipes, troughs, diapirs, and plumes: Late-stage convective instabilities resulting in compositional diversity and permeable networks in crystal-rich magmas of the Tuolumne batholith, Sierra Nevada, California. *Geosphere* **5**, 496–527.
- Paulick, M., Morgeneyer, M. & Kwade, A. (2015). Review on the influence of elastic particle properties on DEM simulation results. *Powder Technology* **283**, 66–76.
- Peng, Z., Doroodchi, E., Luo, C. & Moghtaderi, B. (2014). Influence of void fraction calculation on fidelity of CFD-DEM simulation of gas-solid bubbling fluidized beds. *AIChE Journal* **60**, 2000–2018.
- Perugini, D., De Campos, C. P., Ertel-Ingrisch, W. & Dingwell, D. B. (2012). The space and time complexity of chaotic mixing of silicate melts: Implications for igneous petrology. *Lithos* **155**, 326–340.
- Perugini, D. & Poli, G. (2005). Viscous fingering during replenishment of felsic magma chambers by continuous inputs of mafic magmas: Field evidence and fluid-mechanics experiments. *Geology* **33**, 5–8.
- Perugini, D. & Poli, G. (2012). The mixing of magmas in plutonic and volcanic environments: Analogies and differences. *Lithos* **153**, 261–277.

- Peters, I. R., Majumdar, S. & Jaeger, H. M. (2016). Direct observation of dynamic shear jamming in dense suspensions. *Nature* **532**, 214–217.
- Philippe, P. & Badiane, M. (2013). Localized fluidization in a granular medium. *Physical Review E* **87**, 42206.
- Philpotts, A. R., Brustman, C. M., Shi, J., Carlson, W. D. & Denison, C. (1999). Plagioclase-chain networks in slowly cooled basaltic magma. *American Mineralogist* **84**, 1819–1829.
- Poland, M. P., Miklius, A., Jeff Sutton, A. & Thornber, C. R. (2012). A mantle-driven surge in magma supply to Kilauea Volcano during 2003-2007. *Nature Geoscience* **5**, 295–300.
- Poux, M., Fayolle, P., Bertrand, J., Bridoux, D. & Bousquet, J. (1991). Powder mixing: Some practical rules applied to agitated systems. *Powder Technology* **68**, 213–234.
- Putirka, K. D. (2008). Thermometers and barometers for volcanic systems. *Reviews in Mineralogy and Geochemistry* **69**, 61–120.
- Reid, M. R. (2008). How long does it take to supersize an eruption? *Elements* **4**, 23–28.
- Rhodes, J. M. (1983). Homogeneity of lava flows: Chemical data for historic Mauna Loa eruptions. *Journal of Geophysical Research: Solid Earth* **88**, A869–A879.
- Rhodes, J. M. (1988). Geochemistry of the 1984 Mauna Loa Eruption: Implications for magma storage and supply. *Journal of Geophysical Research: Solid Earth* **93**, 4453–4466.
- Rhodes, J. M. (1995). The 1852 and 1868 Mauna Loa Picrite Eruptions: Clues to Parental Magma Compositions and the Magmatic Plumbing System. In: Rhodes, J. M. & Lockwood, J. P. (eds) *Mauna Loa Revealed: Structure, Composition, History, and Hazards*. American Geophysical Union, 241–262.
- Rhodes, J. M. (2015). Major-Element and Isotopic Variations in Mauna Loa Magmas over 600 ka. In: Carey, R., Cayol, V., Poland, M. & Weis, D. (eds) *Hawaiian Volcanoes*. John Wiley & Sons, Inc, 59–78.
- Rhodes, J. M. & Hart, S. R. (1995). Episodic Trace Element and Isotopic Variations in Historical Mauna Loa Lavas: Implications for Magma and Plume Dynamics. In: Rhodes, J. M. & Lockwood, J. P. (eds) *Mauna Loa Revealed: Structure, Composition, History, and Hazards*. American Geophysical Union, 263–288.
- Rhodes, J. M. & Vollinger, M. J. (2004). Composition of basaltic lavas sampled by phase-2 of the Hawaii Scientific Drilling Project: Geochemical stratigraphy and magma types. *Geochemistry, Geophysics, Geosystems* **5**, n/a–n/a.
- Richter, F. M., Davis, A. M., DePaolo, D. J. & Watson, E. B. (2003). Isotope fractionation by chemical diffusion between molten basalt and rhyolite. *Geochimica et Cosmochimica Acta* **67**, 3905–3923.

- Riker, J. M., Cashman, K. V., Kauahikaua, J. P. & Montierth, C. M. (2009). The length of channelized lava flows: Insight from the 1859 eruption of Mauna Loa Volcano, Hawai‘i. *Journal of Volcanology and Geothermal Research* **183**, 139–156.
- Roux, J.-N. (2009). The nature of quasistatic deformation in granular materials. In: García-Rojo, R., Herrmann, H. J. & McNamara, S. (eds) *Powders and Grains, Proceedings of the 5th International Conference on Micromechanics of Granular Media, Stuttgart, Germany, 18–22 July 2005*, 261–265.
- Rudge, J. F. (2008). Finding peaks in geochemical distributions: A re-examination of the helium-continental crust correlation. *Earth and Planetary Science Letters* **274**, 179–188.
- Ruprecht, P., Bergantz, G. W., Cooper, K. M. & Hildreth, W. (2012). The Crustal Magma Storage System of Volcán Quizapu, Chile, and the Effects of Magma Mixing on Magma Diversity. *Journal of Petrology* **53**, 801–840.
- Ruprecht, P., Bergantz, G. W. & Dufek, J. (2008). Modeling of gas-driven magmatic overturn: Tracking of phenocryst dispersal and gathering during magma mixing. *Geochemistry, Geophysics, Geosystems* **9**, Q07017.
- Rutherford, M. J. (2008). Magma Ascent Rates. *Reviews in Mineralogy and Geochemistry* **69**, 241–271.
- Sakyi, P. A., Tanaka, R., Kobayashi, K. & Nakamura, E. (2012). Inherited Pb isotopic records in olivine antecryst-hosted melt inclusions from Hawaiian lavas. *Geochimica et Cosmochimica Acta* **95**, 169–195.
- Sandnes, B., Flekkøy, E. G., Knudsen, H. A., Måløy, K. J. & See, H. (2011). Patterns and flow in frictional fluid dynamics. *Nature Communications* **2**, 288.
- Sato, E. & Sato, H. (2009). Study of effect of magma pocket on mixing of two magmas with different viscosities and densities by analogue experiments. *Journal of Volcanology and Geothermal Research* **181**, 115–123.
- Schleicher, J. M., Bergantz, G. W., Breidenthal, R. E. & Burgisser, A. (2016). Time scales of crystal mixing in magma mushes. *Geophysical Research Letters* **43**, 1543–1550.
- Schmitt, A. K. (2011). Uranium series accessory crystal dating of magmatic processes. *Annual Review of Earth and Planetary Sciences* **39**, 321–349.
- Shea, T., Costa, F., Krimer, D. & Hammer, J. E. (2015a). Accuracy of timescales retrieved from diffusion modeling in olivine: A 3D perspective. *American Mineralogist* **100**, 2026–2042.
- Shea, T., Lynn, K. J. & Garcia, M. O. (2015b). Cracking the olivine zoning code: Distinguishing between crystal growth and diffusion. *Geology* **43**, 935–938.

- Sinton, J. M. & Detrick, R. S. (1992). Mid-ocean ridge magma chambers. *Journal of Geophysical Research: Solid Earth* **97**, 197–216.
- Sobolev, A. V. *et al.* (2007). The Amount of Recycled Crust in Sources of Mantle-Derived Melts. *Science* **316**, 412–417.
- Sobolev, A. V., Hofmann, A. W., Jochum, K. P., Kuzmin, D. V. & Stoll, B. (2011). A young source for the Hawaiian plume. *Nature; London* **476**, 434–7.
- Špillar, V. & Dolejš, D. (2013). Calculation of time-dependent nucleation and growth rates from quantitative textural data: Inversion of crystal size distribution. *Journal of Petrology* **54**, 913–931.
- Špillar, V. & Dolejš, D. (2014). Kinetic model of nucleation and growth in silicate melts: Implications for igneous textures and their quantitative description. *Geochimica et Cosmochimica Acta* **131**, 164–183.
- Stickel, J. J. & Powell, R. L. (2005). Fluid Mechanics and Rheology of Dense Suspensions. *Annual Review of Fluid Mechanics* **37**, 129–149.
- Streck, M. J. (2008). Mineral textures and zoning as evidence for open system processes. *Reviews in Mineralogy and Geochemistry* **69**, 595–622.
- Sun, Q., Jin, F., Liu, J. & Zhang, G. (2010). Understanding force chains in dense granular materials. *International Journal of Modern Physics B* **24**, 5743–5759.
- Tackley, P. J. & King, S. D. (2003). Testing the tracer ratio method for modeling active compositional fields in mantle convection simulations. *Geochemistry, Geophysics, Geosystems* **4**, 8302.
- Thomson, A. & Maclennan, J. (2013). The distribution of olivine compositions in Icelandic basalts and picrites. *Journal of Petrology* **54**, 745–768.
- Tilling, R. I., Rhodes, J. M., Sparks, J. W., Lockwood, J. P. & Lipman, P. W. (1987). Disruption of the Mauna Loa Magma System by the 1868 Hawaiian Earthquake: Geochemical Evidence. *Science* **235**, 196–199.
- Trulsson, M., Andreotti, B. & Claudin, P. (2012). Transition from the viscous to inertial regime in dense suspensions. *Physical Review Letters* **109**, 118305.
- Tsuji, Y., Kawaguchi, T. & Tanaka, T. (1993). Discrete particle simulation of two-dimensional fluidized bed. *Powder Technology* **77**, 79–87.
- Tuohy, R. M., Wallace, P. J., Loewen, M. W., Swanson, D. A. & Kent, A. J. R. (2016). Magma transport and olivine crystallization depths in Kīlauea’s east rift zone inferred from experimentally rehomogenized melt inclusions. *Geochimica et Cosmochimica Acta* **185**, 232–250.

- Turner, J. S. & Campbell, I. H. (1986). Convection and mixing in magma chambers. *Earth-Science Reviews* **23**, 255–352.
- van Keken, P. & Zhong, S. (1999). Mixing in a 3D spherical model of present-day mantle convection. *Earth and Planetary Science Letters* **171**, 533–547.
- Vermeesch, P. (2012). On the visualisation of detrital age distributions. *Chemical Geology* **312**, 190–194.
- Viccaro, M., Giuffrida, M., Nicotra, E. & Cristofolini, R. (2016). Timescales of magma storage and migration recorded by olivine crystals in basalts of the March–April 2010 eruption at Eyjafjallajökull volcano, Iceland. *American Mineralogist* **101**, 222–230.
- Wallace, G. S. & Bergantz, G. W. (2002). Wavelet-based correlation (WBC) of zoned crystal populations and magma mixing. *Earth and Planetary Science Letters* **202**, 133–145.
- Wallace, G. S. & Bergantz, G. W. (2004). Constraints on mingling of crystal populations from off-center zoning profiles: A statistical approach. *American Mineralogist* **89**, 64–73.
- Wallace, G. S. & Bergantz, G. W. (2005). Reconciling heterogeneity in crystal zoning data: An application of shared characteristic diagrams at Chaos Crags, Lassen Volcanic Center, California. *Contributions to Mineralogy and Petrology* **149**, 98–112.
- Wallace, P. J., Kamenetsky, V. S. & Cervantes, P. (2015). Melt inclusion CO<sub>2</sub> contents, pressures of olivine crystallization, and the problem of shrinkage bubbles. *American Mineralogist* **100**, 787–794.
- Walter, T. R. & Amelung, F. (2006). Volcano-earthquake interaction at Mauna Loa volcano, Hawaii. *Journal of Geophysical Research: Solid Earth* **111**, B05204.
- Welsch, B., Faure, F., Famin, V., Baronnet, A. & Bachelery, P. (2013). Dendritic Crystallization: A Single Process for all the Textures of Olivine in Basalts? *Journal of Petrology* **54**, 539–574.
- Wilkinson, J. F. G. & Hensel, H. D. (1988). The petrology of some picrites from Mauna Loa and Kilauea volcanoes, Hawaii. *Contributions to Mineralogy and Petrology* **98**, 326–345.
- Wyss, M. (1988). A proposed source model for the great Kau, Hawaii, earthquake of 1868. *Bulletin of the Seismological Society of America* **78**, 1450–1462.
- Yang, F.-L. & Hunt, M. L. (2006). Dynamics of particle-particle collisions in a viscous liquid. *Physics of Fluids* **18**, 121506.

# Jillian Schleicher

## *Curriculum Vitae*

### **Contact Information**

Department of Earth & Space Sciences  
University of Washington, Box 351310  
4000 15th Ave NE, Seattle, WA 98195  
Email: jmschl@uw.edu

### **Education**

Ph.D. Earth & Space Sciences 2011-2017  
Dissertation: *Crystal-scale control on magmatic mush mobilization and mixing*  
University of Washington, Seattle, WA

B.S. Geology & Physics, Minor in Mathematics 2007-2011  
University of Saint Thomas, St. Paul, MN  
*Magna Cum Laude*

### **Research Experience**

#### **National Science Foundation Graduate Research Fellow**

##### **University of Washington, Department of Earth & Space Sciences**

Crystal-scale control on magmatic mush mobilization and mixing: particle-based multiphase numerical simulations and geochemical mixing evidence from Hawaiian picrite samples.  
Advisor: Dr. George Bergantz. 2011-2017

#### **Research Assistant**

##### **University of St. Thomas, Geology Department**

Numerical simulation of Fossil Creek meteorogenic travertine deposition, Verde, Arizona.  
Advisor: Dr. Nikki Strong. 2011

Stratigraphic and stable isotope geochemical analysis of Miocene-aged strata located in southeast Nevada.  
Advisors: Drs. Thomas Hickson & Melissa Lamb. 2008-2009

#### **National Science Foundation Research Experience for Undergraduates Participant**

##### **Oregon State University, College of Oceanic and Atmospheric Sciences**

The tidal impact on sea surface advection along the coast of Oregon: Analysis of Regional Oceanography Modeling System (ROMS) simulation results.  
Advisor: Dr. Alexander Kurapov. 2010

#### **Research Assistant**

##### **University of St. Thomas, Physics Department**

Construction of a pendulum apparatus displaying chaotic behavior and development of theoretical simulations predicting behavior of the pendulum.  
Advisor: Dr. Martin Johnston. 2009-2010



## **Skills**

**Computer Languages/Programs:** Adobe Illustrator, ANSYS CFX, ArcGIS, C, Fortran, Inkscape, Jupyter Notebooks, LabVIEW, LaTeX, MATLAB, Mathematica, MFiX, ParaView, Python

**Laboratory Work:** Electrical circuitry, Electron Microprobe (JEOL 733 Superprobe & JEOL Hyperprobe JXA-8500F), computer data acquisition, optics laboratory setup

## **Teaching Experience**

### **University of Washington**

2015,16,17 Teaching Assistant: Living with Volcanoes (ESS 106)

2016 Teaching Assistant: Geomechanics (ESS 311)

2012 Teaching Assistant: Introductory geology lab section (ESS 101)

### **University of St. Thomas**

2010-11 Teaching Assistant: Fundamentals of the Lithosphere (GEOL 340, 360)

2010 Physics Tutor: Introductory Physics courses (PHYS 109, 110, 111, 112)

2009 Field Course Teaching Assistant: Regional Geology and Field Methods (GEOL 260)

2008-11 Mathematics Tutor: Calculus sequence courses (MATH 108, 109, 111, 113, 114, 200)

## **Awards, Fellowships, and Scholarships**

- 2017 David A. Johnston Award for Research Excellence
- 2016 Coombs, Ferrel, and Fuller Research Assistantship
- 2015 American Geophysical Union Outstanding Student Paper Award
- 2015 Dr. Howard A. Coombs Scholarship Fund
- 2015 Marie Ferrel Endowment Fund Research Assistantship
- 2014 Exxon Mobil Graduate Student Support Fund
- 2013 XSEDE Startup Allocation on TACC Lonestar Cluster
- 2012 National Science Foundation Graduate Research Fellowship
- 2012 Geological Society of America Graduate Research Grant
- 2012 Ferrel Fund - Geological Sciences, University of Washington
- 2011 University of Washington "Top Scholar" Award
- 2010 Barry M. Goldwater Scholarship
- 2010 Jack M. Brownstein Geology Scholarship, University of St. Thomas

## **Extra Curriculars, Outreach, & Workshops**

University of Washington, Department of Earth & Space Sciences

- 2014-16 Graduate student representative to the faculty
- 2012-16 "Rock"ing Out outreach program volunteer
- 2014,16,17 Departmental Gala oral presenter
- 2012,14 Family Day volunteer
- 2012-13 Graduate Student Brown Bag organizer
- 2012 Departmental Research Gala organizer

External Programs

- 2013-15 Burke Museum Girl Scout and Boy Scout Geology Days Volunteer
- 2014 NETL Workshop on Multiphase Flow Science
- 2013 Cooperative Institute for Dynamic Earth Research Participant
- 2013 ECSITE'13, EarthCube Summer Institute participant
- 2009-11 University of St. Thomas Geology Club co-president

## Professional Affiliations

Association of Environmental and Engineering Geologists, American Geophysical Union, Geological Society of America, Mineralogical Society of America

## Publications

**Schleicher, J.**, Bergantz, G. (*In press*). The mechanics and temporal evolution of an open-system magmatic intrusion into a crystal-rich magma. *Journal of Petrology*.

Bergantz, G., **Schleicher, J.**, Burgisser, A. (*In press*). On the kinematics and dynamics of crystal-rich systems. *Journal of Geophysical Research - Solid Earth*.

**Schleicher, J.**, Bergantz, G., Breidenthal, R., Burgisser, A. (2016). Time scales of crystal mixing in magma mushes. *Geophysical Research Letters* **43** (4), 1543-1550.

Bergantz, G., **Schleicher, J.**, Burgisser, A. (2015). Open-system dynamics and mixing in magma mushes. *Nature Geoscience* **8** (10), 793-796.

Lamb, M., Beard, L. S., Hickson, T., Umhoefer, P., Dunbar, N., **Schleicher, J.**, McIntosh, W. (2015). Late Oligocene-early Miocene landscape evolution of the Lake Mead region during the transition from Sevier contraction to Basin and Range extension. *Geological Society of America Bulletin*, B31144-1.

## Invited Talks

University of St. Thomas Geology Department and Center for Applied Math joint seminar, The 1868 Mauna Loa picrite eruption: A window into the multiphase dynamics of a magmatic mush. 21 November, 2014.

## Abstracts

Bergantz, G., **Schleicher, J.**, Linking Crystal Populations to Dynamic States: Crystal Dissolution and Growth During an Open-System Event. Oral session at: AGU Fall Meeting; 12-16 December 2016; San Francisco, California.

**Schleicher, J.**, Bergantz, G., Multiphase simulations constraining the characteristic volumes and efficiency of mixing within magmatic mushes. Oral session at: AGU Fall Meeting; 14-18 December 2015; San Francisco, California.

**Schleicher, J.**, Bergantz, G., Multiphase simulations constraining the characteristic volumes and efficiency of mixing within magmatic mushes. Poster presented at: AGU Fall Meeting; 15-19 December 2014; San Francisco, California.

**Schleicher, J.**, Bergantz, G., The dynamics of unlocking (fluidization) and mixing in particle-rich, viscous mixtures: MFX-DEM applications to Hawaiian volcanoes. Oral session at: NETL Workshop on Multiphase Flow Science; 5-6 August 2014; Morgantown, West Virginia.

**Schleicher, J.**, Bergantz, G., Geist, D., Petrologic observations and multiphase dynamics in highly-crystalline magmatic mushes sourcing Galápagos Island volcanoes. Poster presented at: AGU Fall Meeting; 9-13 December 2013; San Francisco, California.

**Schleicher, J.**, Strong, N., Sklar, L., Meteogenic travertine deposition through varied flow velocities: A model of the Fossil Creek travertine system in Verde, Arizona. Oral session at: GSA Annual Meeting; 9-12 October 2011; Minneapolis, Minnesota.